IMAGING AND SPECTROSCOPY OF CONDUCTING POLYMER-FULLERENE COMPOSITE MATERIALS

by

DAERI TENERY
B.A. State University of New York at Oswego, 2002

A dissertation submitted in partial fulfillment of the requirements
for the degree of Doctor of Philosophy
in the Department of Chemistry
in the College of Sciences
at the University of Central Florida
Orlando, Florida

Summer Term
2009

Major Professor: Andre J. Gesquiere

ABSTRACT

Since the development and optical study of conjugated (conducting) polymers it has become apparent that chain conformation and aggregation at the molecular scale result in complex heterogeneous nanostructured bulk materials for which a detailed insight into morphological, spectroscopic as well as optoelectronic properties and mechanisms is overwhelmingly difficult to obtain. Nanoparticles composed of the conjugated polymer poly[2-methoxy-5-(2-ethylhexyl-oxy)-p-phenylenevinylene] (MEH-PPV) and nanocomposite nanoparticles consisting of MEH-PPV doped with 1-(3-methoxycarbonylpropyl)-1-phenyl-[6.6]C_{61} (PCBM) were prepared as model systems to study these materials at the length scale of one to a few domains. The MEH-PPV and PCBM doped nanoparticles were analyzed by single imaging/particle spectroscopy (SPS) and revealed molecular scale information on the structure-property relationships of these composite materials. The data obtained from SPS were investigated in terms of spectral difference between doped and undoped nanoparticles. The doped nanoparticles are blue shifted by approximately 5-10 nm, have an additional blue shoulder, and show different vibronic structure than the undoped nanoparticles. Specifically, relative intensity of the 0-1 transition is lower than for the undoped nanoparticles. These data are indicative of differences in molecular order between both nanoparticle systems, detected at the molecular scale. In addition, the effect of electrical fields present in devices on the interfacial charge transfer properties was evaluated. Furthermore, these nanoparticles were incorporated into the lipid nanotubes to study the diffusion process of the single MEH-PPV nanoparticles inside the lipid nanotubes. Our data shows a clear proof of concept that diffusion of nanoparticles inside the hollow lipid nanotubes can be studied

on a single particle basis, which will allow us to study diffusion processes quantitatively and mechanistically within the framework of developing a biocompatible drug and gene delivery platform.

ACKNOWLEDGMENTS

There are so many wonderful people who I have encountered through my journey of Ph. D. study in chemistry. I would like to let all of them know that I could not have come this far without their help and support. First, I would like to sincerely thank my advisor Dr. Andre J. Gesquiere for his excellent guidance and endless patience and for providing me with a unique opportunity of research in the field of nanoscience. Dr. Gesquiere is one of the best physical chemistry professors I have ever met. I have learned so much from him in class and in the lab during my dissertation research. I hope to become an excellent teacher like him in the future.

I would like to offer special thanks to my dissertation committee members, Dr. Kevin Belfield, Dr. Diego Diaz, Dr. William Self and Dr. Lei Zhai, for their invaluable time, support, and guidance. I am grateful to Dr. Kevin Belfield for his encouragement and advice at the beginning of my graduate study when I was not sure if I was making the right decision to pursue a doctoral degree in chemistry. I clearly remember what he told me, and I now know that this is the best decision I have ever made. I would like to thank Dr. Diaz for his tremendous help with my candidacy. He has been very supportive of me at all times and I really appreciate him sharing his world experiences with me. I would like to thank Dr. Zhai for his good-natured support and for always making time for me when I needed help. To Dr. Diaz and Dr. Zhai, I give sincere thanks for the numerous recommendation letters they wrote on my behalf. I would like to express my appreciation to Dr. Self for his nurturing support and for being involved in my Ph. D. journey. I would like to thank Dr. Jiyu Fang for providing me with the $DC_{8,9}PC$ lipid nanotube samples.

Thank you to my coworkers Max Bonner and Zhongjian Hu for their emotional support and help. I am very fortunate to have special friends who were there to help me through some difficult times. I would like to deepest thanks to my special friends Rebecca Fidler, Debbie Maxwell, and April and Jose Marrone. They have always been supportive and have shared many happy and sad times with me. I very much enjoyed studying with Rebecca, Debbie, and April for classes we had to take for our graduate study.

I also would like to offer very special thanks to my best friend Wanda Ullom and her husband John Ullom. I have known them since I moved to Florida in 2002. I very much appreciate the support, care, and love they have given me. They have taught me how to be strong and have shown me that there is always hope no matter how bad a situation seems to be. I am so grateful to have them as my friends.

Mostly importantly, I would like to thank my mom, my aunt and uncle, Mi Ja and Tom Bucher, and my cousin, Joshua Bucher. Aunt Mi Ja and Uncle Tom raised me as their own child when I came to the United States in 1994. I thank them so much for providing me with a home and an education. They have always been supportive and encouraging through all of my endeavors. I truly believe that I could not be where I am at this point of my life without their generosity.

Thank you.

TABLE OF CONTENTS

LIST OF FIGURES

LIST OF TABLES

SUMMARY

Conducting polymers have been at the forefront of materials research on novel semiconductors given the exciting prospect of plastic electronic devices that may be built from solution processed materials with low-cost manufacturing processes, and the fact that these materials can be processed into nanosized high brightness probes for imaging applications. **Chapter 1** further introduces these topics and presents the background and significance of the reported dissertation research. The flow chart below gives an overview of the research projects reported in this dissertation.

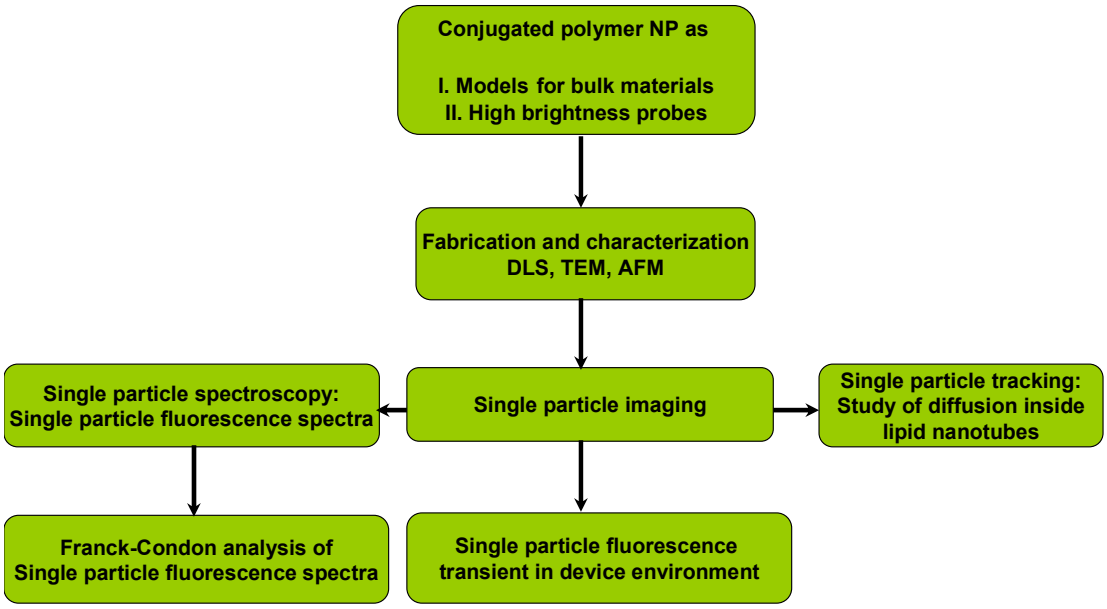

In Chapter 2 through Chapter 6 the dissertation research focuses on the study of the photophysics and optoelectronic properties of conducting polymers. The literature on the conducting polymer MEH-PPV comprising research in solution, bulk film, single molecule, and nanoparticles is briefly covered in **Chapter 2**. The literature data show that the properties of conducting polymers are highly dependent on polymer chain morphology and polymer chain interactions. On the nanoscale, variations in conjugated

polymer chain conformation, packing or aggregation can result in complex and heterogeneous materials. Due to this high complexity and heterogeneity it is impossible to achieve a detailed understanding of the photophysical and optoelectronic processes occurring in bulk conducting polymer films. To alleviate this issue, we develop novel composite conducting polymer poly[2-methoxy-5-(2-ethylhexyl-oxy)-p-phenylenevinylene] (MEH-PPV)/fullerene 1-(3-Methoxycarbonyl propyl)-1-phenyl-[6.6]C_{61} (PCBM) nanoparticles which represents an intermediate system between bulk films and single molecules, but have the functionality of the bulk materials. In other words, these nanoparticles are a model system for study of the properties of bulk materials from a molecular level perspective. Such composite nanoparticles offer many opportunities to obtain molecular scale information on conducting polymer properties by limiting the number of molecules under investigation, thus reducing the complexity of the system under investigation. The optical properties of *individual nanoparticles* were investigated by Single Particle Spectroscopy (SPS). SPS is an attractive tool to study the morphological and photophysical properties of the nanostructured materials at the molecular level. Utilizing SPS, detailed molecular information on the morphological and conformational effects on the photophysical properties of the blended nanoparticles is obtained. The custom built apparatus for SPS experiments is described in **Chapter 2** together with the experimental methods employed throughout the course of the presented dissertation research. A detailed discussion on the fabrication, characterization and SPS experiments completed on the composite nanoparticles is presented in **Chapter 3**. The collected data show that emission spectra of composite MEH-PPV/PCBM nanoparticles exhibit changes in vibronic structure with varying doping levels of PCBM. In **Chapter 4**,

this observation is rigorously investigated and explained by an in depth Franck-Condon analysis. One of the major findings from fitting the SPS data to a Franck-Condon model is that the emission spectra can be modeled as the superposition of two types of emitters, one with aggregate character and one with molecular character and that the aggregate character changes dramatically at very high doping levels of PCBM (50 and 75 wt %). In addition, these data give a molecular level insight on the distribution of exciton migration and exciton trapping properties of these materials as a function of composition. In **Chapter 5** the effect of applied electrical fields on the interfacial charge transfer processes occurring in composite MEH-PPV/PCBM nanoparticles was studied. The composite nanoparticles were incorporated into a field-only device in order to understand how the conducting polymer properties affect the overall performance of the device in the presence of electrical fields. Even though plastic electronic devices have electric field present on the order of $10^5 - 10^7$ V/cm during operation, this is a key issue that is often overlooked. The transients (fluorescence intensity as function of time) of the individual composite nanoparticles were collected at various applied voltages. The results show that the interfacial electron charge transfer rates do not change upon applied electrical fields similar to those found in fully functional devices.

In **Chapter 6** the MEH-PPV nanoparticles were introduced into the lipid nanotubes to study the diffusion kinetics of single MEH-PPV nanoparticles inside the lipid nanotubes. Since the MEH-PPV nanoparticles are very bright, they are excellent probes for use in single particle tracking (SPT) experiments. The motivation this work is that the lipid nanotubes have shown to be outstanding candidates for controlled nanoparticle drug delivery by releasing the preloaded biological molecules in a sustained manner. However,

the mechanisms of initial fast release followed by slow and sustained release of the biological molecules are not fully understood for this system. Our data give a clear proof of concept that diffusion of nanoparticles inside the hollow lipid nanotubes can be studied on a single particle basis, which will allow us to study diffusion processes quantitatively and mechanistically within the framework of developing a biocompatible nanoparticles drug and gene delivery platform.

CHAPTER 1. SCOPE OF THE DISSERTATION AND INTRODUCTION TO THE FIELD OF RESEARCH

1.1 Significance of dissertation research

1.1.1 Composite conjugated polymer nanoparticles as model systems for bulk composite conjugated polymer materials for application in organic photovoltaic devices: study of morphology-property relationships at the molecular level

As more strain is being placed on current energy supplies due to increasing demand, solar energy will become an indispensable addition to available energy sources. Polymer based solar cells, and organic photovoltaic devices (OPVs) in general are a particularly promising technology for solar energy conversion due to its advantages over inorganic PV cells including flexibility and ease fabrication at low cost.[1,2] Since the discovery that the efficiency of bulk heterojunction devices can exceed that of bilayer devices due to short exciton diffusion lengths in organic films (on the order of 10 nm), substantial research effort has been aimed at developing blended materials.[3-14] The blended film created from intermingling the acceptor and donor molecules forms a bicontinuous interpenetrating network providing a large interfacial area, thus exciton dissociation can reach close to unity.[15] Despite the efficiency of charge separation being close to unity, in this type of OPVs when using electron acceptors such as C_{60} and PCBM (1-(3-Methoxycarbonylpropyl)-1-1phenyl-[6.6]C_{61}), the device energy conversion efficiency is too low for practical applications. While an interpenetrating network of electron donor and acceptor materials provides a large interfacial area for efficient photoinduced charge separation, one of the most severely limiting factors in these OPV devices is the resulting complex nanostructured morphology of the active layer that is created by mixing of the electron donor and acceptor molecules. As a result, low carrier mobility and inefficient

carrier transport is typically observed. The architecture of bulk heterojunction OPV cell is shown in Figure 1.1.

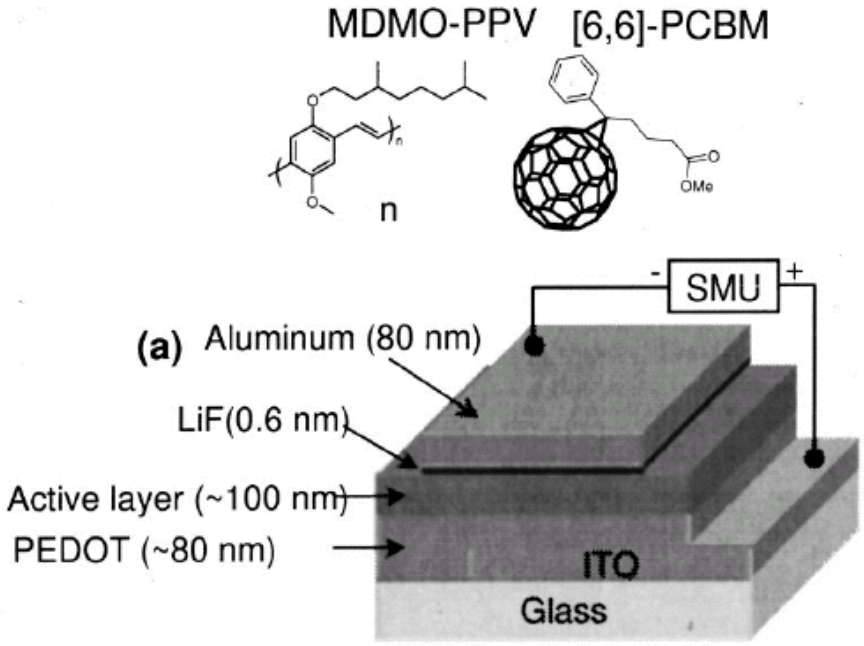

Figure 1.1 Schematic of bulk heterojunction organic photovoltaic cell in which the active layer is made up of MDMO-PPV and [6,6]-PCBM. The active layer of the blended film is created by intermingling of the acceptor and donor molecules, which form a bicontinuous interpenetrating network providing a large interfacial area for exciton dissociation by charge transfer from donor to acceptor. However, this active layer comes with very heterogeneous and complex nanostructured morphology. (Reproduced from reference [12]).

There is also tremendous controversy in the field about which active layer blend composition (i.e. 1:1 or 1:2 polymer:fullerene ratio) and thickness will result in the most efficient OPVs. For example it has been found by Yang's group that the best charge mobility is obtained for OPVs with approximately 200 nm thick active layers while van Duren et al. found the best charge mobility exists for devices with 100 nm thick active layers.[16,17] *At the basis of such controversies is in the complexity of the electronic and*

morphological structure of the organic materials at the molecular and mesoscale in these devices. The state of the field is further illustrated by the fact that well-known issues with current OPVs, which include light absorption, charge transport and charge collection at electrodes have remained largely unresolved for over a decade, mainly due to random trial-and error approaches to address these problems. In addition, genuine attempts to better understand these issues have had limited success. Past studies mostly involved current-voltage (I-V) device characterization and photocurrent measurements under solar spectrum air mass 1.5 (AM1.5) simulating conditions. These are bulk methods that give an averaged and sometimes misleading set of information, due to slow charge detrapping from deep traps for example.[18-26] The focus of the dissertation research is the fundamental study of structure (morphology)-optical property relationships of blended materials at the molecular and nanoscale instead of the macroscopic bulk level. *With the reported dissertation research, we aim to understand and relate material composition, morphology, optical properties, interfacial charge transfer processes and mechanisms at the molecular level.* The schematic of this idea is shown in Figure 1.2.

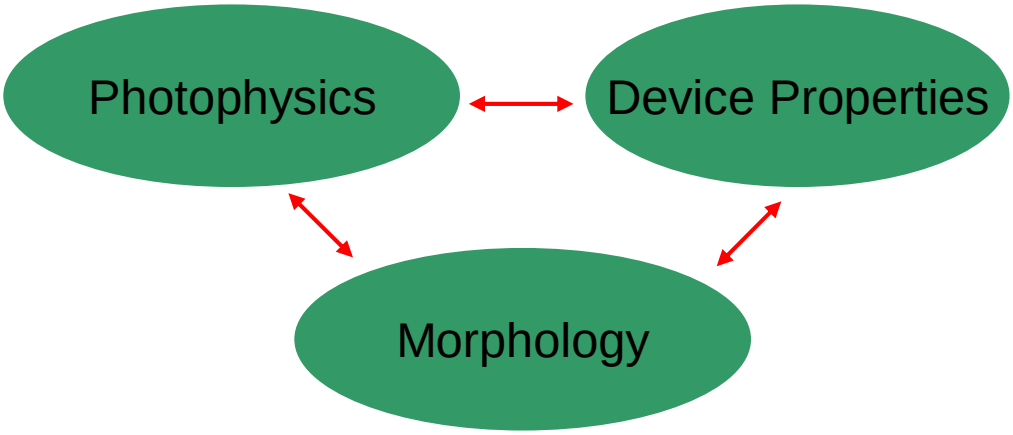

Figure 1.2 The schematic shows interconnected relationships between the morphology, photophysical properties of blended material to device properties. Thus, one must consider or understand how the morphology and photophysical properties of the blended material relate to device properties.

We have develop nanoparticles models for the bulk material with the goal of discovering the molecular level details of light harvesting, transfer of light energy and interfacial charge separation in organic functional materials. Since material properties (especially electronic structure) and mechanism and kinetics of interfacial charge transfer are affected by the device environment these materials are applied in, specifically the presence of electrical fields, these nanoparticles were also studied in a device environment.

1.1.2 Diffusion study of nanoparticles in lipid nanotubes via Single Particle Tracking of high brightness conjugated polymer nanoparticles

Self-assembled lipid nanotubules have shown promise as a controlled release system for drug delivery and gene expression applications. For example, the long term release of transforming growth factor-β from lipid tubules of 1,2-bis(tricosa-10,12-diynoyl)-sn-

glycero-3-phosphocholine ($DC_{8,9}PC$) to cell cultures has been used in soft tissue regeneration such as neurite extension or cell migration.[27,28] Price and coworkers found that the sustained release of tetracycline (antifouling agent) from $DC_{8,9}PC$ tubules, which were mixed into a ship's bottom paint formulation, inhibited the formation of marine fouling in ocean for six months.[29] Bellamkonda and coworkers demonstrated that $DC_{8,9}PC$ tubules were capable of sustained release of compacted plasmid DNA with a diameter of approximately 30 nm.[30] For example, only 30 % of the initially loaded DNA was released from the $DC_{8,9}PC$ tubules after 50 days in agarose hydrogels. The released DNA from $DC_{8,9}PC$ tubules was found to retain physical compaction and nuclease resistance. The sustained gene release is considered for a variety of in vivo applications such as wound healing, bone regeneration, and vaccination.[31-33] The advantages of lipid tubules-based delivery systems are summarized hereafter. First, lipid tubules-based delivery systems are biocompatible. Rudolph et al. found that $DC_{8,9}PC$ tubules have no significant effect on the in vitro proliferation of U937 histocytic monocytes, K52 erythroblasts, or Jurkat derivative lymphoblasts.[27] Second, they are injectable and can therefore be localized to specific sites of interest in vivo. For example, Yager and coworkers injected lipid tubules in living rats shows biphasic kinetics consisting of a burst followed by a slower phase for over 9 days.[34] Third, they involve no residual organic solvents, thus there is no need to mix immiscible phases. *However, the mechanism of slow and sustained release of bioactive agents from lipid tubules is not completely conceived*. From literature, *it has been suggested that the release rate of bioactive agents is associated with their diffusivity in lipid tubules, but very little is known on their diffusion behavior inside lipid tubules*. Recently, Orwar and coworkers

constructed lipid tubes-vesicle networks with microelectroinjection techniques. By using gel-capped electrodes, they observed the electrophoretic single-file transport of fluorescently labeled DNA molecules through the lipid tubes in the net works.[35] They also demonstrated that the tubes-vesicle network was able to support the electrophoretic transport of colloidal particles contained in the lipid tubes down to the limit of single particles.[36] However, the influence of the diameter and surface properties of lipid tubes on these electrophoretic transports has not been studied. In addition, the lipid tubes pulled from lipid vesicles using a micropipette technique have fluidic bilayer walls. Self-assembled lipid tubules formed by rolled-up bilayers are in a crystalline phase. The influence of the phase transition of bilayer walls on the diffusion of confined biomolecules is unknown. A detailed understanding of how the sizes, phases, and surface properties of lipid tubules affect the release rate of bioactive agents will provide the possibility of the designing lipid tubules for achieving their sustained release over a targeted period time. The focus of the dissertation research for this topic is on the diffusion study of approximately 30 nm nanoparticles of conjugated polymer MEH-PPV inside the $DC_{8,9}PC$ lipid nanotube via single particle tracking (SPT). The MEH-PPV nanoparticles are excellent probes to study SPS since they are very bright and the size is comparable to the compacted plasmid DNA. Our study can contribute to better understanding of diffusion processes that occurs inside the lipid tubules which can lead to improved or new design rules and principles for potential applications of tubule-based drug delivery systems.

1.2 Background of dissertation research

Conjugated polymers are organic semiconductors which possess an extended delocalization of the π-electron system. Conjugated polymers have gained much attention due to their attractive physical properties upon manipulation of the chemical structures. For example, their chemical structure can be modified to make the polymers soluble in organic solvents so that solution processing can be achieved at room temperature.[37] This is an ideal method to produce high quality thin films that can spread over large areas by spin coating. The ease of manipulation of the conjugated polymers has lead to research into its potential applications in optoelectronic devices such as organic photovoltaic cells, transistors, and light emitting devices.[14,38-40] Despite this versatility, critical issues remain given that the optical and electronic properties of conjugated polymer strongly depend on the physical conformation and aggregation of the polymer chains which influence the performance of the optoelectronic devices. To better understand how the morphology of films correlate with material properties and function, researchers have investigated the photophysical properties of conjugated polymers in solutions, bulk film, nanoparticles and even at single molecule level.

Examples illustrating that the recent discoveries proving that morphological heterogeneity exist in conjugated polymer (composite) materials at the scale of 30 nm and below are discussed first, followed by a very brief survey of recent literature showing the intense relationship between morphology and optoelectronic properties of the conjugated polymer MEH-PPV from bulk solution to single molecules.

1.2.1 Heterogeneous and complex nanostructured morphology of conjugated polymers

Shaheen et al. reported organic photovoltaic cells with power conversion efficiency of 2.5 % using a blend film of MDMO-PPV and PCBM as an active layer.[12] The authors prepared two types of blended films of MDMO-PPV and PCBM that were spin coated from either toluene or chlorobenzene solutions. As a result, two distinctive morphologies are obtained from these two blend films. This can be clearly seen from the AFM images of the films shown in Figure 1.3.

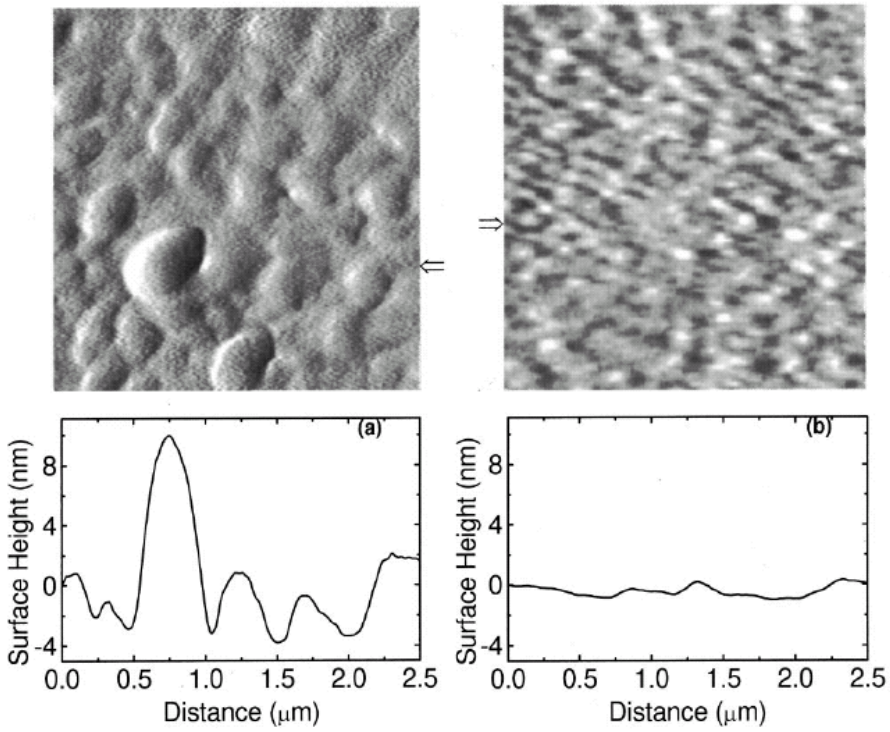

Figure 1.3 The surface morphology of MDMO-PPV:PCBM (1:4 by weight percent) blend films are shown in AFM images. The film thickness is approximately 100 nm and the cross section of the films is obtained which correspond to the marked arrows on the AFM images. (a) The film spin cast from a toluene solution. (b) The film spin cast from a chlorobenzene solution. (Reproduced from reference [12])

The AFM image of the film spin coated from a toluene solution shows large clusters throughout the film. The diameter and height of the clusters are approximately 0.5 μm and 10 nm respectively. The region that surrounds clusters is referred as valleys and is attributed to phase segregated regions with different concentration of PCBM. On the other hand, the AFM image of the film spin coated from chlorobenzene solution shows smaller clusters in which the diameter and height of the clusters are approximately 0.1 μm and 1 nm respectively. The smaller size of the clusters was assigned to better mixing of MDMO-PPV and PCBM in chlorobenzene compared to in toluene. The same blended films (MDMO-PPV and PCBM in toluene and chlorobenzene) were further investigated by Hoppe et al.[41] This study is different from Shaheen et al. in that the group prepared various weight ratios of two materials. To gain detailed information about the nanostructure under the surface of the film, the authors performed SEM on the profile of the samples, which is shown in Figure 1.4. At 1:1 ratio, small nanospheres (20 – 30 nm) that are embedded in the film can be observed. Because these nanospheres are smaller than the film thickness, they are not detected on the top view SEM images. For the higher PCBM content samples (1:2, 1:3, and 1:4), disk-like shaped nanoclusters are covered by another layer. The authors refer to this as a "skin" layer. The thickness of the skin is approximately 20 - 40 nm and the skin contains the nanospheres observed in the 1:1 ratio samples.

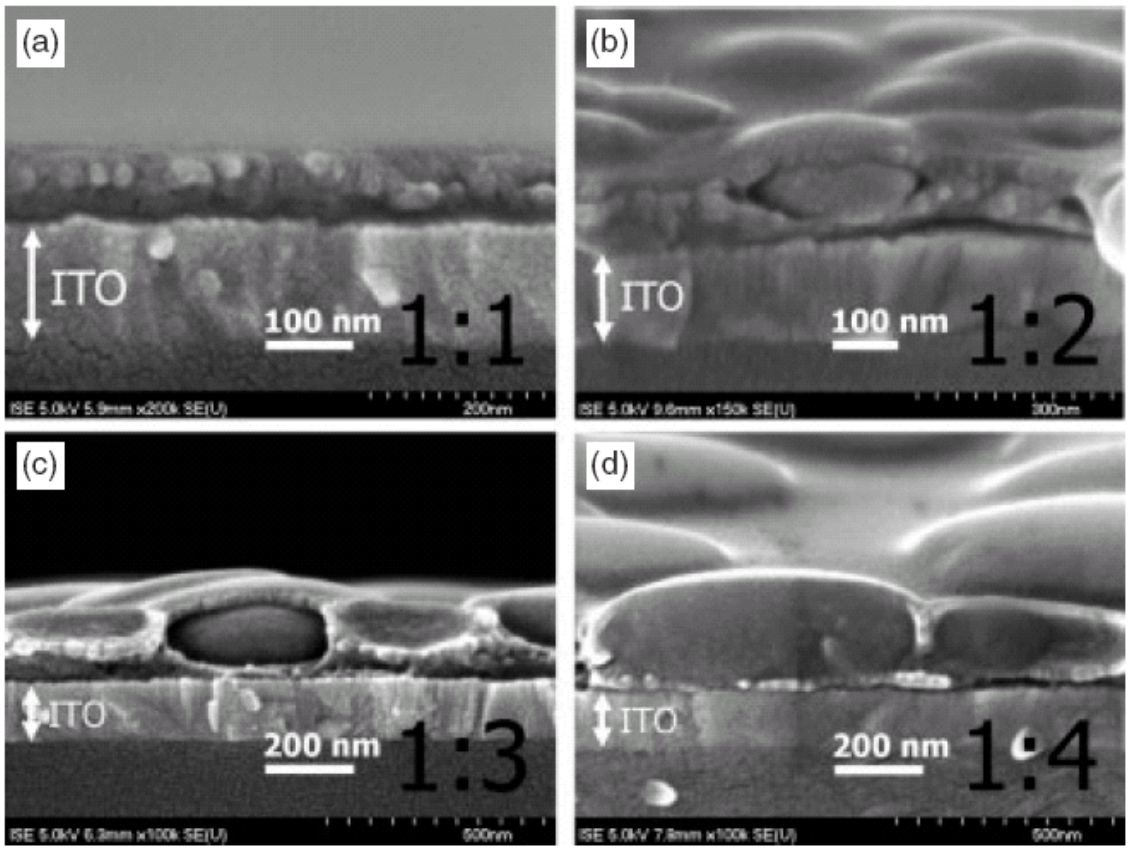

Figure 1.4 SEM images (cross-sections) of films spin coated from toluene solution with various weight ratios of MDMO-PPV:PCBM. (a) MDMO-PPV:PCBM (1:1 by weight percent) film contains small nanospheres that are approximately 20-30 nm. (b-d) MDMO-PPV:PCBM (1:2, 1:3 and 1:4 by weight percent) films show nanoclusters shaped like a disk which is covered with a layer of skin (another phase). Also, the nanospheres are found in the skin layer. The nanoclusters become larger as the PCBM content increases. (Reproduced from reference [41])

In Figure 1.5, the SEM images of profiles of films spin cast from toluene solution with 3 different weight ratios (1:2, 1:4, and 1:6) of MDMO-PPV to PCBM are shown.

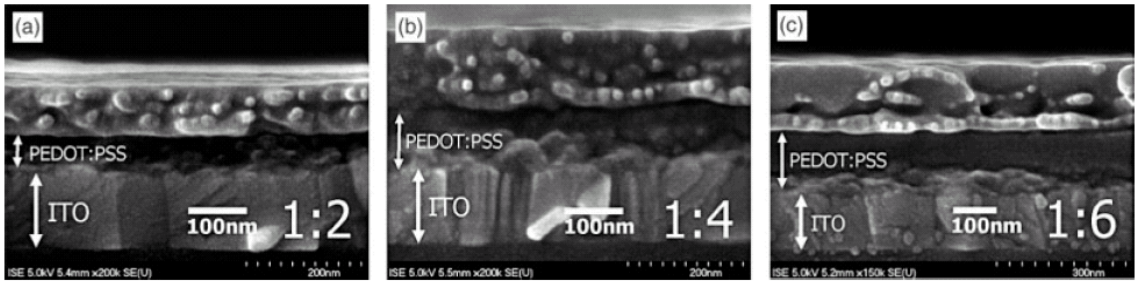

Figure 1.5 SEM images (cross-sections) of films spin coated from chlorobenzene solution with various weight ratios of MDMO-PPV:PCBM. (a-b) MDMO-PPV:PCBM (1:2 and 1:4 by weight percent) film contains small nanospheres that are approximately 20-30 nm throughout the film. (c) MDMO-PPV:PCBM (1:6 by weight percent) film starts show disk-like shaped clusters and the nanospheres are found in the skin layer. (Reproduced from reference [41])

In contrast to toluene cast films, small nanospheres (20nm) can be found for all the samples, even at higher content of PCBM. The nanospheres appear to be dispersed throughout the film (in a more homogeneous manner) and the skin layers are not predominant. At 1:6 ratio, larger nanoclusters are found but they are not as big as the nanoclusters found in the toluene cast films.

Dante et al. examined the surface and cross section of bulk heterojunction blends that were prepared from poly[2,6-(4,4-bis-(2-ethylhexyl)-4H-cyclopenta[2,1-b;3,4-b']-dithiopene)-alt-4,7-(2,1,3-bezothiadiazole) (PCPDTBT)], and [6,6]-phenyl C_{71}-butyric acid methyl ester (C_{71}-PCBM) with and without 1,8-octanedithiol.[42] The authors were interested in the addition of 1,8-octanedithiol because there have been reports in which the solar cell power conversion efficiency increased when small amount of 1,8-octanedithiol were added to the solution before spin-coating. The authors wanted to find out what effects the addition of 1,8-octanedithiol has on the morphology of the bulk heterojunction blends and relate the results to the observed power conversion efficiencies of OPVs comprising these materials as active layers. The authors collected topographic

and phase AFM images at high magnification (scan area of 250 nm by 250 nm). These are shown in Figure 1.6.

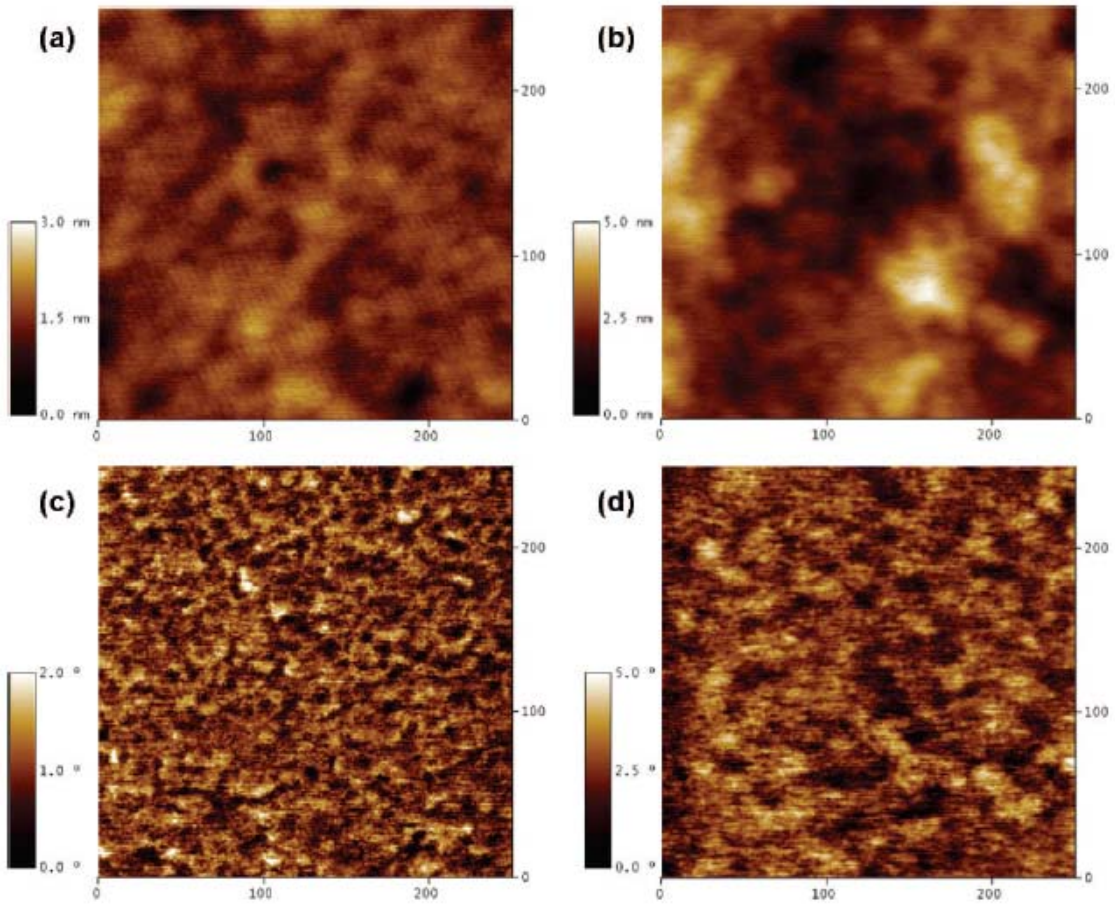

Figure 1.6 Topographic (top) and phase (bottom) AFM images of PCPDTBT:C_{71} –PCBM films without (a and c) and with (b and d) 1.8-octanedithiol are shown. The scan sizes are 250 nm by 250 nm. (Reproduced from reference [42])

As it can be seen, the topographic images show a rough surface morphology with evidence of phase separation. The phase images show that these two separated phases are in fact made up of smaller domains. The domain sizes increase from 7 nm to 13 nm upon addition of 1,8-octanedithiol. The phase images of cross sections of both samples are shown in Figure 1.7.

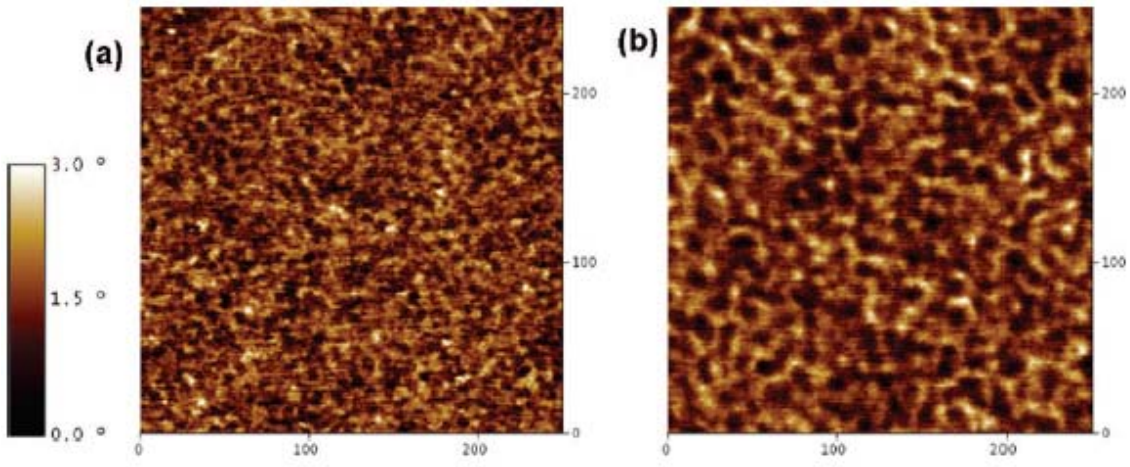

Figure 1.7 Phase AFM images of cross section of the sample that were prepared by cutting the PCPDTBT:C_{71} –PCBM film with (a) and without (b)1.8-octanedithiol are shown. The scan sizes are 250 nm by 250 nm. (Reproduced from reference [42])

The size of the domains in the film with 1,8-octanedithiol (8 nm) is larger than for the films without1,8-octanedithiol (5 nm).The larger phase separation between PCPDTBT and C_{71}-PCBM reduces the likelihood of interfacial charge recombination while the domain size is small enough to where exciton diffusion to the interface is efficient.

These recent results are quite compelling given that no strong evidence was given for the presence of such nanoscale structure in amorphous conjugated polymer films before these studies. Nguyen et al. attempted a study to show that local variations in morphology of a film (bumps and flat spots) influence the local electronic properties and thus the photophysics of the bulk film.[39] The authors performed an experiment in which the topographic images and spatially resolved photoluminescence (SRPL) are collected using NSOM. The topographic profiles and the normalized SRPL of MEH-PPV films cast from different solvents (CB and THF) are shown in Figure 1.8 a and b. The SRPL collected on the bump is clearly distinguishable from the off bump for both solvent systems confirming the conjugated polymer films are spatially inhomogeneous. The SRPL

spectrum collected from the flat area (spot 2) is similar to photoluminescence spectrum of MEH-PPV in CB solution. The SRPL spectrum collected for the bump (spot 1) shows red-shifted spectrum with enhancement of the vibronic peak (0-1) around 620 nm. According to the authors, this weak red PL tail is the emission from the aggregated chromophores and the PL enhancement around 620 nm is due to a change in vibronic coupling characteristics of MEH-PPV chromophores in regions with tightly packed chains. In the end however, the authors concluded that the flat region of the film is uniform in terms of morphology and optoelectronic properties.

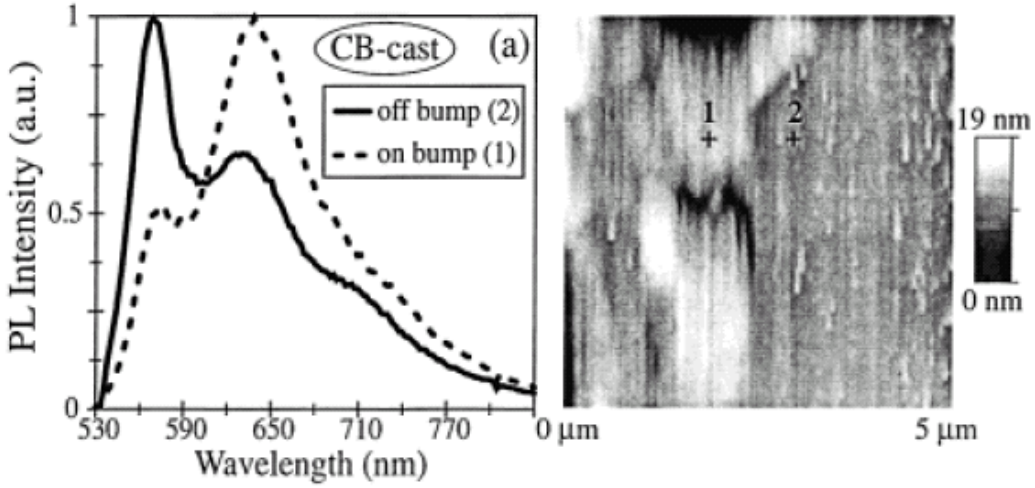

Figure 1.8 Topographic profiles (right) and normalized spatially resolved photoluminescence (SRPL) spectra (left) of MEH-PPV films spin coated from 1 % w/v chlorobenzene solution. Right: Topography profile obtained from film spin coated from chlorobenzene solution. The black to white color scale represents the height difference of 19 nm. The scan sizes are 5 μm by 5 μm. (Adapted from reference [39])

1.2.2 Spectroscopy of MEH-PPV in solution and solid state: effect of morphology and aggregation on optical properties

Due to space considerations only a brief survey of recent and highly cited literature on this topic is presented.

Solution Spectroscopy. Nguyen et al. studied poly[2-methoxy-5-(2'-ethylhexoxy)-p-phenylenevinylene] (MEH-PPV) solutions in THF, CB, and mixed solvent (equal volume mixture of THF and CB).[43] The absorption and photoluminescence spectra of these solutions are shown in Figure 1.9.

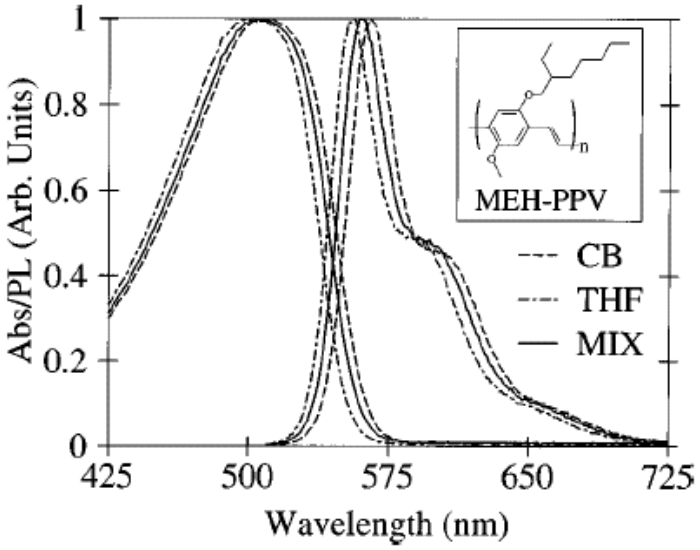

Figure 1.9 The normalized absorption and photoluminescence spectra of MEH-PPV in dilute solutions of chlorobenzene (CB, dashed lines), tetrahydrofuran (THF, dashed-dot lines) and a 1:1 mixture of chlorobenzene and tetrahydrofuran (MIX, solid line). The inset represents the molecular structure of MEH-PPV. (Reproduced from reference [43])

The absorption and photoluminescence spectra of MEH-PPV in CB are red-shifted relative to MEH-PPV in THF. As one can expect, the mixed solvent lies in between THF and CB. The authors explained the observation of the shifts is due to changing in the conjugation length of the polymer chains in the different solvents. For example, MEH-PPV forms extended conformation in CB to maximize the π-π interactions between the

polymer and solvent. However, MEH-PPV forms tightly coiled conformation in THF to avoid the interactions between aromatic backbones in the polymer with the solvent. Therefore, the extended conformation of MEH-PPV in CB indicates a longer conjugation length which results in the red shifted spectra compared to MEH-PPV in THF with shorter conjugated length. Photoluminescence excitation spectra were obtained for MEH-PPV dissolved in THF at different concentrations (w/v) (0.05, 0.10, 0.15, and 1.5 %) at emission wavelengths of 660 nm (Figure 1.10).

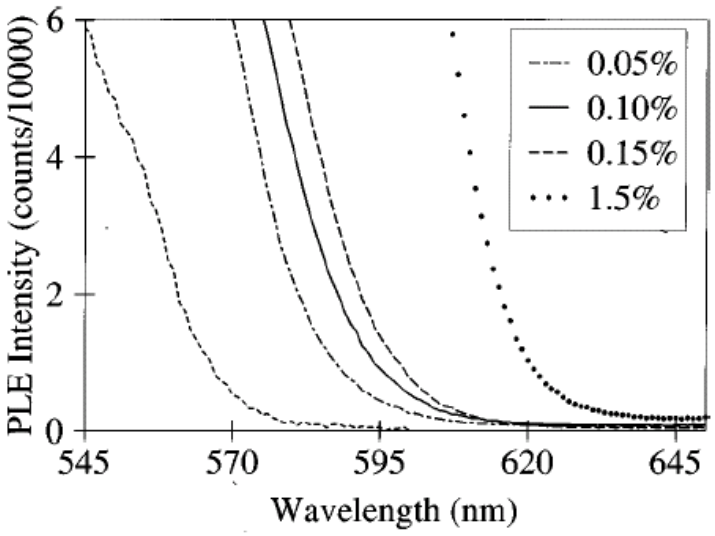

Figure 1.10 The zoomed in red portion of the 660 nm photoluminescence excitation spectra at different concentrations of MEH-PPV in THF. The concentrations (w/v) are 0.05 % (dash-dot line), 0.10 % (solid line), 0.15 % (dashed line) and 1.5 % (dotted line). (Reproduced from reference [43])

As the concentration of MEH-PPV in THF increases, the formation of aggregates becomes apparent. For example, the red-shifted and increasing relative intensity of the 660 nm photoluminescence excitation band can be observed in Figure 1.10. From this experiment, the authors concluded that the solvent and the concentration of the polymer play an important role in determining the conformation of the polymer chains and that

conformation of the polymer chains can be controlled by varying the solvents and the concentration of the polymer.

Zhang et al. investigated the photophysical properties and the fluorescence lifetime of MEH-PPV in mixtures of a poor solvent (cyclohexane or methanol) and a good solvent (chloroform).[44] The absorption spectra of MEH-PPV in chloroform and mixed solvent (chloroform-cyclohexane) are shown in Figure 1.11. The volume proportion of chloroform in the mixed solvent system are 100 %, 50 %, 20 %, 15 %, and 10 % which is labeled as 1 through 5 respectively.

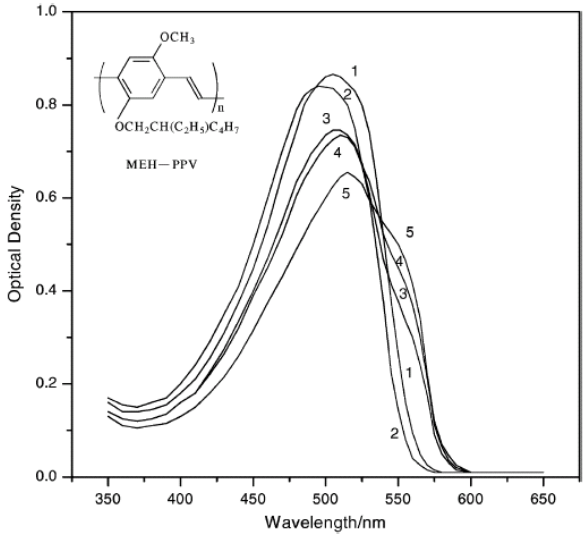

Figure 1.11 Absorption spectra of MEH-PPV in a mixture solvent system of chloroform-cyclohexane are shown. The proportion in volume of chloroform in the solvent system is followed as 100 % (1), 50 % (2), 20 % (3), 15 % (4) and 10 % (5). (Reproduced from reference [44])

As the volume proportion of cyclohexane increases, the absorption peak is first blue-shifted then gradually red-shifted in comparison to MEH-PPV in 100% chloroform. In addition, the volume proportion of 20 %, 15 %, 10% chloroform samples show a gradually increasing shoulder peaks around at 550 nm. The emission spectra of MEH-

PPV in chloroform and mixed solvent (chloroform-cyclohexane) are shown in Figure 1.12. The volume proportion of chloroform in the mixed solvent system are 100 %, 50 %, 30 %, 20 %, 15 %, and 10 % which is labeled as 1 through 6 respectively.

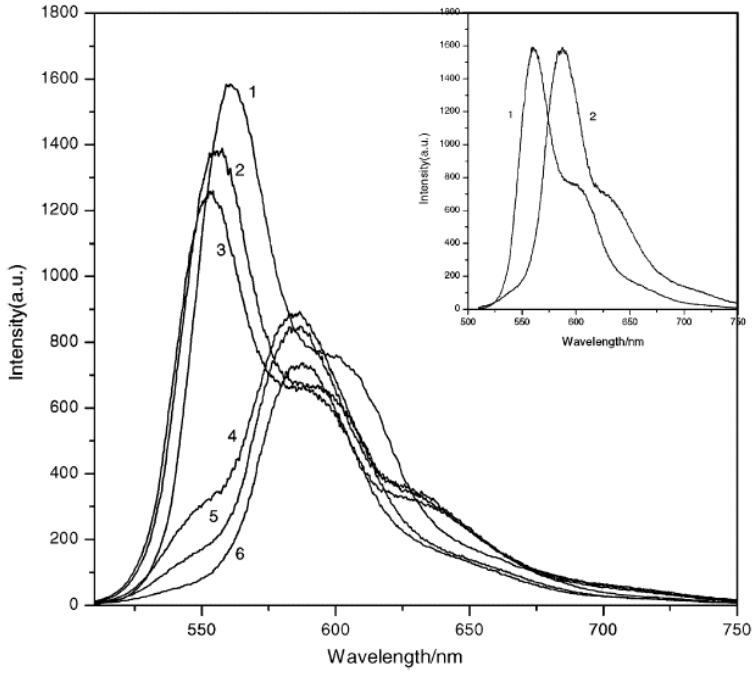

Figure 1.12 Emission spectra of MEH-PPV in a mixture solvent system of chloroform-cyclohexane are shown. The proportion in volume of chloroform in the solvent system is followed as 100 % (1), 50 % (2), 30 % (3), 20 % (4), 15 % (5) and 10 % (6) (Excitation wavelength at 500 nm). The inset displays the normalized emission spectra of MEH-PPV in 100 % chloroform (1) and 10 % chloroform (2). (Reproduced from reference [44])

The emission maximum is at 550 nm with two shoulders at 600 nm and 670 nm for MEH-PPV in chloroform. The volume proportions of 50 % and 30 % chloroform samples show blue-shifted emission peaks while maintaining similar vibronic structure as the chloroform with slight decrease in the emission intensity. However, for the volume proportion samples of 20 % and 15 % chloroform, there are dramatic changes in the vibronic structure while red-shifted emission peaks are observed. The emission intensity is also reduced by approximately half in comparison to 100 % chloroform. The inset in

Figure 1.12 show the normalized emission spectra of 100 % chloroform and 10 % chloroform. They both have similar vibronic structures but the 10 % chloroform is red-shifted by 30 nm. The authors considered two possibilities for the observations made from the absorption and emission spectra. The first possibility is the formation of aggregation in poor solvents (binary solvent systems in this case), which causes the changes in the spectral properties due to interactions between molecular chains. The second possibility is the self-coiling of the molecular chain.

The time-resolved fluorescence emission of MEH-PPV in chloroform and two mixed solvent systems were also collected by the authors. The data show that the lifetimes of MEH-PPV in binary solvents are longer than the lifetimes of MEH-PPV in 100 % chloroform.

Traiphol et al. investigated the photophysical properties of MEH-PPV in dilute solution. The study focused on the effect of solvent quality on conjugation length.[45] The solvent quality was categorized into difference in molecular structure, aromaticity and polarity. The absorption spectra of MEH-PPV in series of solvents are shown in Figure 1.13. The absorption peak at 495 nm of MEH-PPV in chloroform with broad and structureless absorption spectrum is obtained. They assigned the broad and structureless shape of absorption spectrum to of the presence of many individual chromophores with different band gaps. The absorption spectra of MEH-PPV in aromatic solvents (pyridine and toluene) show very little change in the shape but the absorption peak was red-shifted (λ_{max} = 500 nm) compared to MEH-PPV in chloroform. The most dramatic blue-shifted absorption peaks can be seen in solvents such as cyclohexane and hexane. The polarities of hexane and cyclohexane and toluene are very similar (dielectric constants of 1.9, 2.0,

and 2.4 respectively) however, the absorption spectra obtained of these solvents were very different.

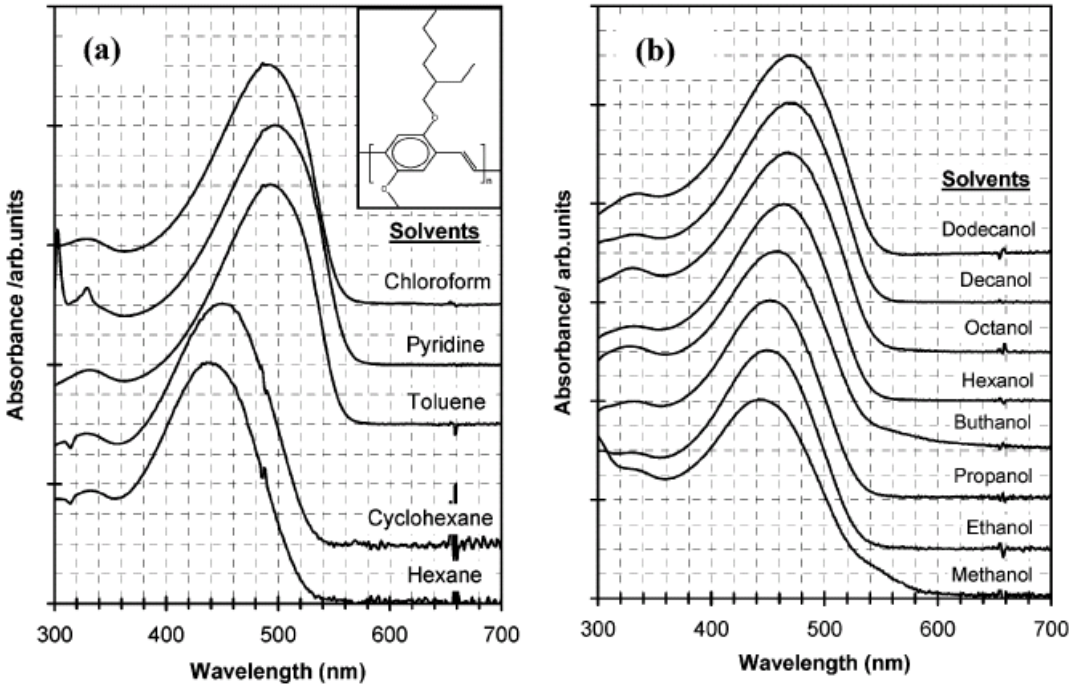

Figure 1.13 Absorption spectra of MEH-PPV in different solvents are shown. The solvent used is labeled on the right side of the corresponding spectrum. (Reproduced from reference [45])

Figure 1.14 shows the absorption peaks (λ_{max}) obtained from series of solvents as function of dielectric constant of the solvents. Dielectric constant of the solvent represents the degree of polarity. These data suggested that there is no correlation between the effective conjugation length and the solvent polarity.

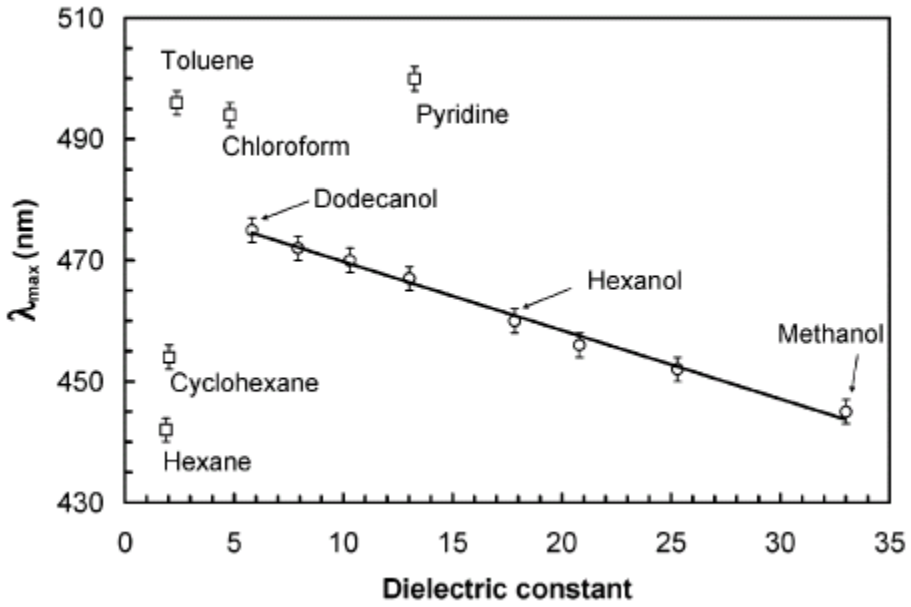

Figure 1.14 The absorption maximum peaks obtained from different solvents are plotted against dielectric constant of the solvent. For the data collected using the alcohol solvents are fitted to the linear equation $y = -1.13x + 481$, $R^2 = 0.99$. (Reproduced from reference [45])

The emission and excitation spectra of MEH-PPV in toluene and cyclohexane are shown in Figure 1.15 a and b respectively. These two solvents are chosen to represent the good (toluene) and bad (cyclohexane) solvents for MEH-PPV. The emission spectra of MEH-PPV in toluene at different excitation wavelengths (500, 470, and 530 nm) consist of an emission peak at 560 nm with a shoulder at 610 nm with similar vibronic structures but slight changing in the intensity. The excitation spectra also show a similar trend as the emission spectra which suggests that there is only one type of emitter present in the conjugated polymer chains which was assigned as the chromophores with the lowest energy gap, which are populated by energy transfer.

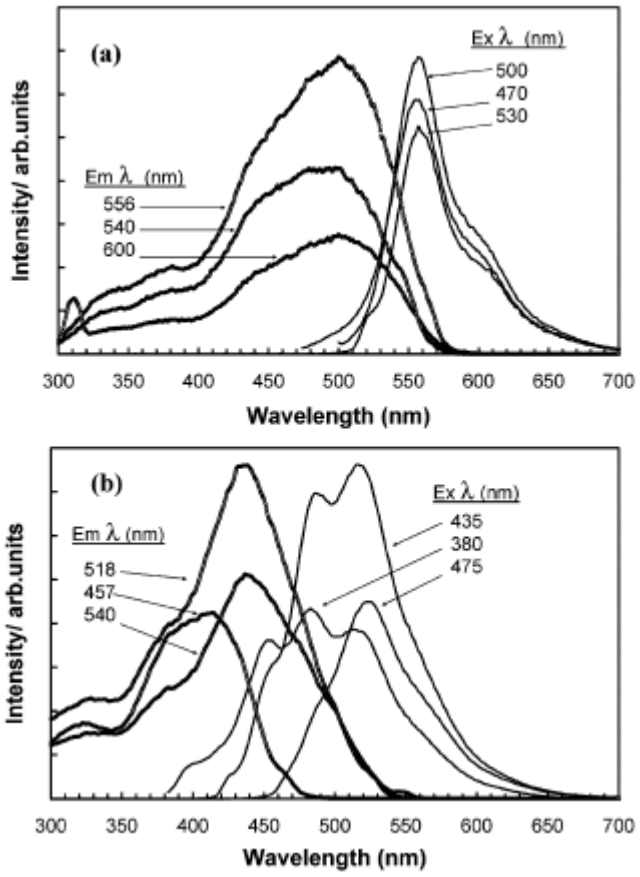

Figure 1.15 Excitation and emission spectra of MEH-PPV in (a) toluene (emission wavelengths at 540, 556 and 600 nm and excitation wavelengths at 470, 500 and 530 nm) and (b) cyclohexane (emission wavelengths at 457, 518 and 540 nm and excitation wavelengths at 380, 435 and 475 nm). (Reproduced from reference [45])

However, the emission spectra obtained from MEH-PPV in cyclohexane show distinct spectral shapes at different excitation wavelengths. The same observation can be seen in the excitation spectra. The dependency of the emission spectra at different excitation wavelengths indicate the presence of more than one type of emitters which appear due to the increase of disorder in the collapsed conformation in a poor solvent.

Bulk Film Spectroscopy. Shi et al. reported a systematic study of how the speed of spin casting affects the morphology of the polymer thin films.[46] The authors show that the morphology of the film only depends on the spinning speeds when the polymer concentration is in the certain range which was referred as concentrations for loose aggregation (CLA). Figure 1.16 displays the normalized EL emission spectra of the film casted from 0.7 wt % MEH-PPV in cyclohexanone at different spinning speeds of 1500, 2500, 4000, and 8000 rpm.

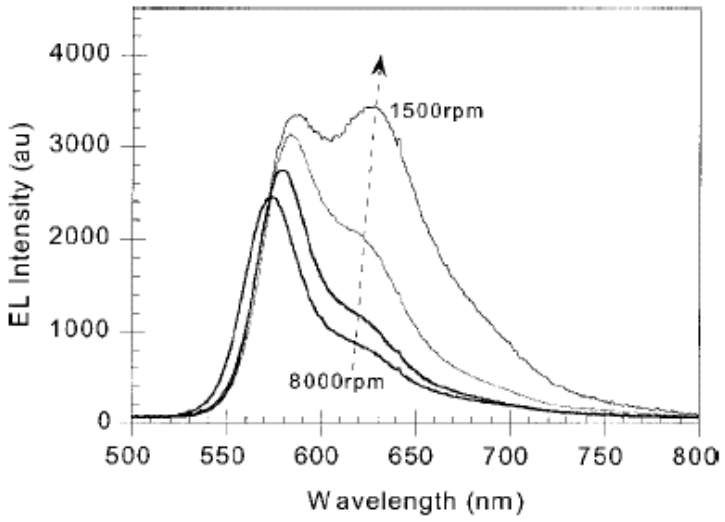

Figure 1.16 The normalized electroluminescence spectra of MEH-PPV films that are spin coated at different spinning speeds (1500, 2500, 4000, and 8000 rpm). (Reproduced from reference [46])

At high spin speeds (4000 and 8000 rpm), mainly a yellow EL emission peak (λ_{max} 575 nm) with a weak red shoulder (630 nm) is observed. When the spin speeds is decreased (2500 and 1500 rpm), the spectra are red-shifted and the red shoulder becomes stronger at 630 nm. The films prepared at higher spin speeds result in thinner films and the solvent evaporates faster than the films prepared at lower spin speeds. Thus, the films prepared at higher spin speeds have more extended conformation and the yellow emission is

originated from the singlet chain exciton in the more extended polymer chains. However, the films prepared at lower spin speeds favor the formation of interchain species (aggregation) because the solvent evaporates slower inside the film allowing the polymer chains to have more time to rearrange into their thermodynamically favorable conformation

Wang et al. performed a pump-dump experiment on MEH-PPV films spin cast from different solvent systems.[47] The group used a 100 fs pump pulse at 400 nm (~100μJ/cm^2) excites the polymer and is followed by a strong 100 fs dump pulse from a frequency doubled optical parametric amplifier (~1mJ/cm^2). Figure 1.17 a shows the steady state PL spectrum of MEH-PPV in toluene (black squares), PL dump spectra of at 550 nm (open circles) and 630 nm (open triangles). All three spectra look the same, thus the authors suggested that there is only one type of chromophore present in this case. Figure 1.17 b represents steady state PL spectrum of MEH-PPV in mixture solvent system (50/50 toluene and hexane) (black squares), PL dump spectra of at 550 nm (open circles) and 630 nm (open triangles). The PL pump spectrum at 550 nm in the mixed solvent shows the identical spectrum as in Figure 1.17 a except for the blue-shifted by 5 nm. The blue shifted spectrum is expected since the solvent system is less polar. In Figure 1.17 c, the authors obtained the spectrum of the chromophore in packed regions by subtracting the spectrum of steady state from the dump spectrum at 550 nm in mixed solvent system. The logic behind this procedure is the authors stated that the dump spectrum at 550 nm represents only the isolated chromophores while the dump spectrum at 630 nm represent both the isolated chromophore and packed chromophore regions (i.e. aggregates) respectively. Therefore, the outcome of subtracting the dump spectrum at 550 nm from

steady state spectrum gives the spectrum of the chromophores in packed regions. Figure 1.17 d shows the dump spectrum at 630 nm for the mixed solvent system (black circles) and the fitted spectrum (open circles) using a different linear combination of exactly the same isolated and packed chromophore spectra in the mixed solvent system. From the results, the authors concluded that the individual chromophores can be considered as a bimodal distribution rather than a continuous distribution of conjugation lengths or spectroscopic environments.

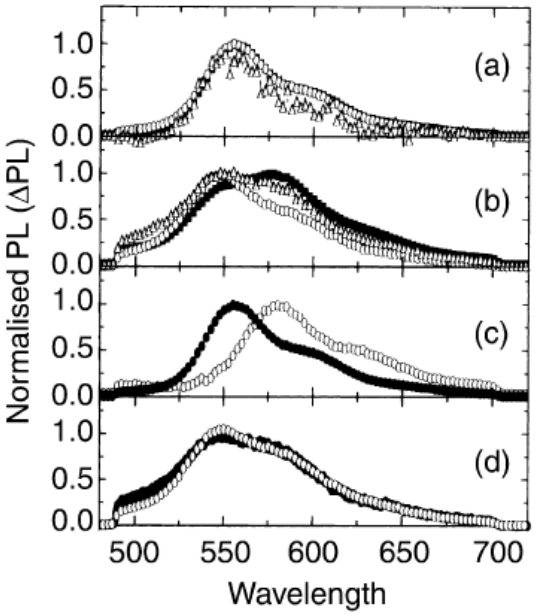

Figure 1.17 The photoluminescence and photoluminescence dump spectra of MEH-PPV are shown. (a) Steady state spectrum (dark squares), 550 nm dump spectrum (open circles) and 630 nm dump spectrum (triangles) in toluene. (b) Steady state spectrum (dark squares), 550 nm dump spectrum (open circles) and 630 nm dump spectrum (triangles) in mixture of toluene and hexane (50/50). (c) Comparison of steady state spectrum in toluene (dark circles) with the packed region spectrum obtained from the mixed solvent system. (d) Comparison of 630 nm dump spectrum (dark circles) in the mixed solvent system with a fitted spectra that was acquired by a linear combination of isolated and packed region spectra (open circles). (Reproduced from reference [47])

Nanoparticle Spectroscopy. Grey et al. studied the spectroscopic properties of MEH-PPV nanoparticles as function of nanoparticles size in which the size range from approximately 10 nm to 100 nm.[48] The authors investigated individual nanoparticles using the single particle spectroscopy at 20 K. The ensemble emission spectra of nanoparticles (aggregates) and low- and high- molecular weight of single polymer chains are constructed from many individual single molecule/particle spectra. The ensemble spectra and the histogram of emission maximum peaks for nanoparticles (aggregates), low- and high- molecular weights single polymer chains are shown in Figure 1.18.

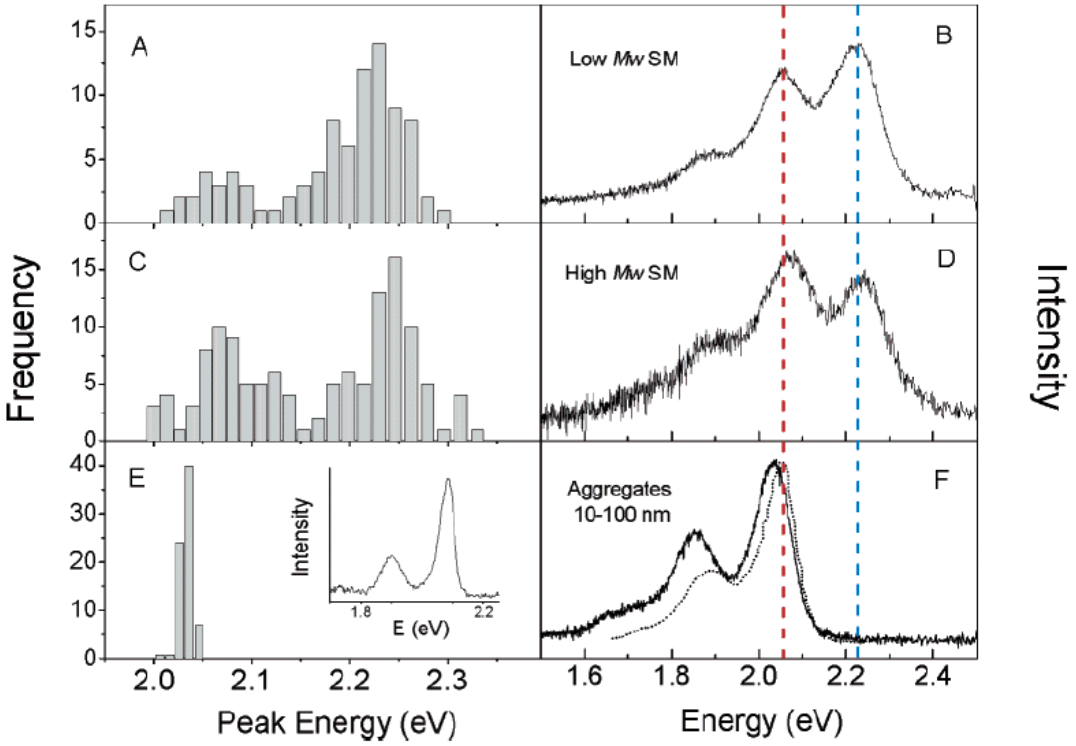

Figure 1.18 (A, C, and E) Peak wavelength histograms and (B, D, and F) ensemble spectra of MEH-PPV single molecules and nanoparticles (aggregates) measured at 20 K. The low- and high- molecular weight of single molecules is 186,000 amu and 1000,000 amu respectively. (Inset E) Emission spectrum of a single MEH-PPV nanoparticle measured at 20 K. (F) Emission spectrum of a MEH-PPV bulk film measured at 4 K (dashed line). (B, D, and F) The red and blue vertical dashed lines represent the red and blue peak energy maxima respectively. (Reproduced from reference [48])

As it can be seen in Figure 1.18 A and C, the energy distributions exhibit bimodal characteristics which indicates that the ensemble spectra is superimposed of emission from the high energy blue sites and low energy red sites. The vibronic origin (0-0 transition) of the blue and red emitters is represented by the red and blue vertical dashed lines. The ratio of blue to red emitters changes upon the molecular weight (Figure 1.18 B and D). As it can be expected, the intensity of the red emitter increases with increasing the molecular weight since the probability of the presence of red site increases with more chain-chain contacts in the higher molecular weight conjugated polymer chains. Interestingly, the ensemble spectra of the nanoparticles show no emission from the blue sites (Figure 1.18 F). The energy distribution of the nanoparticles is very narrow and closely matched with the emission maxima of the bulk MEH-PPV. In addition, the ensemble spectra of the nanoparticles look very similar to the spectrum of bulk thin film (Figure 1.18 F, dashed line). The authors concluded that MEH-PPV nanoparticles that are greater than 10 nm in size behave as bulk-like materials.

Szymanski et al. prepared a stable, aqueous dispersion of MEH-PPV conjugated polymer nanoparticles that are approximately 5 – 10 nm in size and studied the nanoparticles by Near Field Optical Microscopy (NSOM).[49] The absorption spectrum of the aqueous suspension of MEH-PPV nanoparticles is slightly blue-shifted compared to the MEH-PPV in THF. This observation is ascribed by the *decrease in conjugation length due to the kinking and bending of the polymer backbone*. The fluorescence spectra of the aqueous suspension of MEH-PPV nanoparticles, MEH-PPV in THF and that of thin film were obtained for comparison. The fluorescence spectra are largely red-shifted for both aqueous suspension of MEH-PPV nanoparticles and thin film compare to MEH-PPV in

THF. This is attributed to *energy transfer to the low-energy chromophores and weakly fluorescent aggregates which is enhanced by intra- and interchain interactions in the nanoparticles* and thin film. It was noted by the authors that the absorption spectrum of nanoparticles shows a blue-shifted spectrum while the fluorescence spectrum displays the red-shifted spectrum compared to MEH-PPV in THF. This suggested that there is a very small fraction of intrachain aggregates in the ground state and a large fraction of intrachain aggregates in the excited state. The authors referred to literature where exciton diffusion length of MEH-PPV is found to be approximately 20 nm which is larger than the size of the nanoparticles. Thus, an efficient energy transfer to intrachain aggregates causes the red-shifted fluorescence spectrum.

Single Molecule Spectroscopy. Vanden Bout et al. studied a single conjugated copolymer PPV-PPyV which is derivatized from poly(p-phenylene vinylene) and poly(p-pyridylene vinylene).[50] The molecular structure of PPV-PPyV and a fluorescence transient are shown in Figure 1.19 a and b respectively. The transient of PPV-PPyV exhibits discrete intensity jumps in which the fluorescence intensity drops down to the background level (50 counts per second) and comes back to fluorescence intensity level of 4000 counts per second before it permanently photobleaches at 40 seconds. The authors discuss that this observation would be expected in a single chromophoric system but not for conjugated polymers which consist of many chromophores. Thus, the authors suggested that there is an efficient intramolecular energy migration to a defect site along the polymer chain (i.e. a radical cation and radical anion) where the fluorescence is quenched temporarily, i.e. the chromophores are coupled. However, this process is reversible, the mechanism of

which was later proven experimentally by Gesquiere et al. by means of the F-V/SMS technique.[51] Figure 1.19 c displays the histogram of the normalized intensity levels for a collection of single molecule transients. Almost all the molecules show the three distinct peaks at dark levels (blue) and intermediate levels (red) and bright levels (green) which is consistent with discrete intensity jumps.

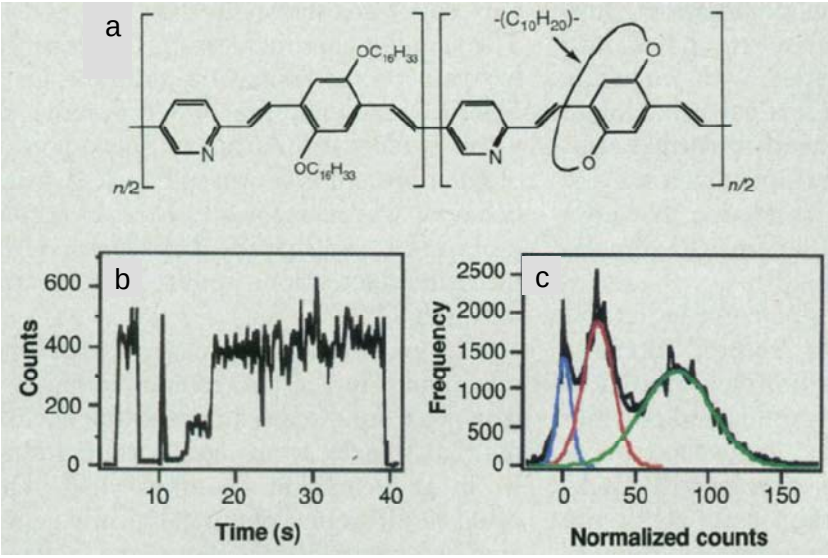

Figure 1.19 (a) The molecular structure of conjugated copolymer PPV-PPyV is shown. (b) The transient of fluorescence intensity as function of time is acquired. The bin size is 100 ms. The excitation wavelength used is 514 nm at laser power of 0.25 μW. (c) Combined intensity histogram of transients from 40 molecules is shown. Each transient was normalized by dividing the intensity collected by the initial intensity (first 500 ms of irradiation).Colored curves represent the Gaussian fits to the dark intensity (blue curve), intermediate intensity (red curve) and bright intensity (green curve). (Reproduced from reference [50])

Yu et al. investigated the individual MEH-PPV molecules dispersed in PMMA and polystyrene matrix at low temperature (20 K). [52] The authors took advantage of a narrow bandwidth fluorescence spectrum which was determined to be 10 nm at low temperature while a broader bandwidth fluorescence spectrum of 37 nm is obtained at room temperature (300 K). The narrow bandwidth fluorescence spectrum at low temperature

shows the distinction between different types of chromophores in the spectrum. In Figure 1.20, the spectrum of individual MEH-PPV molecules in PMMA at 300 K (a) and 20 K (b and c) is shown. Two types of single molecule spectrum were obtained at low temperature and they were assigned as either a single-chromophore type (Figure 1.20 b) or a multi-chromophore type (Figure 1.20 c).

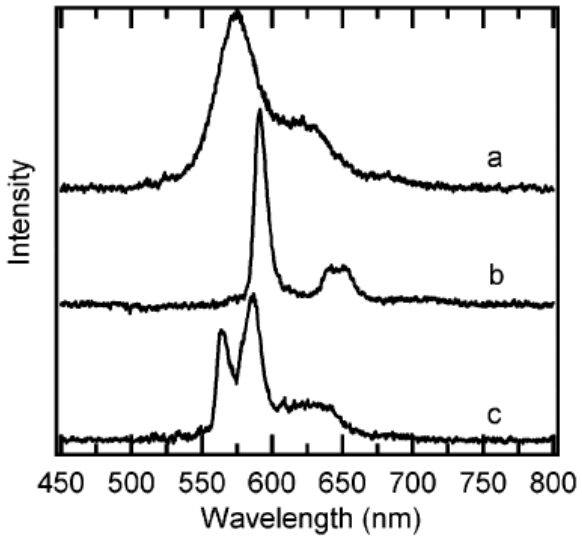

Figure 1.20 Fluorescence spectra of single MEH-PPV molecules are shown. (a) A representative single molecule spectrum of MEH-PPV at 300 K. (b) Single molecule spectrum of MEH-PPV at 20 K showing single-chromophore characteristics (emission of only red chromophore). (c) Single molecule spectrum of MEH-PPV at 20 K showing multichromophore characteristics (emission from both blue and red chromophores). (Reproduced from reference [52])

Figure 1.21 a and b show the fluorescence spectra from two different MEH-PPV molecules under two different excitation wavelengths (488 nm and 543 nm). Using two different excitation wavelengths, different chromophores in the polymer chains can be excited. The fluorescence spectra obtained from different excitation wavelengths does not change significantly for both of the molecules. This indicates that there is an efficient energy transfer to the same low energy site regardless the initial excitation wavelength.

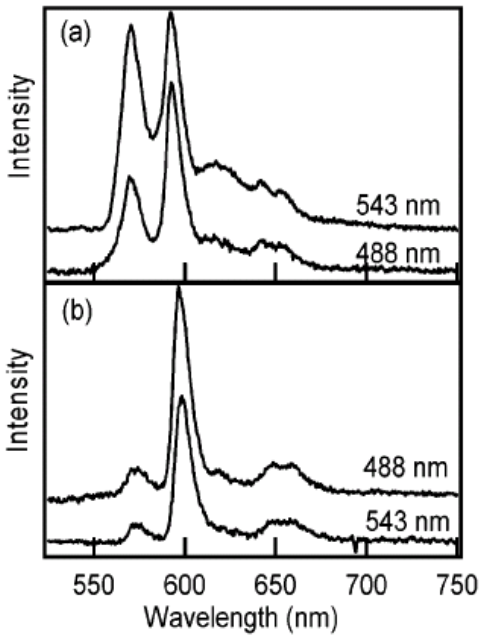

Figure 1.21 (a) Fluorescence spectra of two different MEH-PPV molecules at 20 K using excitation wavelengths of 488 nm and 543 nm. (Reproduced from reference [52])

1.2.3 Studies of diffusion inside nanotubes

In order to utilize the lipid nanotubes as vehicles for delivering biomolecules or drugs, it is critical to understand the diffusion process occurring of these molecules inside the lipid nanotubes (i.e. sustained release of compacted plasmid DNA from $DC_{8,9}PC$ tubules). There have been experiments performed to gain insight into the fundamental understanding of transport mechanism of nanostructured materials. Jayaraman et al. studied the wettability of the hydrophobic interiors of the silica nanotubes to find out whether the wetting phenomena in the nanotube (nanoregime) deviate from the wetting phenomena in macroscopic scale.[53] The various sizes of silica nanotubes were fabricated using surface sol-gel template synthesis. The interior of the silica nanotube was modified

as hydrophobic surface by covalently attaching octadecyltrimethoxysilane (OTS). The TEM and the confocal fluorescence images are shown in Figure 1.22.

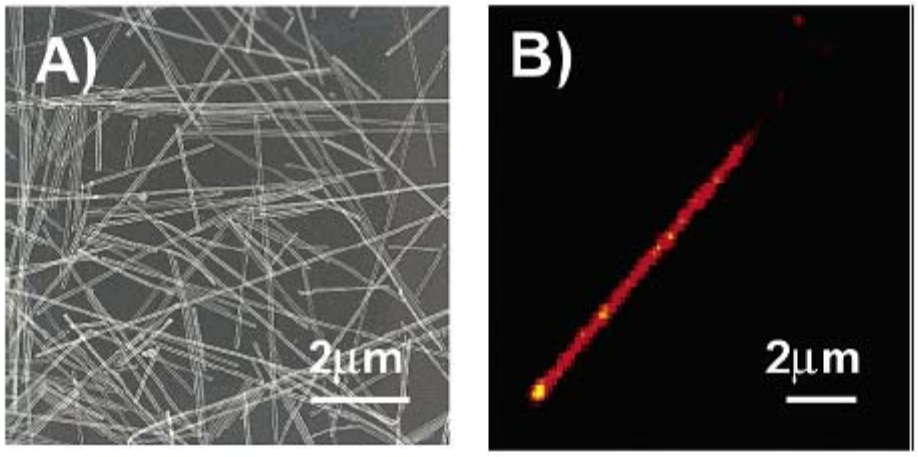

Figure 1.22 (A) TEM image of hydrophobic interior silica nanotubes. (B) Confocal fluorescence image of the silica nanotube in which the interior surface contains a small amount of the fluorescent dye, $DiIC_{18}$. (Reproduced from reference [53])

As it can be seen the length of the silica nanotube varies greatly while uniform diameter of the silica nanotubes is obtained (approximately 30 nm). A fluorescence recovery after photobleaching (FRAP) experiments were performed to monitor the diffusion of the dye molecules ($DiIC_{18}$) inside the hydrophobic silica nanotubes. In addition, these samples were prepared in two different solvents, water and methanol to investigate the wetting strength at the nanotube interior. Figure 1.23 displays confocal fluorescence images of before and after photobleaching of silica nanotubes in water (Figure 1.23 A and B) and methanol (Figure 1.23 C and D) respectively.

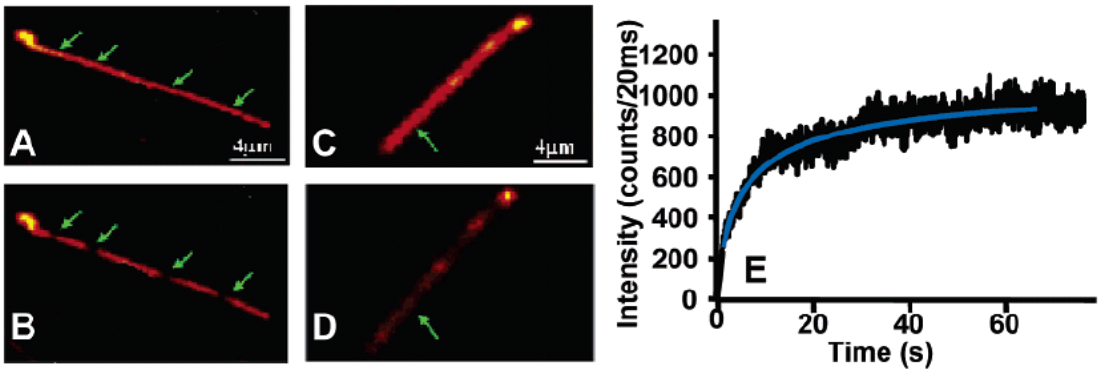

Figure 1.23 (A) Confocal fluorescence image of $DiIC_{18}$-bearing hydrophobic silica nanotube immersed in water prior to performing FRAP experiment. The green arrows represent the locations where the photobleaching will take place. (B) Confocal fluorescence image of $DiIC_{18}$-bearing hydrophobic silica nanotube immersed in water obtained 26 minutes after photobleaching. (C) Confocal fluorescence image of $DiIC_{18}$-bearing hydrophobic silica nanotube immersed in methanol prior to performing FRAP experiment. (D) Confocal fluorescence image of $DiIC_{18}$-bearing hydrophobic silica nanotube immersed in methanol after performing FRAP experiment. (E) Fluorescence recovery curve obtained from $DiIC_{18}$-bearing hydrophobic silica nanotube immersed in methanol. (Reproduced from reference [53])

There are four spots (indicated with green arrows) on the silica nanotube that were photobleached (Figure 1.23 A). The same nanotube was imaged 26 minutes after photobleaching of the four spots (Figure 1.23 B). As it can be seen, the four spots are permanently photobleached and no diffusion of the dye molecules was observed. This indicates the interior of the silica nanotube is dry and this observation is supported by single-molecule fluorescence correlation spectroscopy (FCS) studies in which the $DiIC_{18}$ is able to diffuse freely at the interface between water and a dimethyloctadecylsilane surface.[54] Interestingly, the diffusion dynamics of dye molecules inside silica nanotube in methanol show completely different behavior. For this sample, only one spot was photobleached (Figure 1.23 C) however, the whole silica nanotube is appeared to be dimmer (less in fluorescence intensity, Figure 1.23 D). According to the authors, this observation can be explained by rapid diffusion of the dye molecules during and after

photobleaching thus the fluorescence intensity of the entire silica nanotube decreases. The fluorescence recovery curve for the silica nanotube in methanol is shown in Figure 1.23 E. The diffusion coefficient calculated from this curve is determined to be 8.7 x 10^{-7} cm^2/s.

Guo et al. investigated the diffusion rates of dye molecules (Rhodamine 6G (R6G) and Nile red (NR)) inside lipid tubules formed by 1,2-bis(10,12-tricosadiynoyl)-sn-glycero-3-phosphocholine ($DC_{8,9}PC$) via FRAP and FCS.[55] The fluorescence images of the lipid tubules with R6G and NR are shown in Figure 1.24 a and b respectively.

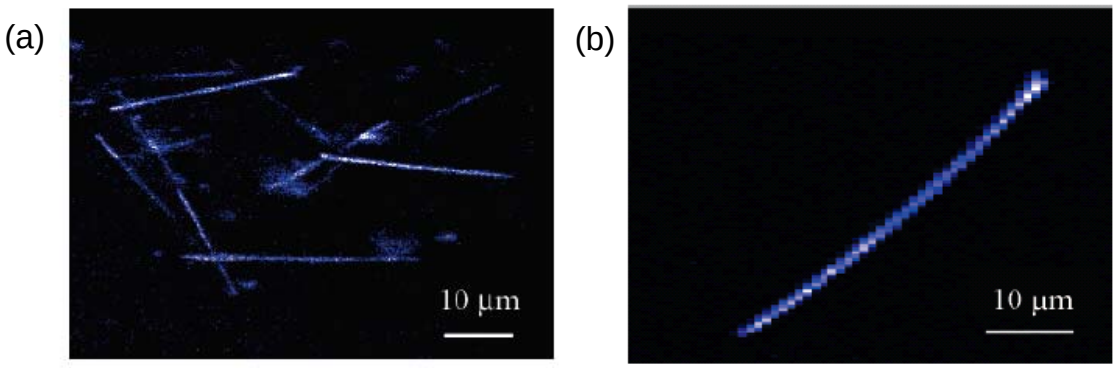

Figure 1.24 (a) Confocal fluorescence image of lipid tubules that are hydrated with 1μM of R6G. The excitation wavelength of 514.5 nm and power of 350 nW was used. (b) Confocal fluorescence image of lipid tubule that is hydrated with 1μM of NR. (Reproduced from reference [55])

The FRAP experiment was performed in the region of interest (RIO) on the lipid tubules which is categorized into three general regions. The first region is the aqueous phase in the tubule interior (region 1). The second region is the area immediately near the inner surface of the tubule (region-2). The third region is the tubule wall (region-3). Figure 1.25 displays the FRAP traces of R6G acquired at different positions along a lipid tubule (i.e. The positions (P_1 through P_4) investigated on the lipid tubules goes from left side of the lipid tubes to center to the right side of the lipid tube).

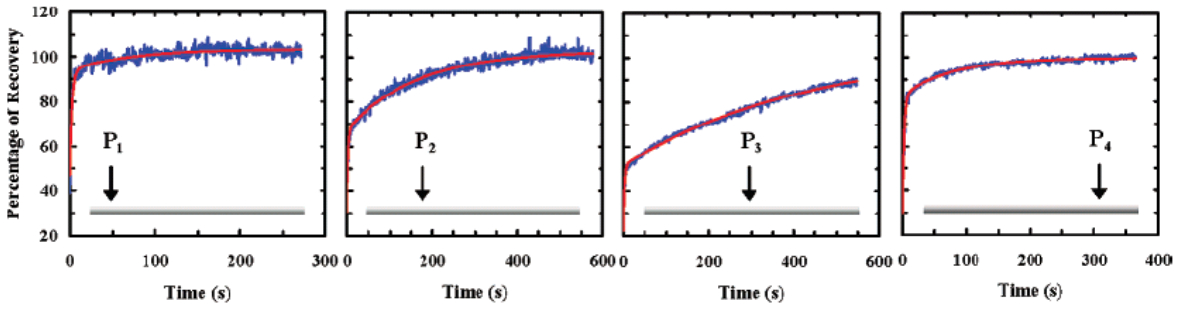

Figure 1.25 FRAP measurements of R6G positioned along the lipid nanotube and schematic of the position of the lipid nanotube under investigation is shown on the bottom of each panel. (Reproduced from reference [55])

The fluorescence recovered from FRAP experiment indicates the fluorescence signal recovers in biphasic manner which is composed of fast and slow phases. However, the fast phase could not be studied since it was not obtainable due to limitation of response time of the instrument. However, the slow phases (slow diffusion of the R6G dye molecule) were obtained and attributed to the interactions of the R6G dye molecules near or inside wall of the lipid tubules (region 2 and 3). As it can be seen in Figure 1.25, the diffusion kinetics of the R6G dye molecules inside the lipid tubules is strongly dependent on the position. For example, the diffusion of the dye molecule inside the lipid tubule becomes slower towards the center (P_3, recovery time of 440 seconds) then becomes faster at the end (P_4, recovery time of 70s). The possible explanation for this observation is assigned to the maximum lipid packing density at the center region of the lipid tubule. FRAP measurements of NR inside the lipid tubules were obtained. As it can be seen in Figure 1.26, the fluorescence signal only recovers approximately 25 – 45 % (from different lipid tubules).

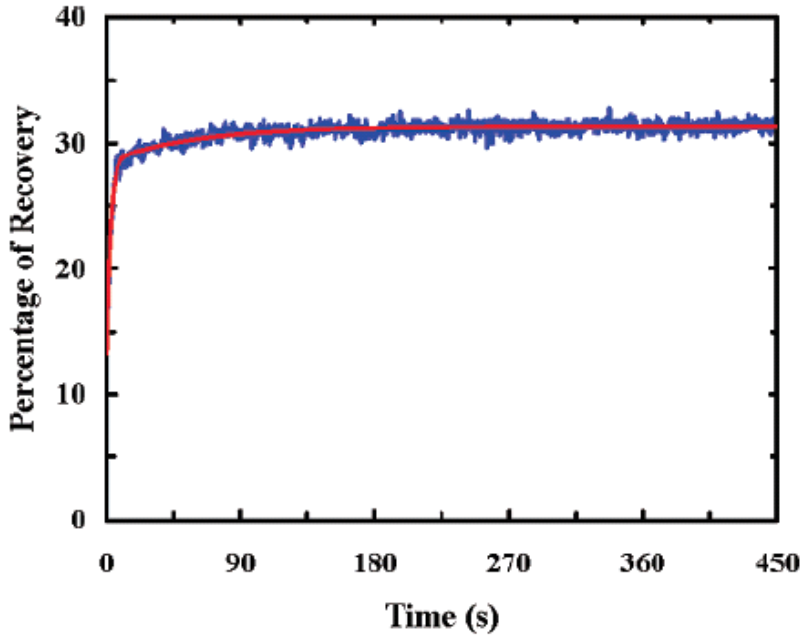

Figure 1.26 FRAP measurements of NR positioned at the center of the lipid nanotube. (Reproduced from reference [55])

This result is expected as the affinity towards the membranes is much higher in NR than R6G. In addition to FRAP experiments, FCS was performed to probe the diffusion of the R6G and mixtures of R6G and 1-anilino-8-naphthalene-sulfonate (ANS) inside the lipid tubules.

CHAPTER 2. SINGLE MOLECULE/PARTICLE DETECTION: INSTRUMENTATION BUILDUP AND SAMPLE PREPARATION

2.1 Introduction

Data collected from bulk experiments represent the average value or ensemble measurement of a given parameter of interest and yields a single observable. Such ensemble measurements give an accurate qualitative and quantitative picture in the case of homogeneous systems for which the events of interest occur in a time-synchronized fashion. However, many chemical and biological systems are in fact heterogeneous due to e.g. variations of the local environment at the molecular scale, variations in actual molecular behavior, or randomness in time of cycling through events by molecules in the ensemble. This concept is illustrated in Figure 2.1. Suppose the sample consists of an enzyme and the recorded signal (bulk measurement) represents the catalytic activity of the sample at a certain time. The data obtained from such an ensemble measurement represents the average value of many events, which is represented by the uniform grey color. However, the data obtained from bulk measurement does not provide detailed information on the possible scenarios described in Figure 2.1 a, b, and c. In scenario a, the enzymes all have the same catalytic activity thus each enzyme is represented as a grey circle (intermediate turnover). In scenario b, some fraction of the enzymes has very high catalytic activity (high turnover, black circles) while the rest of the enzymes show very low catalytic activities (low turnover, white circles). In scenario c, the catalytic activities of individual enzymes vary from one to another displaying different catalytic activities (low to intermediate to high turnover, white to grey to black circles).

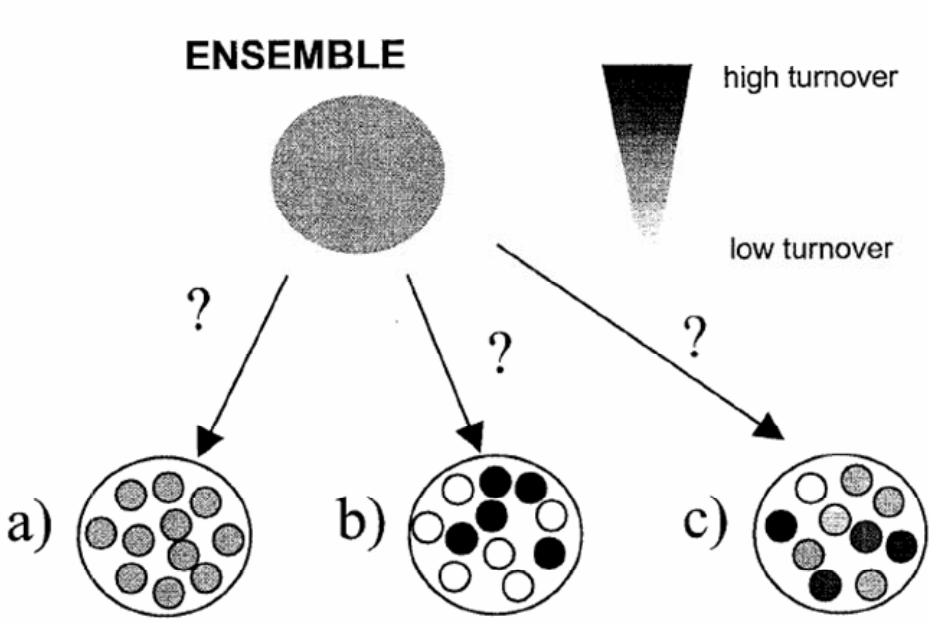

Figure 2.1 Schematic illustration of how single molecule spectroscopy experiments can be advantageous compared to bulk measurement. The sample is composed of an enzyme. In the bulk measurement, the average turnover rate is recorded and assumes that individual enzyme have the same turnover (a). However, it may be resulted from combination of some enzymes with high turnover and low turnover (b) or it may be resulted from combination of individual enzyme with various turnovers rates (c).

This example illustrates how detailed information such as distribution of quantities and time dependent molecular dynamic processes of a system can go undetected in ensemble measurements. Single molecule experiments allow us to examine one molecule at a time providing such information through direct measurements.

The single molecule spectroscopy technique was first introduced by Moerner and Kador in 1989 when these authors reported on the detection of the absorption signal of an individual molecule at cryogenic temperatures.[56] The use of low temperatures for measurements was motivated by the fact that the absorption cross section of a molecule is greatly reduced at room temperature, which led to a poor absorption signal of the molecules. Since then, there has been a rapid growth in the area of fluorescent detection

of single molecules at room temperature.[56] In particular, far-field confocal microscopy has been utilized widely due to its high optical throughput, three-dimensional imaging, and noninvasive detection. In addition to these attractive features, the simplicity of the experimental set up and the high sensitivity offer a powerful optical method to detect single molecules.[57,58]

2.2 Basic considerations for single molecule fluorescence detection

In order to detect signal from a single molecule at room temperature, there are several requirements one must consider. First, it must be guaranteed that only one molecule is in resonance in the volume probed by the laser. Second, the single molecule signal must be higher than the background signal providing a reasonable signal to noise ratio (SNR). This can be achieved by using a high photon collecting scheme and appropriate filtering of the detected signal in combination with highly sensitive detectors. Furthermore, the following parameters must be taken into a consideration: the focal volume must be small, the operating conditions should be below saturation of the molecular absorption, the molecule must have a large absorption cross section, high photostability, weak bottlenecks into triplet states (dark states), and a high fluorescence quantum yield.[57] Additionally, it is important to use ultrapure solvents and host matrix on a clean slide to prepare samples to minimize the signals from impurities. The detection of a single fluorophore in the focal volume can be achieved by focusing the laser beam to a small probe volume of 10 μm^3.[57] This tiny probe volume has an approximately cylindrical shape ($V = \pi r^2 h$) with a diameter of 0.5 μm (diffraction limited) and height of 2 μm (limited by spherical aberration).[58] The concentration of sample required depends on the

laser probe volume which varies from one to another but it is approximately 10^{-11} M. In our case, the sample concentration is approximately 5.0 x 10^{-12} M.

2.3 Photophysics of single molecules

Single molecules can be treated as a single quantum system, which is associated with a phenomenon known as photon bunching. In a three level system which includes ground state (S_0), singlet excited state (S_1) and triplet excited state (T_1), the molecule can emit photons from the S_1 to S_0 until the occupancy of T_1 via intersystem crossing.

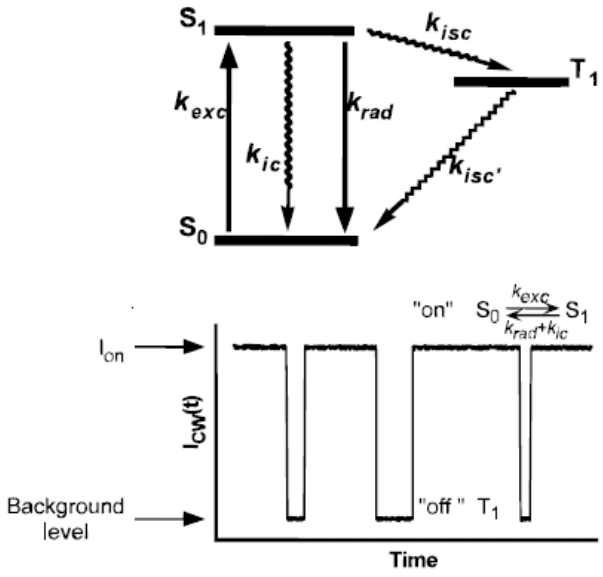

Figure 2.2 (Top) Jablonski diagram considering a simple three-level system for a single dye molecule. S_0 and S_1 represent the ground and excited single state respectively. T_1 represents the lowest excited triplet state. k_{exc} is the rate constant of excitation, k_{rad} is the rate constant of fluorescence and k_{ic} is rate constant of internal conversion. Conversion from S_1 to T_1 is called intersystem crossing. k_{isc} is the rate constant for the transition from S_1 to T_1 and $k_{isc'}$ is the rate constant for the transition from T_1 to S_0. (Bottom) Transient of a single dye molecule exhibits "on and off" behavior. The single dye molecule is on when the transition occurs from S_1 to S_0 while off when it goes from S_1 to T_1. (Reproduced from reference [59])

This represents a single quantum system in which the single molecule emits photons (S_1 to S_0) or no photons (S_1 to T_1 to S_0), on or off. This concept is illustrated in the Figure 2.2.

When the single molecule emits photons in bunch (photon bunching), an anti-bunching is expected within one bunch of photons emitted. This means that the photons within one bunch are not emitted simultaneously. In other words, the probability for two photons to arrive at the detector at the same time is zero. This concept is illustrated in Figure 2.3.

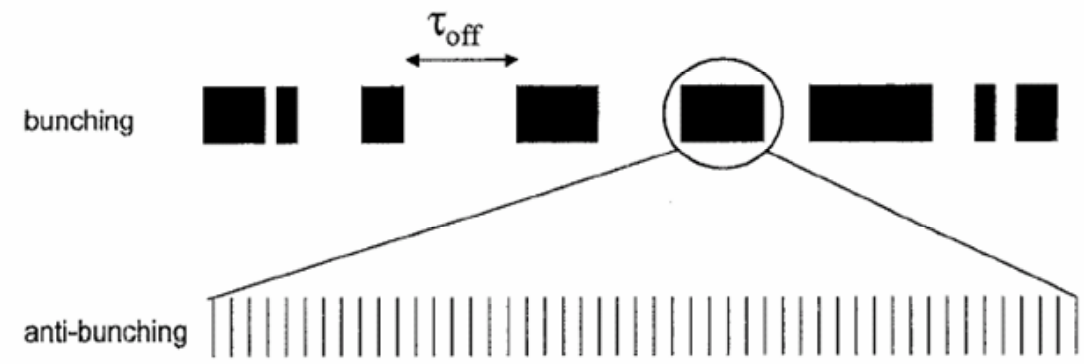

Figure 2.3 Schematic illustration of the photon bunching and anti-bunching. A single molecule acts as a single quantum system where the photon is on or off.

The amount of photons emitted from a molecule varies and depends on the system and the condition given. In single molecule spectroscopy, there is a special term used for photon bunching which is called blinking or flickering (fluorescence intensity intermittency). The phenomenon blinking can be i.e. due to the occupancy of the excited triplet state during which the molecule does not emit photons resulting in a dark period (off state), while in the absence of triplet state the molecule emits continuously (on state). This phenomenon is mostly reported in the literature for single dye molecule.[60-65] However, it is important to point out that the observation of blinking in a system does not indicate it is in fact a single chromophoric molecule since this behavior was also observed for coupled multichromophoric systems. How can one be certain that the detected signals are from single molecules and not from molecular aggregates or

artifacts? The following procedures are commonly used to resolve this issue: (a) The number of detected fluorescent spots in an image should scale approximately linearly with concentration, but the signal intensities should remain the same; (b) photobleaching should occur in an all or non fashion (single step photobleaching); (c) the recorded optical spectra may vary from molecule to molecule or from time to time because of environment perturbations such as spectral diffusion; (d) the signal dependence on excitation intensity should show saturation as expected for a single molecule; (e) the observed detection rate of fluorescence photons should not exceed the maximum rate (limited by the absorption/decay cycling of a single molecule); (f) the time correlation of the fluorescence signal should exhibit antibunching.[58]

2.4 Overview of SMS on Single and Multichromophoric Systems

In this section, literature examples of single molecule spectroscopy studies performed on single chromophoric systems and multichromophoric systems at room temperature are reviewed. Through the studies of fluorescent single dye molecules, unprecedented observations such as blinking (also known as quantum jumps) were observed. The explanation for this behavior is as a result of the population of the triplet state and no photon is emitted during this time period (dark period). In multichoromphoric systems, the molecules contain two or more chromophores therefore; one would expect exponential decay of fluorescence intensity as the individual chromophores emit photons independently from each other (Figure 2.4 a). However, interestingly, the experimental data of the multichromophoric systems such as dendrimers, oligomers, and conjugated polymers show characteristics of a single chromophoric system where discrete on-off jumps are predominant (Figure 2.4 b). The possible explanation for this unique

observation is due to the presence of the strong coupling between the chromophores and thus they act as a single quantum system. There are also uncoupled multichromophoric systems, but we are not going to review them since they are not extensively considered in the field.

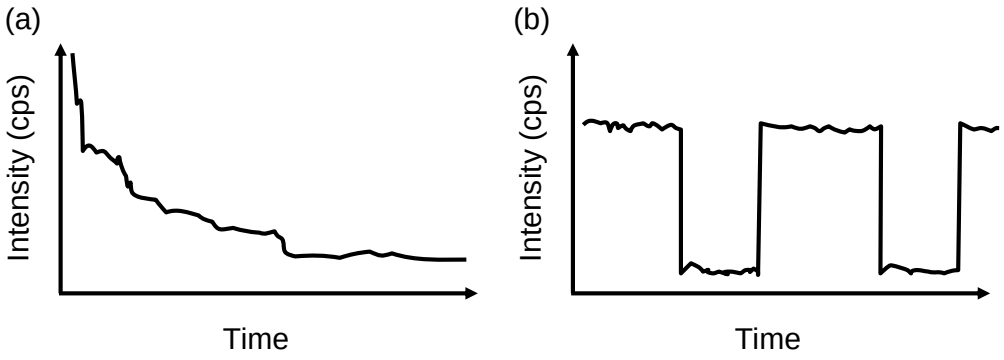

Figure 2.4 Schematic presentation of fluorescence transient for multichromophoric system. (a) Fluorescence transient displays exponential decay as the individual chromophores are emitting independently from each other. (b) Fluorescence transient displays single step blinking in which emission is resulted from strongly coupled chromophores that acts a single quantum system.

2.4.1 Single chromophoric systems

Many single fluorescent dye molecules were investigated to obtain their underlying photophysical processes. These dye molecules are excellent candidates to examine the occurrence of discrete on-off behavior (blinking) due to its occupancy of the triplet state via intersystem crossing. The first observation of the on-off behavior of the individual molecules was shown in experiments performed in cryogenic temperatures.[66-68] In these experiments, the fluctuation of the fluorescence intensity is described as quantum jumps and various triplet lifetimes and intersystem crossing rates of different molecules were obtained. Since these experiments were carried out at low temperature, researchers were

curious to see whether the quantum jumps of the individual molecules can be observed at room temperature. Ha et al. demonstrated the quantum jumps of single fluorescent dye (Texas Red) molecules that are link to individual DNA strands (TR-DNA) at room temperature.[62] The individual TR-DNA molecules that were adsorbed on dry surfaces showed different molecular emission intensities as function of time as shown in Figure 2.5. The result obtained from the experiment show the heterogeneity of the dye molecules due to the various local environment factors such as different concentration of oxygen. Veerman et al. investigated the triplet lifetimes and intersystem crossing yield of 1,1'-didocyl-3,3,3',3'-tetramethyl-indocarbocyanine perchlorate ($DiIC_{18}$) using near-field scanning optical microscopy (NSOM).[64] The $DiIC_{18}$ molecules were prepared in two different polymer matrices in which they were embedded in 10 nm of polymethyl methacrylate (PMMA) and polystyrene (PS). The NSOM fluorescence images of two different single $DiIC_{18}$ are shown in Figure 2.6. In this work, the triplet lifetimes and intersystem crossing yield of the $DiIC_{18}$ molecules were different for the polymer hosts PMMA and PS, demonstrating the sensitivity toward different environments on the molecular photophysical properties. It was noted that the various local oxygen concentrations in the polymer host was one of the main contribution for this inconsistency. Since the ground state triplet oxygen is well known to quench the triplet state of many aromatic dyes (triplet-triplet annihilation), it is important to investigate the photophysical processes of single dye molecules in absence of oxygen.[30, 35] Weston et al. investigated the triplet lifetimes of $DiIC_{12}$ molecules under vacuum condition (approximately 10^{-4} torr).[65]

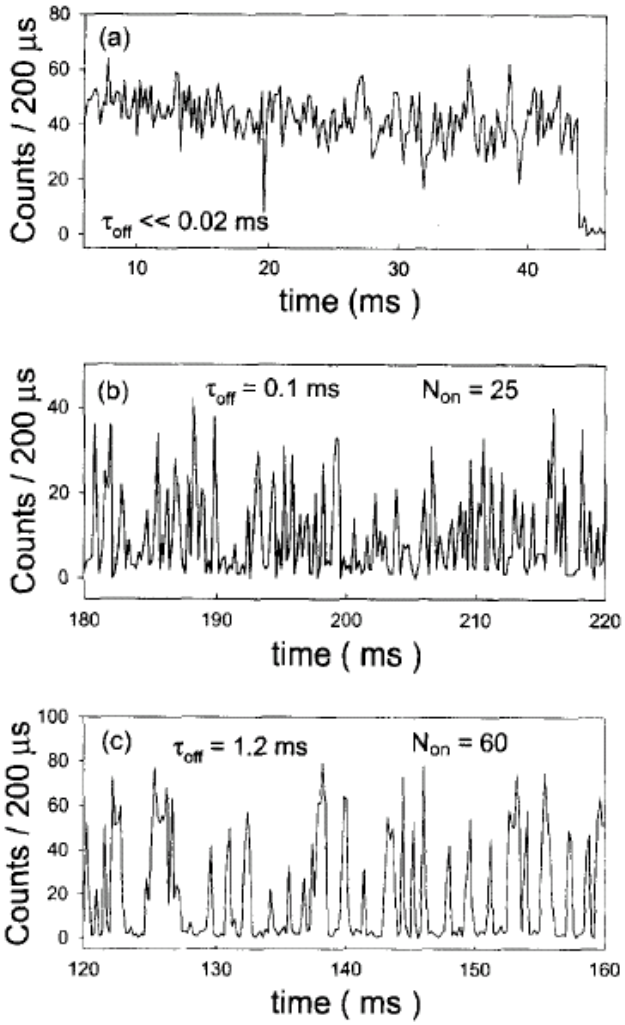

Figure 2.5 Total emission time trace for three individual TR-DNA molecules from the same sample. The emission intensity from one of the three molecules shows little intensity fluctuation (a) while the other two (b and c) show large fluctuation in emission intensity. N_{on} represents the on-state average counts and τ_{off} represents off-state lifetime. The bin size is 200 µs. (Reproduced from reference [62])

The observation of triplet state was more easily accomplished in this condition because the triplet lifetimes were longer (4-100 ms) and the rate of photobleaching was reduced by an order of magnitude compared to the ambient air environment. In this work, it was illustrated that there are one or more sudden fluctuations in the triplet lifetime and the intersystem crossing rate due to changing in molecular configurations. This imperative

information could not be shown due to the presence of oxygen in the sample in the previous studies. An example of the sudden fluctuations is shown in Figure 2.7.

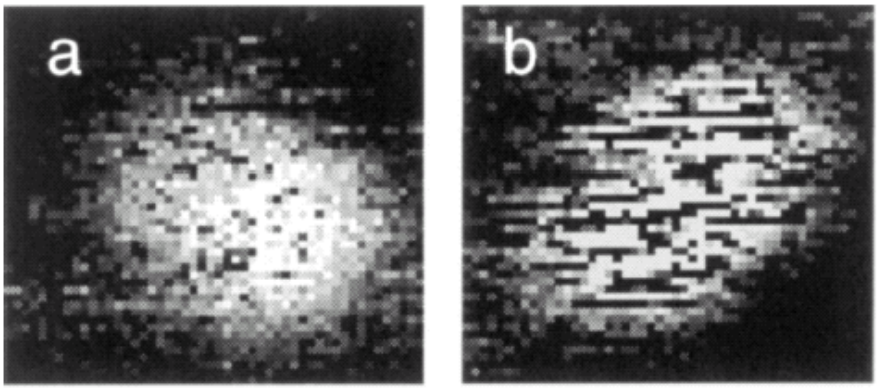

Figure 2.6 (a and b) NSOM fluorescence images of two different single $DiIC_{18}$ molecules embedded in 10 nm of PMMA layer. The presence of dark spots within the bright spot indicates that fluorescence is not continuous due to a temporal residence of the molecule in the triplet state. The triplet lifetime of the molecule (b) is longer than the molecule (a). (Reproduced from reference [64])

In the duration of 35 seconds (top panel), the molecule undergo 4 different transitions between configurations for which the on-off blinking rates are different. In this transient, the first, third, and fifth distinct periods can be attributed to the same molecular configuration. However, the molecule shows a long off state in the fourth period which represents a metastable dark state due to a tremendously small absorption cross-section or efficient non-radiative pathways as the deactivation process. The bottom panel shows the zoomed in view of the first transition.

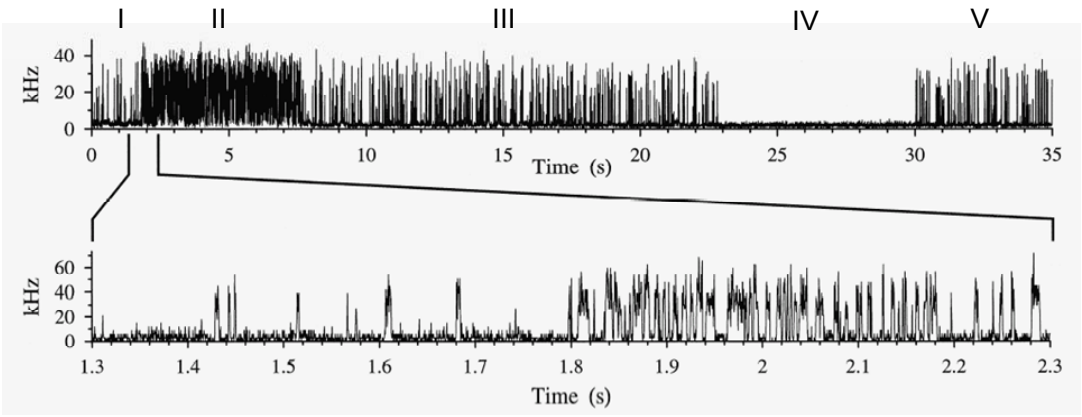

Figure 2.7 (Top) Emission intensity as function of time for a single dye $DiIC_{12}$ molecule. The emission intensity was measured for 35 s at bin size of 3.6 ms. (Bottom) Zoomed in view of the first transition between molecular configurations with bin size of 336 μs. (Reproduced from reference [65])

Kohn et al. performed single molecule experiment on five different cyanine dye molecules.[63] The studies divided into two parts. In the first part, the fluorescence trace intensities of molecules 1, 2 and 3 (Figure 2.8) were compared to investigate the internal heavy atom effect on single dye molecule. In the second part, molecules 1 and 5, which are only difference in the length of alkyl chains, were investigated to study the effect on the torsional motion which can cause a twisted geometry or even trans-cis isomerization leading to a non-radiative decay.

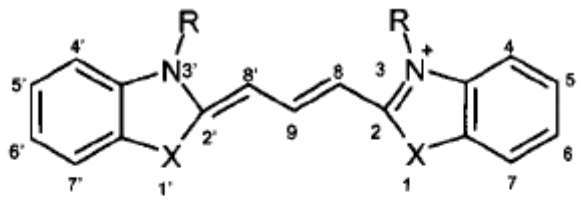

1: X= $C(CH_3)_2$; R=*n*-$C_{18}H_{37}$

2: X= S; R=*n*-$C_{18}H_{37}$

3: X= Se; R=*n*-$C_{18}H_{37}$

4: X= O; R=*n*-$C_{18}H_{37}$

5: X= $C(CH_3)_2$; R=*n*-C_3H_7

Figure 2.8 The molecular structures of variety cyanine dye molecules that are under investigation in the study. (Reproduced from reference [63])

From the first part of the experiment, it was found that the rate constants for intersystem crossing from triplet state to ground state for compounds 2 and 3 increased compared to compounds 1 and 5. Also, the quantum yield of intersystem crossing from singlet excited state to the triplet state show the same trend. It is important to note that this increase is due to the presence of a few much longer triplet lifetimes in the compound 2 and 3. This was explained in terms of the spin-orbit coupling where there is stronger spin orbit coupling in the compounds with the heavy atoms. The compound 4 was excluded from the data because it photobleached very fast, so no molecules survived for a long enough time to collect the data. For the second part of the experiment, the rate constants for the compound 1 and 5 are similar however, the quantum yield of the intersystem crossing is almost double for the compound 5. This was interpreted as an additional deactivation pathway due to compound 5 favoring a twisted state.

2.4.2 Multichromophoric systems

In the previous section, the discrete on-off (blinking) behavior was shown in single chromophoric systems. In this section, multichromophoric systems such as oligomers, nanoparticles, dendrimers and conjugated polymers are discussed.

Yip et al. investigated photophysical processes of the conjugated copolymer dPPV-PPyV (shown in Figure 2.9) using single molecules spectroscopy.[59]

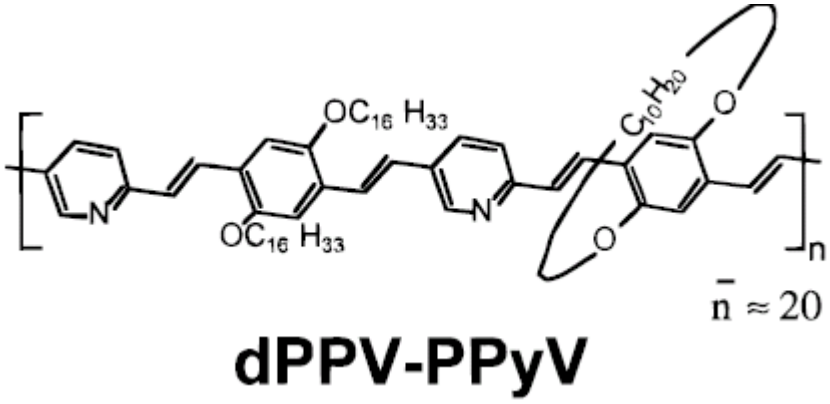

Figure 2.9 The molecular structure of conjugated copolymer dPPV-PPyV. (Reproduced from reference [59])

The fluorescence intensity trajectories of 4 different dPPV-PPyV single molecules are shown in Figure 2.10. As it can be seen in Figure 2.10, the individual dPPV-PPyV molecules exhibit distinctive fluorescence intensity fluctuations. Interestingly, discrete on-off intensity jumps are observed in the system. This was explained by efficient intramolecular energy transfer between different conjugated segments of the polymer which leads to efficient connection of all the segments (coupled chromophores). The polymer thus acts as a single quantum system. In addition, intermediate fluorescence intensity levels were observed for some molecules because the emission was as a result of two independent chromophore segments due to weak or no coupling between these segments.

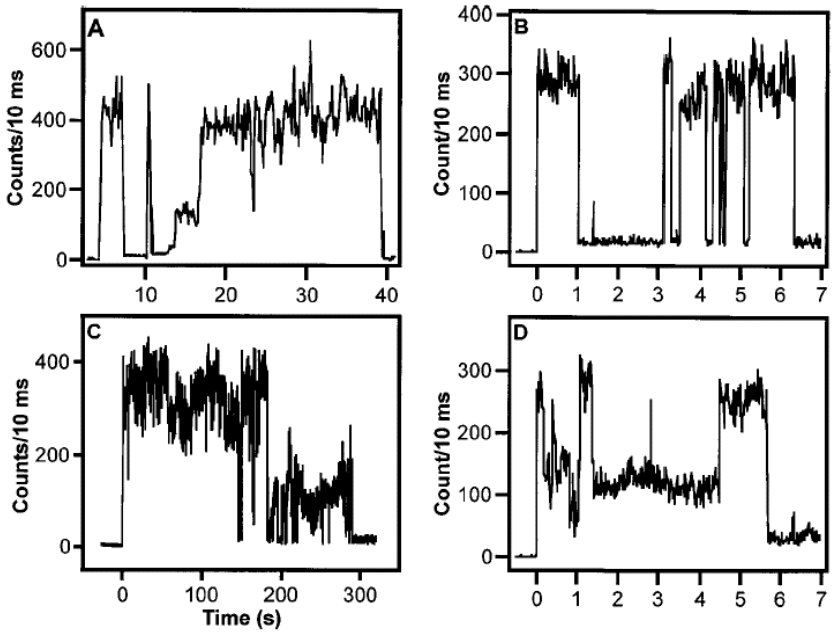

Figure 2.10 Transients collected from four individual dPPV-PPyV molecules. The bin size is 10 ms. (Reproduced from reference [59])

Ying et al. performed single molecule experiment to gain a better understanding of the underlying mechanism for the photochemistry and photophysics of single allophycocyanin (APC) trimers.[69] The APC trimers are composed of three αβ monomers and a schematic drawing of the structure is shown in Figure 2.11. The α or β polypeptide chain in each monomer unit is covalently bound with a phycocyanobilin (open-chain tetrapyrrole) chromophore through a cystein residue α84 or β84. When one of α84 in a monomer is positioned close to β84 in another monomer, a strong interaction occurs between them forming an aggregate.

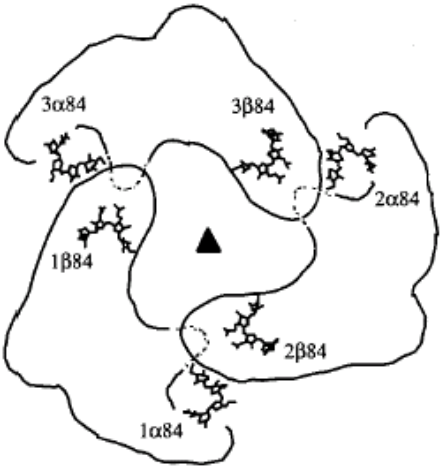

Figure 2.11 Schematic drawing of allophycocyanin trimers. (Reproduced from reference [69])

The fluorescence intensity trajectories of the different single APC trimer are shown in Figure 2.12.

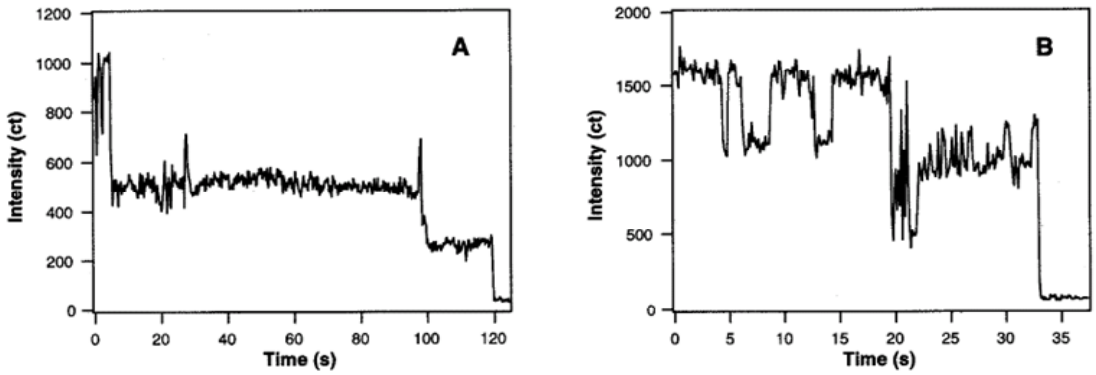

Figure 2.12 (a) Fluorescence trajectory of single APC trimers measured with excitation wavelength of 594nm at excitation power of 250 nW. (b) Another fluorescence trajectory of single APC trimers measured with excitation wavelength of 568 nm at excitation power of 500 nW. (Reproduced from reference [69])

In both cases, three different intensities are observed in the fluorescence intensity trajectories. The authors attributed the highest intensity to three emitting pairs in which each emitting pairs is strongly coupled between α84 and β84. The intermediate intensity

is assigned to two emitting pairs and the lowest intensity to only one emitting pair. The reason for quenching of the emission within a pair is due to the formation of photoinduced exciton traps within the strongly coupled α84 and β84 pairs.

Hofkens et al. performed a comparative study of individual multichoromphoric dendrimers that consist of eight perylenecarboximide chromophores at the rim with a model compound containing only one perylenecarboximide chromophore.[70] The structures of these dendrimers are shown in Figure 2.13.

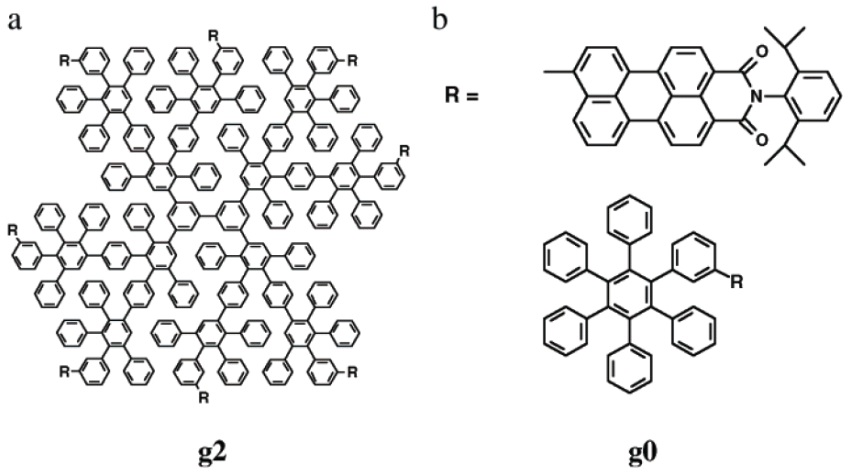

Figure 2.13 (a and b) Structures of the second-generation dendrimers (g2) and the model compound (g0). (Reproduced from reference [70])

The model compound (g0) shows three different types of fluorescence intensity trajectories which are shown in Figure 2.14. Sixty percent of the molecules exhibit single step photobleaching which is expected for a single chromophoric system. Thirty five percent of the molecules show the blinking phenomenon before irreversible photobleaching occurs. Lastly, five percent of the molecules have different emission intensity levels due to rotational diffusion of single molecules in the thin polymer film in which they are embedded.

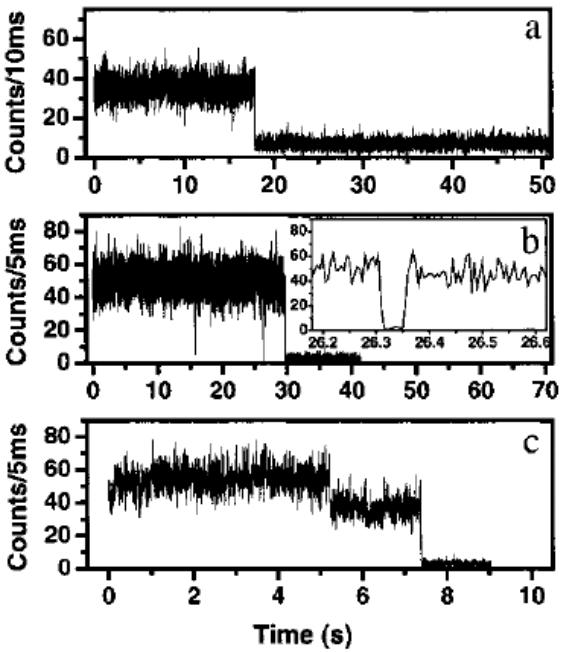

Figure 2.14 Fluorescence intensity trajectories of the model compound (g0) measured with excitation wavelength of 488 nm at excitation power of 350W/cm^2. (a) 60 % of the molecules exhibit single step photobleaching. The bin size is 10 ms. (b) 35 % of the molecules show more than one off periods. Inset displays the zoomed in view of the second off period in the fluorescence intensity trajectory. The bin size is 5 ms. (c) 5 % of the molecules show different intensity levels in the fluorescence intensity trajectory. The bin size is 5 ms. (Reproduced from reference [70])

The fluorescence intensity trajectories of the dendrimers (g2) were also collected using linear polarized and circular polarized excitation, as shown in Figure 2.15 a and b, respectively. The difference in excitation with linear and circular polarized excitation is that the circular polarized light accounts for the average z-orientation in addition to x- and y-orientations. As a result, all eight chromophores were monitored in the circular polarized excitation while only a fraction of the eight chromophores was monitored in with linearly polarized excitation. This can be observed in the Figure 2.15 b in which the fluorescence intensity trajectory collected using the circularly polarized shows longer average survival times (average survive time of 280 s vs. 450 s) and a higher number

photon counts on average (average photon counts of 7.9 x 10^5 vs. 11 x 10^5). As it can be seen in the inset of Figure 2.15 b, the off time varies from a few milliseconds to several hundreds milliseconds in the beginning of the transient.

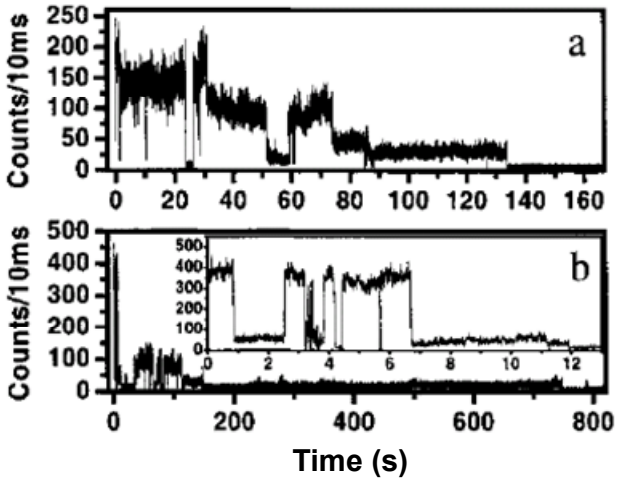

Figure 2.15 Fluorescence intensity trajectories of the dendrimer (g2) measured with excitation wavelength of 488 nm at excitation power of 350W/cm^2. (a) Fluorescence intensity trajectory recorded with linear polarized excitation (b) Fluorescence intensity trajectory recorded with circular polarized excitation. Inset shows the zoomed in view of the fluorescence trajectory at the beginning of the measurement. (Reproduced from reference [70])

However, a much longer off time of several seconds to tens of seconds can be observed towards the end of the transient. The fluorescence intensity trajectory from dendrimers (g2) displays more fluctuations in the fluorescence intensity compare to the model compound (g0). Most importantly, frequently blinking phenomena were observed as if it was a single chromophoric system. One possible explanation is that the eight chromophores are interacting with each other thus; they are strongly coupled via energy transfer and can act as a single quantum system, specifically when one of the chromophores goes to the triplet state.

White et al. studied fractionalized pristine poly(2,5-dioctyloxy p-phenylene vinylene) (DOO-PPV) in which there is only three chromophores in the system.[71] The fluorescence intensity trajectory representative of the most of the single polymers is shown in Figure 2.16. The fluorescence intensity can be seen as three discrete intensity levels. The interpretation of the data is as follows. After 330 ms, one of the chromophore undergoes triplet state and the emission is from two chromophores. At 13.5 s, the chromophore that was in triplet state returns to ground state and emits with the other two chromophores from the singlet excited state after that. Then one of the chromophores undergoes ISC to the triplet state at 20 s and recovers, resulting in the three chromophores emitting for about 30 s. Lastly, two chromophores are turned off and only one is emitting until the end of the recording. From this observation, they concluded that the structure of the polymer chain that was spin-casted maintained a rigid rod-like structure.

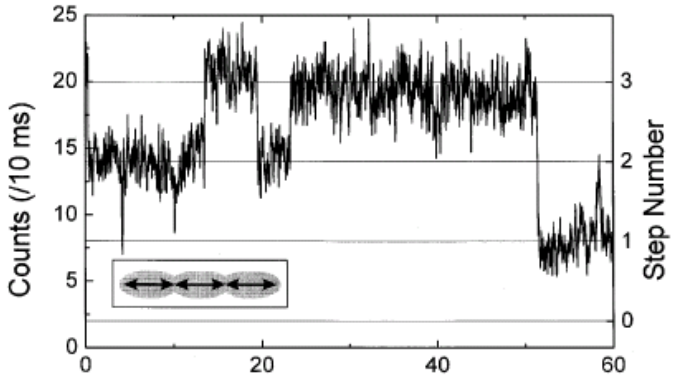

Figure 2.16 Transient of a defect free single DOO-PPV molecule. The excitation power of 200 W/m^2 is used. The bin size is 10 ms. Inset shows deduced conformation of the polymer. (Reproduced from reference [71])

2.5 Confocal Microscopy: construction of custom-built single molecule/particle detection setup

In confocal microscopy, a collimated laser beam of appropriate wavelength travels through a microscope objective lens which is focused to a diffraction limited spot at the sample plane. The diffraction limited spot diameter (D) depends on the excitation wavelength (λ) and the numerical aperture (NA) of the objective lens and the Equation 2.1 is given by [57]:

$$D = \frac{0.51\lambda}{NA} \qquad 2.1$$

Once the sample is excited, the emission from the sample passes through the microscope objective lens and photons are collected using APD or CCD. The fluorescence image of the sample is obtained using an avalanche photodiode (APD), a single photon counting detector and fluorescence emission spectra are collected using a spectrograph which is couple to a thermoelectrically cooled charge couple device (CCD). This is discussed in further detail in sections 2.5.3. A simplified schematic of the optical set up that was built in our lab is shown in Figure 2.17 and is discussed in detail hereafter.

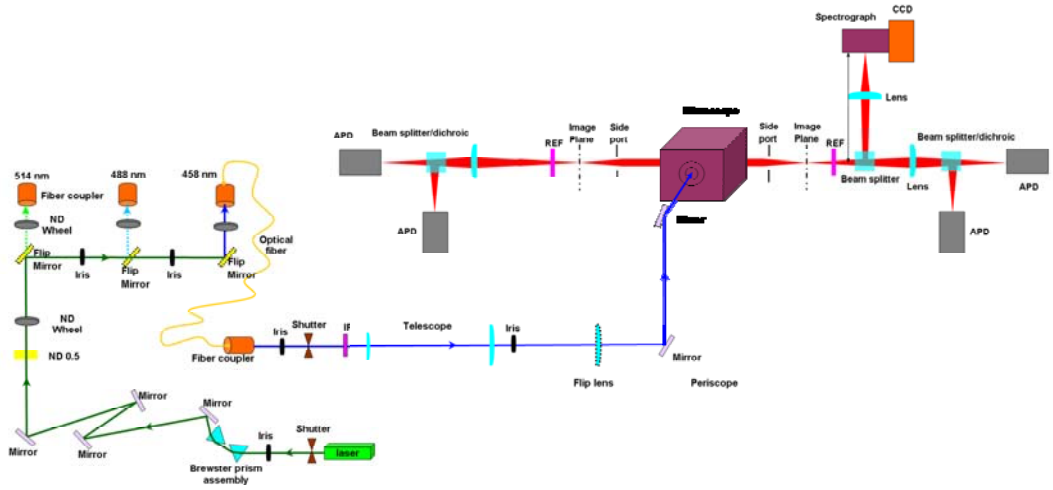

Figure 2.17 Schematic presentation of the whole optical table set up for a single molecule/particle spectroscopy experiment. The optical table is divided into three parts; the excitation, the microscope and the detection parts.

2.5.1 The excitation part

An argon-ion laser (Melles Griot 43 series) is used as the continuous wave (CW) excitation source. The laser lines include 457.9 nm, 488 nm, and 514.5 nm, which are separated with a double prism arrangement. The photograph of the double prism set up is shown in Figure 2.18.

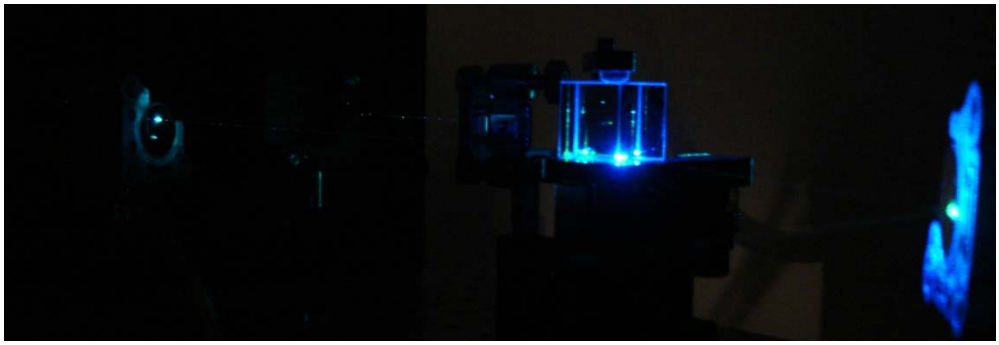

Figure 2.18 Photograph of Ar ion laser beam that is separated further apart by using double prism set up which is called Brewster prism assembly.

For the optical set up, a combination of optical fibers and fiber couplers with mirrors and irises are used to direct the laser beam into the backside of the microscope. This is a convenient way to direct the three different laser beams without needing a large optical table space or realignment of optics to guide the different beams into the microscope, and cleans up the beam profile if necessary. The intensity of the laser beam is controlled using a neutral density filter wheel. An interference filter further cleans up the laser beam. As an example the transmission spectrum of a 488 nm interference filter is shown in Figure 2.19

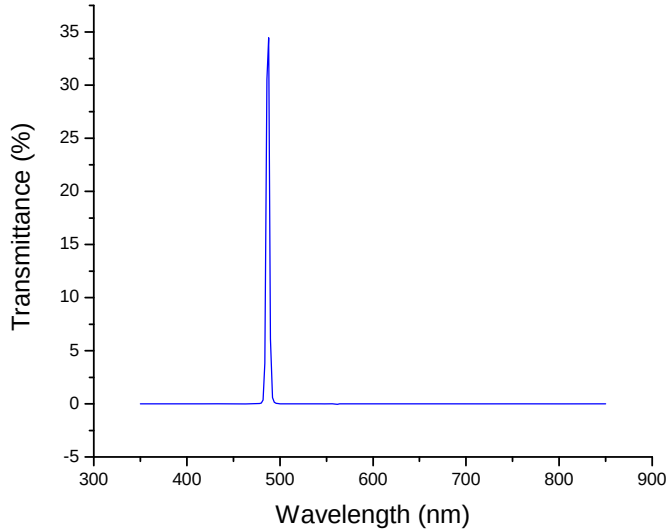

Figure 2.19 Transmission spectrum of a 488 nm interference filter which is used for the excitation wavelength of 488 nm.

A cartoon and photograph of the excitation part of the optical table is shown in Figure 2.20 and Figure 2.21 respectively.

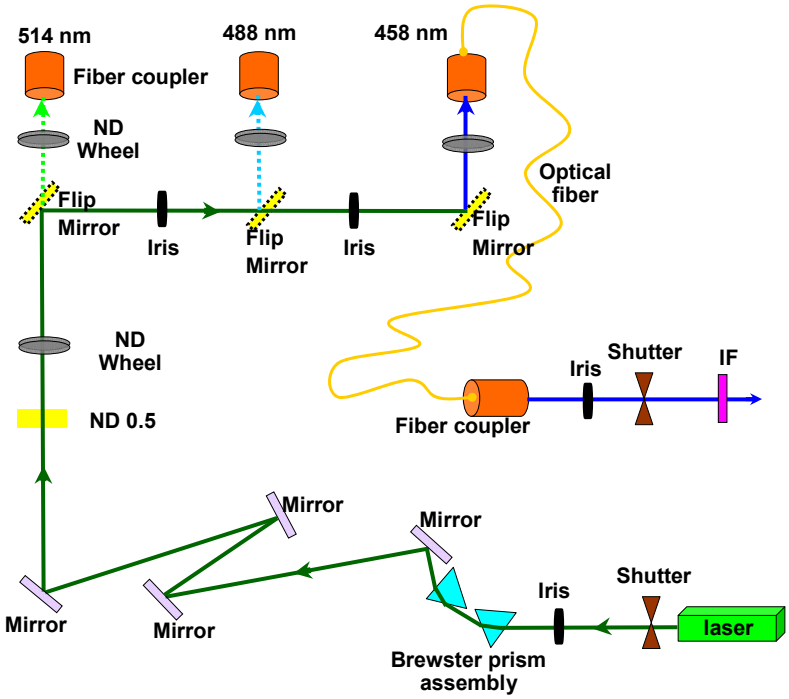

Figure 2.20 Schematic presentation of the excitation part on the optical table in which the laser source is directed to the microscope using mirrors, irises, filters, fiber couplers, and optical fibers.

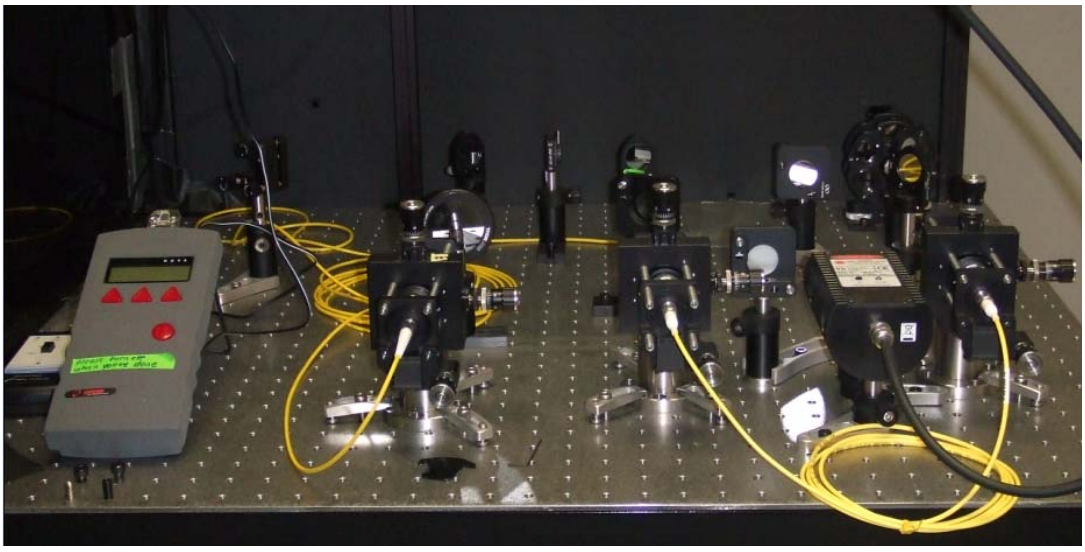

Figure 2.21 Photograph of the excitation part on the optical table in which the laser source is directed to the microscope using mirrors, irises, filters, fiber couplers, and optical fibers.

2.5.2 The microscope

A commercially available inverted microscope (Zeiss Axiovert 200) was modified to fit into the design of our experimental set up. The microscope is a sample scanning design, i.e. the sample is raster scanned in the X-Y direction across the focused laser beam using a Mad City Labs piezoelectric stage (Nano-LP100) that was incorporated onto the microscope body. The microscope is an inverted design, so both excitation and emission light travel through the same microscope objective lens. For the 488 nm laser line, which is used throughout the work reported in this dissertation, this is accomplished using a 495 nm dichroic mirror where the 488 nm laser line is able to reflect to the sample and the emission from sample is able to pass through the dichroic mirror and reach the detectors. The transmission spectrum of the 495 nm dichroic mirror is shown in Figure 2.22.

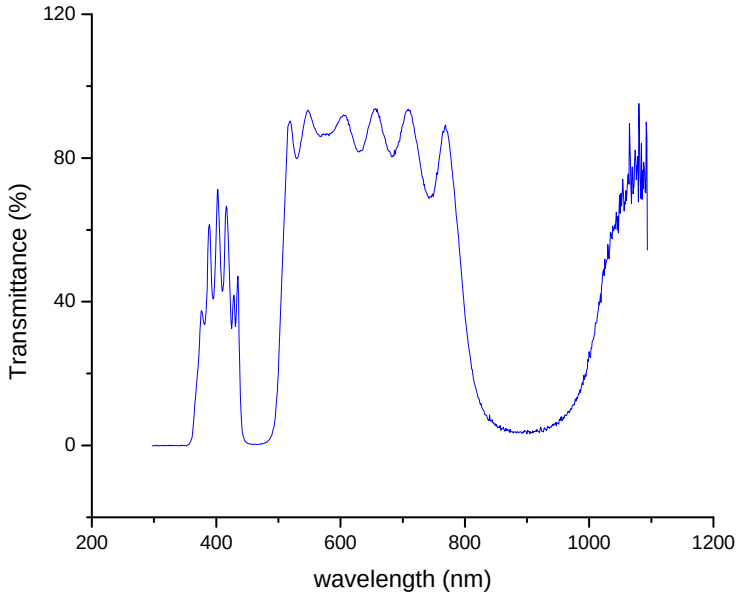

Figure 2.22 Transmission spectrum of a 495 nm dichroic mirror which is used for excitation wavelength at 488 nm.

The laser was focused to a spot size of approximately 300 nm using a Zeiss 100X Fluar objective lens (Magnification 100X, NA 1.3, WD 0.17 mm). There are two important parameters to consider for the objective lens. The first parameter is the numerical aperture (NA) which is determine by: $\eta \cdot \sin(\alpha)$ where η is the refractive index of medium (i.e. the objective lens is immersed in oil and the η is 1.518) and α is the half angle of light cone. The second parameter is the working distance (WD) which is the distance between the sample focal plane and the objective lens. A schematic representation of the half angle of light cone (α) and working distance is shown in Figure 2.23. A higher NA allows for a higher number of photons to be collected from the sample, however; the WD is decreased with increasing number of NA.

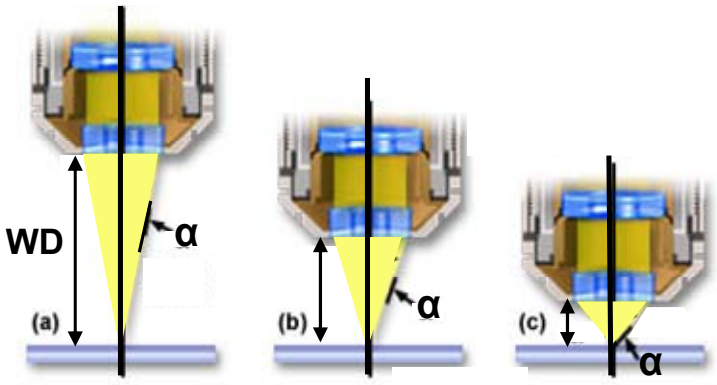

Figure 2.23 Schematic illustration of relationship between the working distance (WD) and the half angle of light cone (α). As the working distance decreases from (a) to (b) to (c), the half angle of light cone increases. As a result, the NA is increases in order of (a) to (b) to (c).

The Fluar objective lens provides high fluorescence throughput with fair color, field curvature and spherical aberration corrections.

2.5.3 The detection part

When the sample is raster scanned across the focused laser beam, a fluorescence image is created at the image plane which is located at the side port of the microscope in our case. The same image is collected (i.e. re-imaged) using optics at the APD (PerkinElmer SPCM-AQR-14) with 100X magnification. The detailed optical table set up is shown in Figure 2.24.

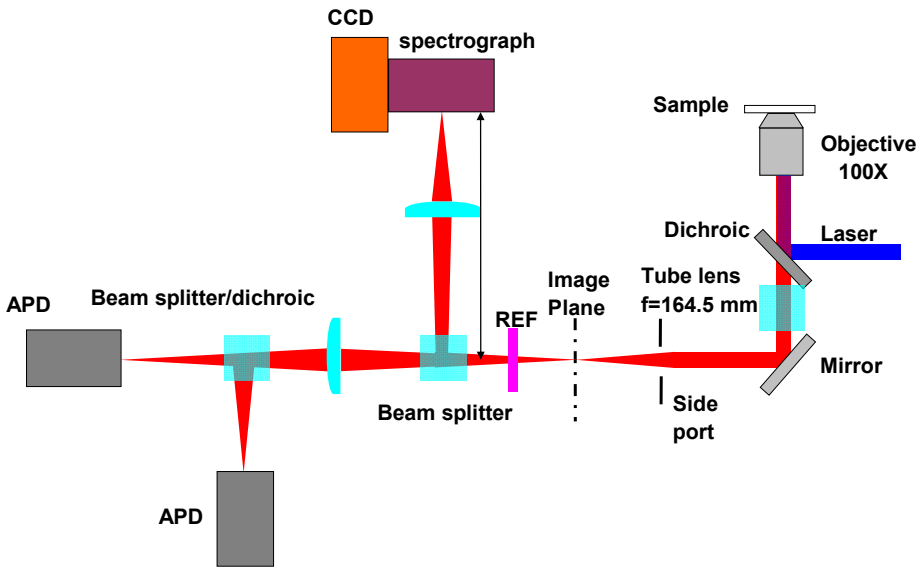

Figure 2.24 Schematic presentation of the microscope and detection parts on the optical table. The excitation wavelength is reflected into the sample and the emission light passes through the dichroic mirror which is directed either to the APD or CCD where photon is collected.

A 488 nm raman edge filter was used to remove scattered laser light from the fluorescence signal. The transmission spectrum of a 488 nm raman edge filter is shown in Figure 2.25.

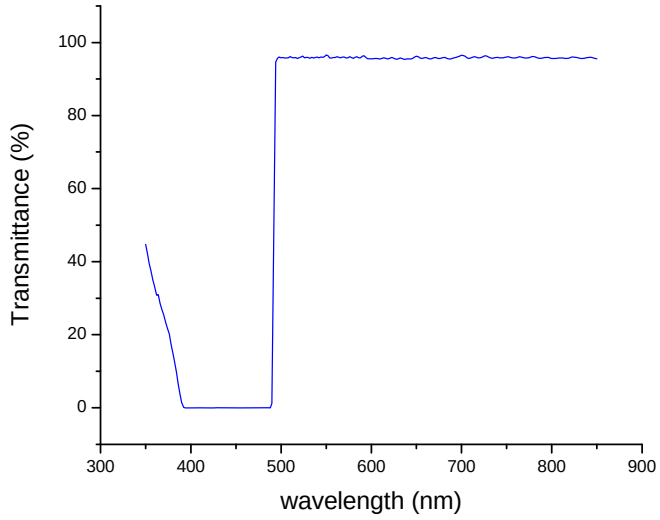

Figure 2.25 Transmission spectrum of a 488 nm raman edge filter which is used for the excitation wavelength of 488 nm.

Single particle emission spectra and transients (fluorescent intensity as function of time) are acquired by positioning the sample so that the laser beam is focused onto the fluorescent spots of interest that is observed in the previously scanned fluorescence image. Single particle fluorescence spectra are collected by a spectrograph (PI Acton SP-2156) with the grating (150g/mm blaze:500 nm) centered at 600 nm, which was coupled to a thermoelectrically cooled Electron Multiplying Charge Coupled Device (EM-CCD, Andor iXon EM + DU-897 BI).

2.6 Experimental procedures

2.6.1 Glass slide cleaning procedure

1. The glass slides are placed into a glass slide holder. The holder is placed in an amber jar filled with acetone and sonicated for 20 minutes.

2. Upon completion of sonication, the glass slides are rinsed with distilled water to remove the residual acetone.

3. The holder is placed in an amber jar filled with 10 wt % NaOH solution and sonicated for 20 minutes.

4. Upon completion of sonication, the glass slides are rinsed with distilled water to remove the residual NaOH solution.

5. The holder is placed in an amber jar filled with distilled water and sonicated for 20 minutes.

6. The distilled water is discarded and replaced with fresh distilled water for storage.

7. The cleaned glass slides from step 6 were blow dried with nitrogen before use.

8. We purchased a UV/Ozone cleaning system on March 23rd of 2009. From then on, we added a step where the nitrogen blow dried glass slides from step 7 are placed in the UV/Ozone cleaner for 15 minutes before use.

2.6.2 Purification of MEH-PPV

The 200,000 MW MEH-PPV contains residual low molecular weight polymers/monomers and other impurities which should be removed prior to use. The following procedure is used for the purification of a small amount of MEH-PPV.

1. A small amount of MEH-PPV (about 1 mg) is added to a glass vial followed by addition of about 1-2 mL HPLC grade acetone. The vial is gently heated at low temperature using a hot plate. The color of the solution is turned to yellow.

2. The acetone is carefully removed using a glass pipette making sure to avoid the MEH-PPV inside the vial.

3. A small amount of chloroform is added to the vial to dissolve the MEH-PPV. The solution is turned to an orange color. Into this vial, a large amount of acetone is added in which the ratio of chloroform and acetone is approximately 1:5. This solution is heated gently and is turned to a red colored suspension.

4. The suspension is transferred to a centrifuge tube and centrifuged for 3 minutes at 4000 rpm. The high molecular weight MEH-PPV is settled on the bottom of the centrifuge tube and the low molecular weight impurities is remained in the solution. The solution with the low molecular weight impurities is removed using a glass pipette.

5. Repeat steps 3 and 4. The color of the solution is almost clear or a light pink tint after repeating this step.

6. The centrifuge tube with the MEH-PPV is first covered with a parafilm and small holes are punctured for air circulation. Then it was vacuum dried for 30 minutes. Finally, the purified MEH-PPV is transferred to a vial for storage.

The absorption and fluorescence spectra of the MEH-PPV impurities in acetone are shown in Figure 2.26. The maximum absorption and emission peaks are 486 nm and 551 nm respectively. The maximum absorption peak of the impurities in acetone is blue-shifted compare to maximum absorption peak of the purified MEH-PPV in THF (λ_{max} = 500 nm). The maximum emission peak of the impurities in acetone is comparable to purified MEH-PPV in THF (λ_{max} = 553 nm). However, the emission spectrum obtained from the impurities shows very broad and structureless shape.

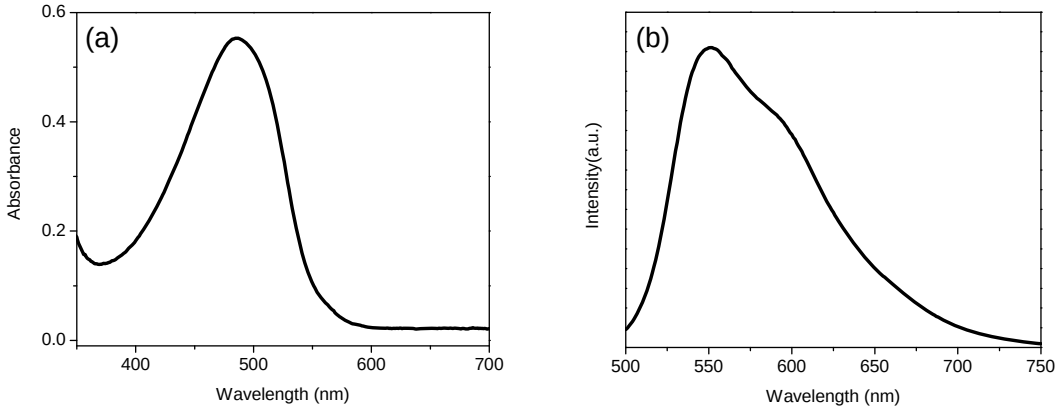

Figure 2.26 (a) UV-Vis absorption spectrum of MEH-PPV impurities in acetone obtained from purification step 2. (b) Fluorescence spectrum of MEH-PPV impurities in acetone obtained from purification step 2.

2.6.3 Nanoparticle fabrication

Materials. MEH-PPV, PCBM, and THF (anhydrous, 99.9 %) were purchased from Sigma Aldrich. MEH-PPV was purified by hot acetone wash before use. Aluminum (99.99 %) pellets for thermal deposition were purchased from CERAC Inc.

Nanoparticle preparation. We prepared approximately 30 nm MEH-PPV/PCBM composite nanoparticles consisting of approximately 20-50 MEH-PPV molecules using the reprecipitation method. This method was first introduced by Nakanishi and has since been modified for the preparation of various nanoparticles by different groups.[48,49,72-74] This method has now been extended for the preparation of composite nanoparticles of electron donor-acceptor molecules, as shown in Figure 2.27.

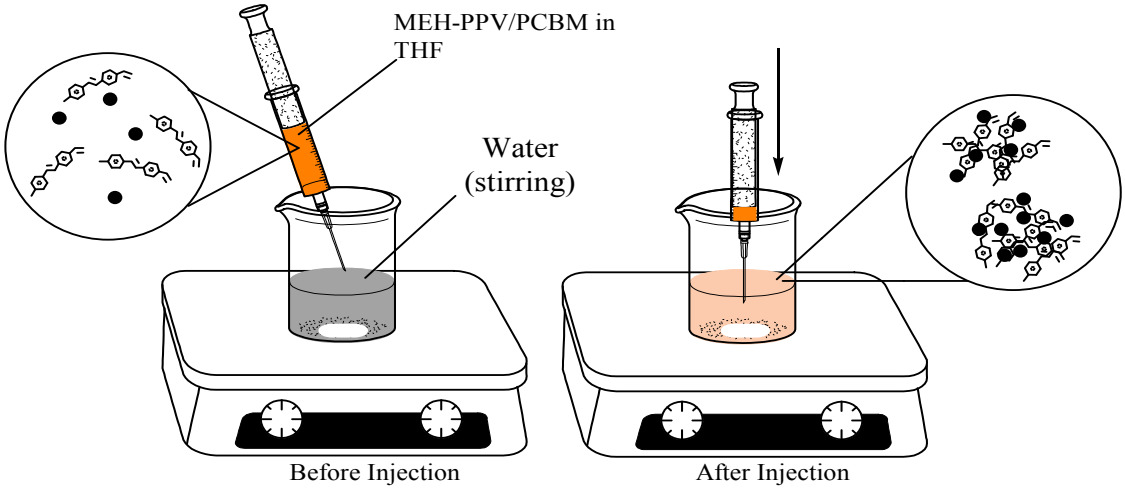

Figure 2.27 Schematic illustration of the reprecipitation method, a simple solution processing technique in which a solution of organic material in good solvent is injected into a very poor solvent for the organic material. The materials are first dissolved in a good solvent (THF) that is miscible with water. Then the THF solution (1 mL) is rapidly injected into 4 mL water, leading to a quick aggregation of the materials. For the preparation of MEH-PPV nanoparticles doped with 5, 50, and 75 wt % PCBM, the same procedure is followed except that the appropriate amount of PCBM is first added to the MEH-PPV solution prior to injection into water.

MEH-PPV with molecular weight of approximately 200,000 amu is purchased from Sigma Aldrich and is further purified by hot acetone wash. The purification procedure is discussed in section 2.6.2. A small amount of the purified MEH-PPV is dissolved in THF (anhydrous, 99.9%) and the absorption spectra of this solution is obtained. The solution is diluted by adding THF until the concentration of the solution is 10^{-9} M. The nanoparticles are prepared by a reprecipitation method in which the MEH-PPV is dissolved in a good solvent (i.e. THF) then injected into a poor solvent (i.e. H_2O). The nanoparticles are prepared by weighing 4 grams DI water into an 8 mL vial using an electronic balance (Cary 300). To this vial, a magnetic stirrer is added and placed on a stir plate. Using a syringe, 1 mL of MEH-PPV in THF (concentration of 10^{-9} M) is measured and quickly injected into the vial while it is stirred vigorously. Then 20 μL of this suspension is

dissolved in 1 mL of 4 % polyvinyl alcohol (PVA) and is spin-coated onto a clean slide for 1 min at 2000 rpm. For the MEH-PPV nanoparticles doped with PCBM followed the exact same procedure except that the appropriate weight percentage of PCBM (i.e. 5, 25, 50, 75 wt %) is added to MEH-PPV in THF before injecting into the water. An example of sample calculation for the amount of PCBM needed to achieve the 5, 25, 50, and 75 wt % is shown below:

1. Determine the concentration of diluted solution which was prepared by taking 50 μL of MEH-PPV in THF (molecular solution) and dissolve in 3 mL of THF. Absorbance of diluted MEH-PPV in THF is obtained.

A = abC (where a = molar absorption coefficient (L/mol*cm), b = absorption path length (cm), and C = concentration (mol/L)
$0.15 = (3.0 \times 10^{7})(1)C$
$C = 5.0 \times 10^{-9}$ M
Therefore, the concentration of the diluted molecular solution is 5.0×10^{-9} M.

2. Calculate the concentration of the MEH-PPV in THF (molecular solution).

$M_1V_1=M_2V_2$
M_1 (50 μL) = (5.0×10^{-9} M)(3050 μL)
$M_1 = 3.05 \times 10^{-7}$ M
Therefore, the concentration of the molecular solution is 3.05×10^{-7} M.

3. Calculate the grams of MEH-PPV in the MEH-PPV in THF.

$$1000\ \mu L \text{ of MEH-PPV in THF} \times \frac{1 L}{10^{6}\ \mu L} \times \frac{3.05 \times 10^{-7}\ mol}{1 L} \times \frac{1 \times 10^{6}\ g}{1\ mol} = 3.05 \times 10^{-4} g$$

Therefore the grams of MEH-PPV is 3.05×10^{-4} g.

4. Calculated how many grams of PCBM is needed to achieve 5, 25, 50, 75 wt %.

$$\frac{x\ g \text{ of PCBM}}{3.05 \times 10^{-4}\ g \text{ of MEH - PPV}} \times 100\ \% = 5\ wt\ \%$$

Solve for x to get the grams of PCBM needed for 5 wt % and the same calculation can be applied for 25, 50, and 75 wt %. Therefore, 1.525×10^{-5} g of PCBM is needed.

5. Weight out a certain amount of PCBM and dissolve it in 500 μL of THF. From this, calculate the concentration of PCBM in THF. For example, 0.0014 g of PCBM is weighed out.

$$0.0014\text{g PCBM} \times \frac{1\text{mol}}{910.88\text{g}} \times \frac{1}{500\ \mu\text{L}} = 3.07 \times 10^{-9}\ \text{mol/μL}$$

The concentration of the PCBM in THF is 3.07×10^{-9} mol/μL.

6. Calculate μL of PCBM in THF needed to achieve 5, 25, 50, 75 wt %. Add the amount of PCBM in THF to MEH-PPV in THF before injection into water to make the doped nanoparticles.

$$1.525 \times 10^{-5}\ \text{g PCBM} \times \frac{1\text{mol}}{910.88\text{g}} \times \frac{1\mu\text{L}}{3.07 \times 10^{-9}\ \text{mol}} = 5.45 \times 10^{0}\ \mu\text{L}$$

To prepare 5 wt % PCBM doped nanoparticles, 5.45 μL of PCBM in THF was added to 1 mL of MEH-PPV in THF first before injection into water. The amount of PCBM in THF needed for 25, 50, and 75 wt % is as follows in this calculation: 25 wt % PCBM (27.25 μL), 50 wt % (54.50 μL) and 75 wt % (81.75 μL).

2.6.4 Nanoparticle characterization

Dynamic Light Scattering (DLS)

The undoped and doped nanoparticle suspensions in water were diluted by placing a drop of the suspension into a 1 cm quartz cuvette and subsequent addition of DI water to the cuvette. Thirty trials were ran (with 30 runs per trial) using a Precision Detector 2000DLS. These values were averaged and standard deviation was calculated.

Transmission Electron Microscopy (TEM)

The diameter of the undoped and doped nanoparticles was determined using transmission electron microscopy (TEM, Phillips Tecnai F 30). A drop of the nanoparticle suspension was placed on a TEM grid and vacuum dried before imaging.

Atomic Force Microscopy (AFM)

Atomic Force Microscopy was ran on a Digital Instruments Multimode and Dimension 3100 system with NanoscopeIIIa controller. After dilution, undoped and doped nanoparticle suspensions in water were dropped onto freshly cleaved mica substrates. These samples were vacuum dried for 15 minutes before imaging.

2.6.5 Bulk solution spectroscopy

UV-Vis

The UV-Vis absorption spectra were taken using a 1 cm path length quartz cuvette with a Varian Cary 300 Bio UV-Vis scanning spectrometer.

Fluorescence

Fluorescence emission spectra were taken using a 1 cm path length quartz cuvette with a Nanolog^{TM} HoribaJobin Yvon fluorimeter. The excitation wavelength was set at 488 nm. The excitation and emission slits were 2 nm.

2.6.6 Single particle imaging and spectroscopy

Samples were prepared by spincoating a solution of nanoparticles in 4 wt % polyvinylalcohol (PVA, Sigma Aldrich) solution at 2000 rpm for 60 seconds on glass cover slides. The samples were sealed from oxygen by thermal evaporation of 200 nm of aluminum on top of the PVA/nanoparticle films. Single particle fluorescence images and spectra were acquired using a home build sample-scanning confocal microscope. The 488 nm line of argon-ion laser (Melles Griot 43 series) was used as the excitation source. Undoped nanoparticle samples were typically excited with 0.72 W/cm^2 laser power, while doped nanoparticles were investigated with a 10-fold larger laser power (7.2 W/cm^2). The laser was focused to a spot size of approximately 300 nm using a Zeiss

100X Fluar objective lens (NA 1.3, WD 0.17 mm). The sample was raster scanned across the focused laser beam using a Mad City Labs piezoelectric stage (Nano-LP100) to create a fluorescence image of the sample. The single particle fluorescence was detected using an avalanche photodiode (PerkinElmer SPCM-AQR-14). Single particle fluorescence spectra were obtained by a spectrograph with the grating (150 g/mm blaze: 500 nm) centered at 600 nm (PI Acton SP-2156) which was coupled to a thermoelectrically cooled Electron Multiplying Charge Coupled Device (EM-CCD, Andor iXon EM+ DU-897 BI). Each fluorescence spectrum was collected with 10 s exposure times with three consecutive exposures and then averaged.

2.6.7 Franck-Condon analysis

Procedures for preparation, characterization and fluorescence imaging of composite MEH-PPV/PCBM nanoparticles have been previously reported in detail.[75] Briefly, nanoparticles are prepared via the reprecipitation method yielding a nanoparticle suspension in water. Reported Transmission Electron Microscopy (TEM) images of the nanoparticles were collected with a Phillips Tecnai F 30 high resolution instrument. Samples for SPS were prepared by adding a drop of the nanoparticle suspension in water to a 4 wt % polyvinylalcohol (PVA, Sigma Aldrich) solution in water followed by spincoating at 2000 rpm for 60 seconds on glass cover slides. The samples were protected from the atmosphere by a 200 nm aluminum film deposited on top of the PVA/nanoparticle films by thermal evaporation. Single particle fluorescence images and spectra were acquired using a home built sample-scanning confocal microscope under 488 nm laser excitation.[75] Undoped nanoparticle samples were typically excited with 0.72 W/cm^2 laser power, while doped nanoparticles were investigated with a 10-fold larger

laser power (7.2 W/cm^2). The Franck-Condon analysis was completed using a home written program in the Matlab (The MathWorks Inc., Natick, Massachusetts) environment. For our analysis, we used 2 vibrational modes with three vibrational quanta (n = 0, 1 and 2) and the following assumptions were made for the emitters; each stick spectrum for a given emitter is broadened by a Gaussian that has the same width σ for each vibrational mode, each vibrational mode has the same Huang-Rhys factors (S) for the vibrational quanta, and the emitters are coupled with vibrational modes in the 1000-1600 cm^{-1} region. All parameters were free to vary during non-linear least-squares fitting of model to data.

2.6.8 Electric field device fabrication

The device is prepared as described in the following. The glue was applied to indium tin oxide (ITO) glass substrate to mask ITO from gold providing a good contact with gold without creating a short circuit. The SiO_2 layer is deposited as an insulating layer. The lower PMMA layer is spin-coated to separate the SiO_2 layer with the nanoparticles layer.

1. Glue is prepared by mixing a 1 mL of bond and a drop of the catalyst that comes in a kit. The glue is applied to the two edges of a clean ITO glass slides (the cleaning procedure for the ITO glass is the same as a glass slide). The glued ITO slides are placed in oven for 1 hour at 100 °C. The glue is completely dried.

2. Onto the glued ITO glass slides, 200 nm of SiO_2 is deposited using electron beam evaporator.

3. Onto the ITO/SiO_2 glass slide, 6 % PMMA (in toluene) is spin-coated at 2000 rpm for 1 min followed by drop cast of MEH-PPV nanoparticles in 4 % PVA (20 μL of MEH-PPV nanoparticle sample in 1 mL of 4 % PVA). This is spin-coated at 400 rpm for 18

seconds followed by increasing the spin-speed to 2000 rpm and spin-coated for another 1 minute. Lastly, 6 % PMMA (in toluene) is spin-coated at 2000 rpm for 1 minute.

4. The same procedure is followed for the sample with 50 wt % PCBM doped MEH-PPV nanoparticles.

5. Approximately 100 nm of aluminum or gold is deposited onto the samples obtained from step 3 using thermal evaporator.

6. Silver paste and epoxy is mixed together to form adhesive. This adhesive is used to attach the copper wires onto the samples prepared in step 5. Once the copper wires are attached, the samples are vacuum dried for 5 hours.

7. The samples from step 6 are transferred to the glove box for storage.

The Figure 2.28 shows the actual photograph of device prepared from the procedures described above.

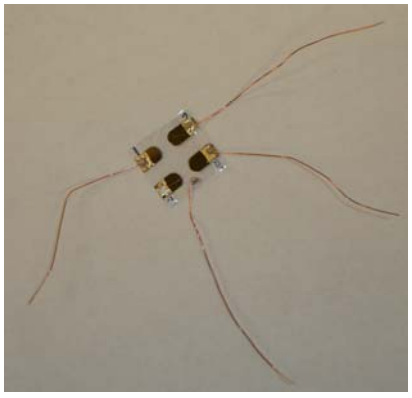

Figure 2.28 Photograph of the actual device that is prepared in the following order (bottom to top): ITO glass substrate, SiO_2, PMMA, MEH-PPV nanoparticles in PVA, PMMA, and gold.

The device is placed on the sample scanning confocal microscope described in section 2.5. The leads of the device are connected with alligator chips to an adapter attached to a

BNC cable which is connected to a function generator. A repetitive triangle waveform is applied to the device during the recording of the transient of the individual nanoparticles. The schematic of the optical set up used for this experiment is shown in Figure 2.29.

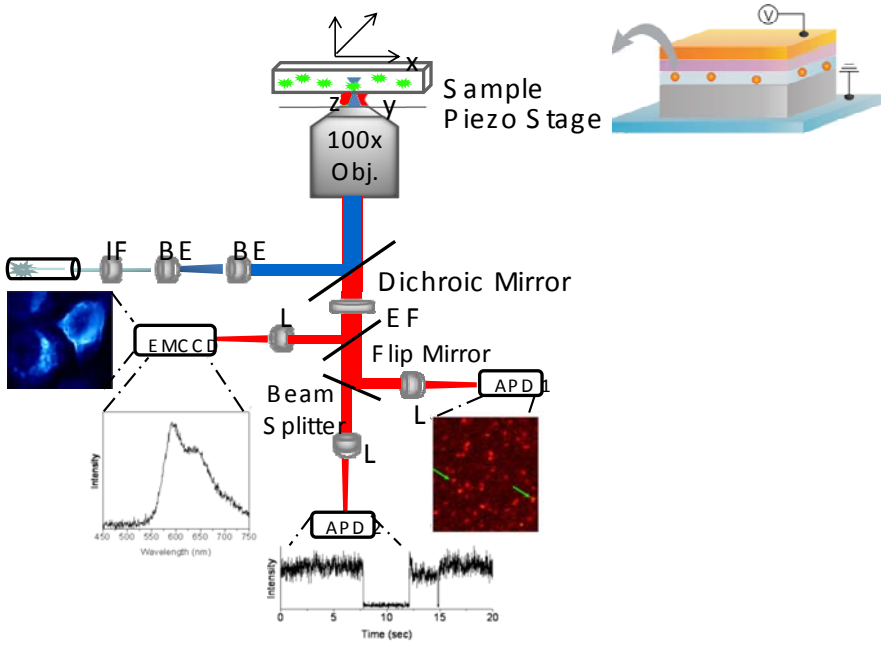

Figure 2.29 Schematic diagram of the single particle microscopy for the device experiment.

The device is placed in the sample stage and voltage is applied to the device through the wires. The fluorescent confocal images, the transient, and the spectra can be obtained.

2.6.9 MEH-PPV nanoparticles inside hollow lipid nanotubes

The samples were prepared in different ways for performing the experiment. Each condition will be described in the following.

Sample 1 preparation

1. The $DC_{8,9}PC$ lipid nanotubes sample is diluted by adding 2 μL of the sample into 40 μL of DI water. And 6 μL of this diluted sample is dropped onto three clean slides and air

dried until the water is removed then they are vacuum dried for 1 hour in a descicator. The samples are transferred to the glove box and stored it for 5 days. By preparing this way, the $DC_{8,9}PC$ lipid nanotubes are dehydrated. One of the dehydrated $DC_{8,9}PC$ lipid nanotubes samples is kept as it is and the other two dehydrated $DC_{8,9}PC$ lipid nanotubes samples are prepared as in the following steps.

2. Onto the dehydrated nanotubes glass slide, 40 μL of MEH-PPV nanoparticles (without dilution) is drop cast and air dried for 20 minutes.

3. The remaining nanoparticles suspension is removed by dipping the sample 15 times into DI water very carefully.

4. The wet sample is placed on a chemwipe and air dried until it is completely dried.

5. To prepare the reference for this sample, the same steps from 2 to 4 is followed except for the drop cast of the MEH-PPV nanoparticles, 40 μL DI water is dropped onto the dehydrated $DC_{8,9}PC$ lipid nanotubes sample instead.

Sample 2 preparation

1. The $DC_{8,9}PC$ lipid nanotubes sample is diluted by adding 2 μL of the sample into 40 μL of DI water. And 6 μL of this diluted sample is dropped onto four clean slides and air dried until the water is removed then they are vacuum dried for 1 hour in a descicator. The samples are transferred to the glove box and stored it for 5 days. By preparing this way, the $DC_{8,9}PC$ lipid nanotubes are dehydrated. One of the $DC_{8,9}PC$ lipid nanotubes samples is prepared as a reference and the other three dehydrated $DC_{8,9}PC$ lipid nanotubes samples are prepared as in the following steps.

2. Onto the dehydrated $DC_{8,9}PC$ lipid nanotubes sample glass slide, 40 μL of diluted MEH-PPV nanoparticles is drop cast and air dried for 20 minutes. Three dilutions of

MEH-PPV nanoparticles are prepared. They are: (a) 40 μL of the MEH-PPV nanoparticles in 20 μL of DI water. (b) 40 μL of MEH-PPV nanoparticles in 40 μL of DI water. (c) 40 μL of MEH-PPV nanoparticles in 80 μL of DI water.

3. The remaining MEH-PPV nanoparticles suspension is removed by dipping the sample 15 times into DI water very carefully.

4. The wet sample is placed on a chemwipe and air dried until it is completely dried.

5. To prepare the reference for this sample, the same steps from 2 to 4 is followed except for the drop cast of the MEH-PPV nanoparticles, 40 μL DI water is dropped onto the $DC_{8,9}PC$ lipid nanotubes sample instead.

Sample 3 preparation

1. The $DC_{8,9}PC$ lipid nanotubes sample is diluted by adding 2 μL of the sample into 40 μL of DI water.

2. A silicone isolator is attached onto a clean glass slide, and 6 μL of the diluted $DC_{8,9}PC$ lipid nanotubes sample is dropped into the well and air dried until the water is removed. It is followed by vacuum dry for 1 hour in a descicator. The sample is transferred to the glove box and stored it for 5 days. By preparing this way, the $DC_{8,9}PC$ lipid nanotubes are dehydrated. The dehydrated $DC_{8,9}PC$ lipid nanotubes sample is rehydrated which is described in the following steps.

3. Into the well of the dehydrated $DC_{8,9}PC$ lipid nanotubes sample glass slide, 20 μL of diluted MEH-PPV nanoparticles is drop cast and incubated for 5 minutes. The dilution of the MEH-PPV nanoparticles is achieved by adding 2 μL of the MEH-PPV nanoparticles sample into 100 μL of DI water.

4. The remaining MEH-PPV nanoparticles suspension is removed by dipping the sample 20 times into DI water very carefully.

5. The wet sample is placed on a chemwipe and the excess water is removed. The sample is then air dried for 5 min. Note: After 5 min, the water is still remains in the well of the sample.

6. A clean glass slide is attached on top of the silicone isolator keeping the water inside the well and as a result, the nanotubes are kept hydrated while performing the experiment.

The sample is placed on the sample scanning confocal microscope described in chapter 3. For wide field imaging a laser beam is focused on the back aperture of the objective lens for homogeneous illumination of the field-of-view. The fluorescence emitted from the sample is collected by the same objective lens and then focused onto a CCD camera. The schematic of experimental set up is shown in Figure 2.30

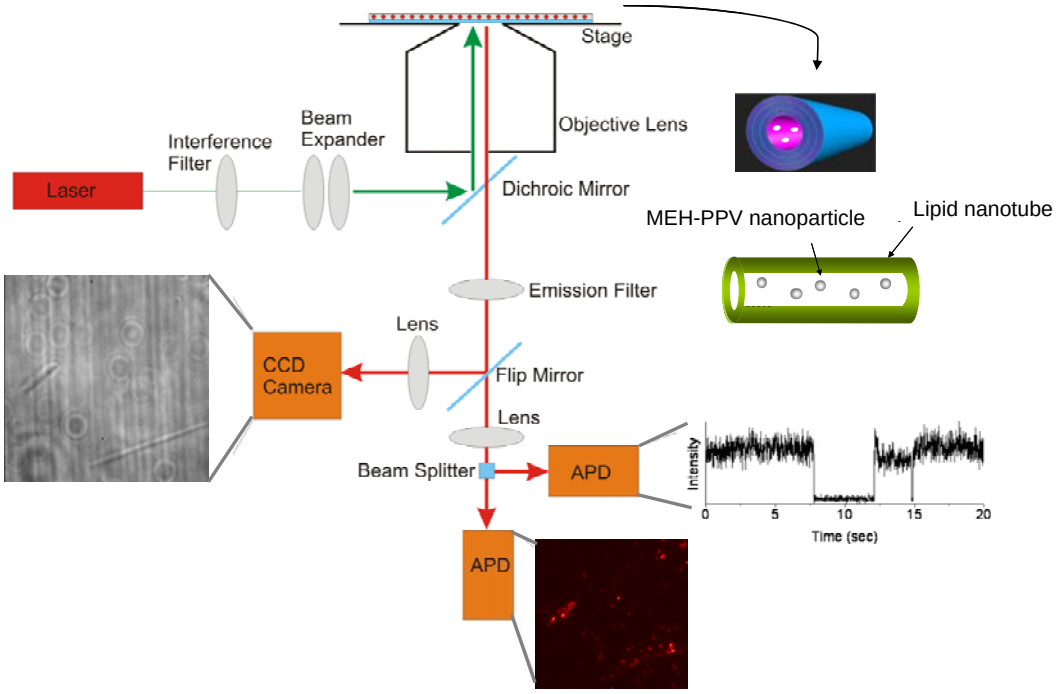

Figure 2.30 The schematic diagram of the single particle optical set up for the imaging of the nanotube samples. The bright field, confocal fluorescent (APD), and wide field images of the nanotubes and nanotubes with MEH-PPV nanoparticles are obtained.

CHAPTER 3. SINGLE PARTICLE SPECTROSCOPY ON COMPOSITE MEH-PPV/PCBM NANOPARTICLES*

3.1 Introduction

Conducting polymers have found wide-spread applications as active semiconductor materials in organic electronics. Leading examples include polymer organic light emitting diodes (PLEDs), field effect transistors (FETs) and organic photovoltaic devices (OPVs), among others.[12,16,76-81] The active layer of plastic bulk heterojunction OPVs is typically composed of a conjugated polymer (electron donating molecule) and fullerene derivative such as C_{60} or PCBM (electron accepting molecule).[14,15,82,83] This active layer has a complex nanostructured morphology that is created by mixing of the donor and the acceptor molecules into a blend that forms a bicontinuous interpenetrating network resulting in a large interfacial area for photoinduced charge separation.[84] Upon absorption of light, the optically excited donor (conjugated polymer) transfers an electron to the acceptor (fullerene) which is followed by charge separation and transport through this active layer to the corresponding electrodes, where the free carriers are collected.

Single molecule and single particle spectroscopy (SMS and SPS, respectively) present a unique opportunity to investigate the morphological and photophysical properties of such nanostructured materials at the molecular level. By simplifying complex bulk systems to single molecules and nanoparticles the complications associated with the presence of bulk material can be avoided.[56,85,86] The SMS approach has been particularly successful in developing a detailed understanding of conducting polymer photophysics.[50,86-96] Unexpected phenomena such as fluorescence intensity intermittency ("blinking") of

*This chapter has been published in Tenery, D.; Worden, J. G.; Hu, Z. J.; Gesquiere, A. J. *Journal of Luminescence* **2009**, *129*, 423-429.

single conjugated polymer chains were observed, even though these chains are multichromophoric systems.[50] In addition, the spectral properties of individual polymer chains embedded in inert polymer hosts were found to vary with preparation conditions and choice of solvent.[88,94] These results establish a direct correlation between the morphology of single conducting polymer chains and the corresponding spectral and temporal behavior, which has lead to a thorough understanding of blue (unstacked) and red (π-stacked) sites in single conducting polymer chains. These sites are coupled to each other by a fast energy transfer process, showing that even single polymer chains exhibit bulk-like behavior to a certain extent and thus are good simplified model systems to study photophysical processes in conducting polymer bulk materials. More recently, reversible photooxidation and deep charge trapping were investigated for single conducting polymer chains in a functioning device, an Stark shifts of conducting polymer spectra by electrical fields were reported.[86,97-99]

The function and structure of bulk active layers in OPVs is not well represented by single molecules, however. We therefore developed composite nanoparticles of the conducting polymer MEH-PPV and the fullerene PCBM by means of the reprecipitation method.[72] The nanoparticles represent structures in between single molecule and bulk, and enable us to study the effects of varying material morphologies and heterogeneity with respect to photophysical properties at the nanoscale. Few groups have investigated conducting polymers at the nanoparticle level, but these reports show that molecular scale information on morphology and photophysical processes is accessible.[48,74,100-102]

In this paper we describe the preparation and characterization of composite poly[2-methoxy-5-(2-ethylhexyl-oxy)-p-phenylenevinylene] (MEH-PPV, Figure 3.1 a)/1-(3-

Methoxycarbonylpropyl)-1-phenyl-[6.6]C_{61} (PCBM, Figure 3.1 b) nanoparticles with doping levels of up to 75 wt % PCBM.

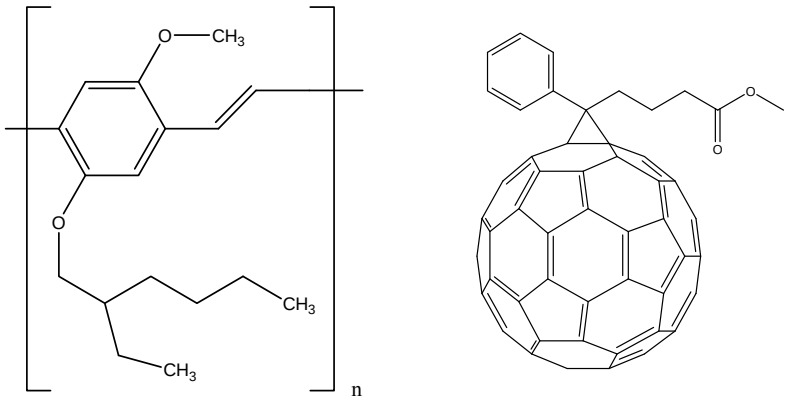

Figure 3.1 Molecular structures of (a) poly[2-methoxy-5-(2-ethylhexyl-oxy)-p-phenylenevinylene] (MEH-PPV) and (b) 1-(3-Methoxycarbonylpropyl)-1-phenyl-[6.6]C_{61} (PCBM).

These composite nanoparticles were characterized for size, morphology and photophysical properties. The data reported in the present work show that these nanoparticles represent structures in between single molecules and bulk that allow for a detailed investigation of molecular conformations and interactions as they are expected to appear in the bulk. Characterization of the nanoparticles with solution- and single particle spectroscopy reveals the extent to which variations in polymer chain folding and interactions between polymer chains and fullerenes affect material morphology and photophysical properties, providing a detailed molecular scale insight in the morphological effects that are at play in nanostructured bulk materials.

3.2 Results and discussion

Nanoparticle characterization. Size and morphology of composite MEH-PPV/PCBM nanoparticles with varying doping levels of PCBM (5, 50, and 75 wt %) and undoped MEH-PPV nanoparticles (denoted as 0 wt %) were characterized by DLS (not shown), TEM and AFM. Data for all the characterization methods and nanoparticle compositions are summarized in Table 3.1 with corresponding error bars.

Table 3.1 Summary of the nanoparticle size of composite MEH-PPV/PCBM nanoparticles with varying PCBM doping levels as determined by DLS, TEM and AFM.

PCBM doping level	0%	5%	50%	75%
DLS (nm)	31.2 ± 5.6	30.2 ± 8.2	54.8 ± 6.5	58.4 ± 5.1
TEM (nm)	28.4 ± 8.0	28.7 ± 8.5	42.8 ± 11.2	58.4 ± 18.7
AFM (Diameter) (nm)	63.1 ± 25.4	58.8 ± 20.4	89.8 ± 13.2	78.1 ± 14.4
AFM (Height) (nm)	12.1 ± 8.1	11.8 ± 3.8	29.6 ± 5.5	23.6 ± 3.3

The resulting TEM and AFM data are shown in Figure 3.2 for undoped nanoparticles and 50 wt % PCBM doped nanoparticles.

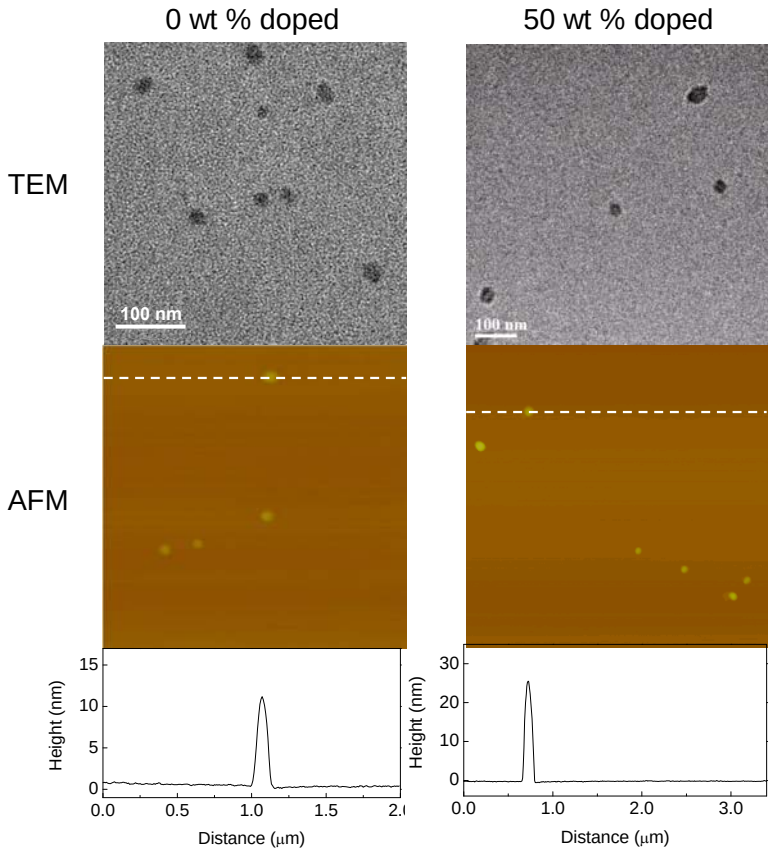

Figure 3.2 TEM and AFM images are shown for the 0 and 50 wt % PCBM doped MEH-PPV nanoparticles. The nanoparticles appear spherical in the images, and the particle radius is slightly larger for the 50 wt % PCBM doped nanoparticles. From the AFM height the nanoparticles do appear to be plate-like. However, these nanoparticles are very soft matter and as such may be compressed by tip-sample interactions. In addition, the nanoparticles are imaged after drying on a surface which may also deform the nanoparticle shape.

TEM images with reasonable contrast could be obtained even though these nanoparticles consist of soft organic materials. The electron dense nature of the organic molecules that constitute the nanoparticles is clearly advantageous in obtaining these images. The nanoparticles appear to have a quasi-spherical shape, and slightly increase in size at high PCBM doping levels due to strong aggregation interactions between PCBM molecules. TEM data provides an accurate measure of nanoparticle radius but does not provide

height information. Nanoparticle height was determined with AFM. The nanoparticle height determined from AFM measurements suggests that the nanoparticles are not perfectly spherical. Even though these experiments were completed with Tapping Mode AFM it is important to realize that these nanoparticles constitute soft matter and as such the aspect ratio may appear exaggerated. In addition, as to be expected the nanoparticle radius measured with AFM is substantially larger compared to TEM due to tip convolution.

Bulk Solution Spectroscopy. UV-Vis absorption and fluorescence spectra of the molecular solutions in THF and the nanoparticle suspensions in water were collected. These data are shown in Figure 3.3 for the undoped and 50 wt % composite MEH-PPV/PCBM nanoparticles.

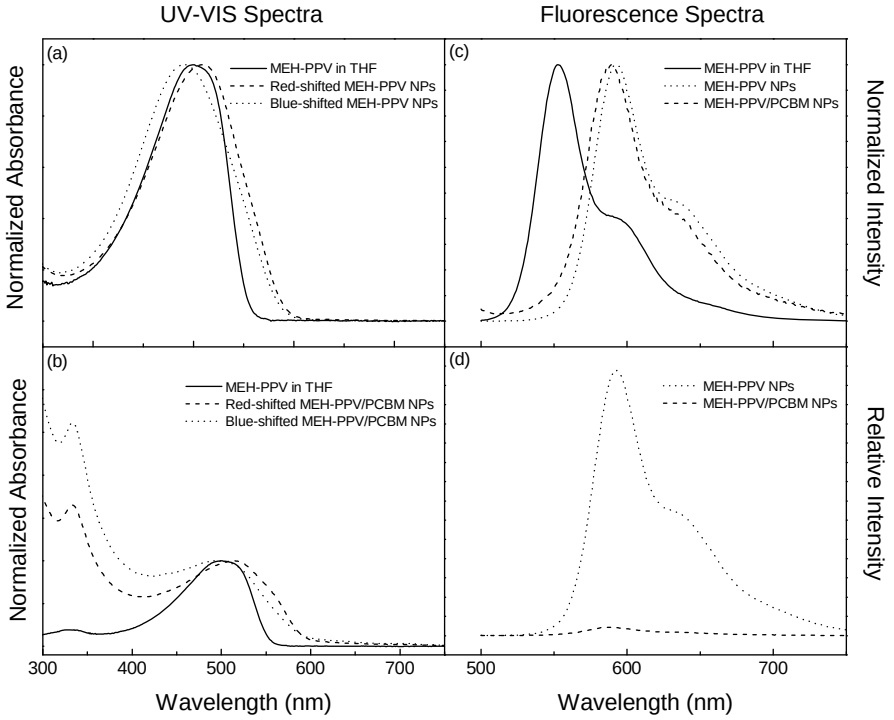

Figure 3.3 (a) UV-Vis spectra collected for undoped MEH-PPV nanoparticle suspensions in water are shown. The solid line represents the absorption spectrum of an MEH- PPV molecular solution in THF, and has its peak absorption at 500 nm. The dashed line represents the absorption spectrum of red-shifted MEH-PPV nanoparticles with peak absorption at 510 nm. The dotted line represents the absorption spectrum obtained on blue-shifted MEH-PPV nanoparticles with absorption maximum at 492 nm. (b) UV-Vis spectra collected for 50 wt % doped MEH-PPV nanoparticle suspensions in water are shown. Similar observations are made as for the undoped nanoparticles, as described in (a). The blue-shifted nanoparticles have their absorption maximum at 495 nm, the red-shifted nanoparticles have their absorption maximum at 514 nm. The increase in absorbance at 330 nm compared to the undoped nanoparticles confirms the presence of PCBM in the nanoparticles. (c) Fluorescence spectra acquired for MEH-PPV molecular solutions in THF have their peak wavelength at 551 nm (solid line). The dotted line represents the fluorescence spectrum of undoped MEH-PPV nanoparticles (0 wt % PCBM). The emission maximum is red-shifted by 42 nm compared to the molecular solution of MEH-PPV in THF (λ_{max} = 593 nm). The emission spectrum of MEH-PPV nanoparticles doped with 50 wt % PCBM is shown with the dashed line (λ_{max} = 589 nm). The spectra in this panel are normalized at the emission maxima. The actual fluorescence intensity of the 50 wt % PCBM doped nanoparticles is reduced by over 90 % compared to the undoped MEH-PPV nanoparticles. Panel (d) shows the corresponding raw data, which allows for a comparison of the relative intensities of the PCBM doped and undoped nanoparticles.

The nanoparticle UV-Vis spectra are slightly shifted compared to the corresponding molecular solutions of the materials dissolved in THF in terms of emission maxima. Interestingly, even though the nanoparticle samples of various composition where prepared under identical conditions while following identical preparation methods, for each composition of nanoparticles (0, 5, 50, and 75 wt %) the UV-Vis spectra of nanoparticles in water were found to be either slightly red or blue-shifted compared to the absorption spectra of the molecular solutions. While solutions in THF have their peak absorption at 500 nm (solid line in Figure 3.3 a, b) the nanoparticle suspensions in water showed red-shifted UV-Vis absorption spectra of the nanoparticles ranging from 502 nm to 515 nm (dashed line in Figure 3.3 a, b) as well as blue-shifted UV-Vis absorption spectra ranging from 492 nm to 498 nm (dotted line in Figure 3.3 a, b). Similar results were obtained for the 5 % and 75 % wt PCBM doped MEH-PPV nanoparticles (data not shown). This unique observation can be explained by the conformation of the polymer chains in the nanoparticles that are formed when MEH-PPV in THF solution is rapidly injected into water. The polymer chains collapse upon rapid injection in water and "freeze" into different conformations of the polymer chains for each experiment that can be classified as either defect cylinders or coiled chains with kinking and bending of the conjugated backbone. When the polymer chains collapse into coiled structures with severe kinking and bending of the conjugated backbone the effective conjugation length is reduced, leading to a blue-shift of the UV-Vis spectra.[37,45,49] When a defect cylinder is formed the stiff conjugated polymer chain only bends at a small number of locations in the polymer backbone while mostly maintaining straight segments that fold back onto each other to form a limited number of intrachain pi-stacks, while also allowing for

intermolecular pi-stacking. Under these conditions red-shifted spectroscopy is expected, and has been shown for MEH-PPV in concentrated solutions and aggregates.[37,45,48,49] Additional features in the UV-Vis spectra stem from the presence of PCBM in the composite nanoparticles. As shown in Figure 3.4 the spectral shape of the absorption spectra of the doped nanoparticles is the sum of the spectra of PCBM with its characteristic absorption peak at 330 nm and MEH-PPV, indicating that there is no detectable ground state interaction between the constituents of the composite nanoparticles.[103,104] In addition, these data show the high degree of control that is achieved in the preparation of composite MEH-PPV/PCBM nanoparticles with different PCBM doping levels.

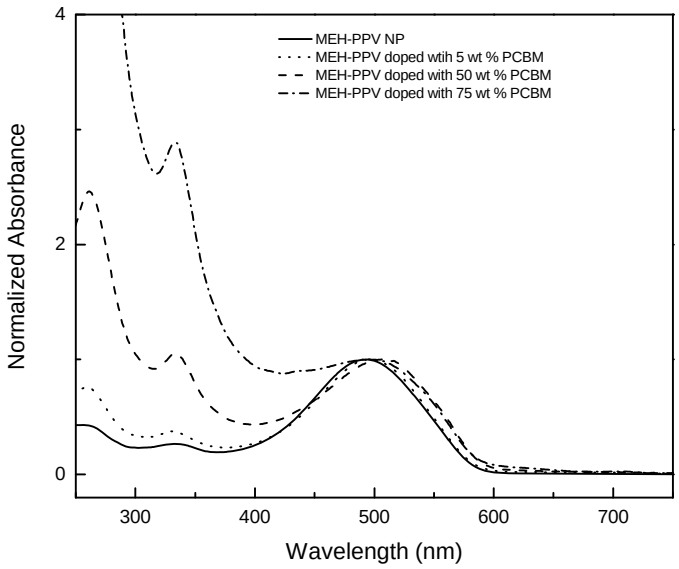

Figure 3.4 UV-Vis spectra collected for nanoparticle suspensions in water are shown for nanoparticles with 0 (solid line), 5 (dotted line), 50 (dashed line), and 75 wt % (dash-dotted line) PCBM doping. The absorption spectra confirm the presence of PCBM in the composite particles by the characteristic peak of PCBM at 330 nm. The increasing intensity of the PCBM absorbance corresponds with the higher loading of PCBM used in the nanoparticle preparation, and confirms that the resulting composite nanoparticles are indeed doped with higher PCBM levels.

Fluorescence spectra collected for the nanoparticles in water show red-shifted fluorescence emission spectra compared to the MEH-PPV molecular solution in THF, as shown in Figure 3.3 c. The emission maximum of the solution of MEH-PPV in THF is located at 551 nm (solid line). The dotted line represents the undoped MEH-PPV nanoparticles with emission maximum at 593 nm. This value is comparable to the fluorescence emission maxima reported for bulk films.[105] The dashed line represents the composite MEH-PPV nanoparticles doped with 50 wt % PCBM, with emission maximum at 589 nm. The red-shift of the fluorescence spectra for both types of nanoparticles (i.e. with blue-shifted and red-shifted absorption maxima) is explained by what was previously designated as red sites in the folded MEH-PPV chains, which are accessed by fast energy transfer from higher energy (blue) chromophores to a limited number of lower energy red sites.[106] The red-shift in emission spectra is thus due to intrachain and interchain pi-stacking interactions in the nanoparticles compared to the MEH-PPV molecular solution in THF, which is reported extensively in the literature.[37,94,98]

The fluorescence spectra of composite nanoparticles doped with 5, 50 and 75 wt % PCBM show over 90 % reduction in fluorescence intensity compared to the undoped nanoparticles. While the data in Figure 3.3 c are normalized at the emission maxima, Figure 3.3 d shows the raw data for the undoped and 50 wt % PCBM doped composite nanoparticles. The graph clearly illustrates the drop in measured fluorescence intensity detected from the PCBM doped nanoparticle sample compared to the undoped sample. Similar results were obtained for the 5 and 75 wt % PCBM doped MEH-PPV nanoparticles (data not shown). This observation is an indication of efficient electron

transfer from the conducting polymer (MEH-PPV) to PCBM. Previously, efficient electron transfer has been observed in conjugated polymers in solution[107,108] and film[103] where the fluorescence intensity was dramatically reduced as a result of addition of PCBM. In addition, energy transfer from polymer to fullerene can not be ruled out as an additional pathway for non-radiative decay of the excited state of MEH-PPV. Given that the spectral overlap between MEH-PPV emission and PCBM absorption is small, Foerster energy transfer is expected to be negligible. MEH-PPV and PCBM are in contact with each other however, so a Dexter mechanism for energy transfer could take place. However, reports in literature documenting various Electron Spin Resonance (ESR) studies show that signal from electrons present in charge separated states can be detected.[103,109] As such, although energy transfer between conducting polymer and fullerene is a possible competing mechanism, charge transfer has been proven experimentally to be the dominant process.

Single particle fluorescence imaging and spectroscopy. The fluorescence properties of the nanoparticles were investigated in further detail on a per-nanoparticle basis. The nanoparticles were deposited on cover glasses by spincoating from a 4 wt % PVA solution and sealed from oxygen and water present in ambient atmosphere with a 200 nm Al film deposited through thermal evaporation. These samples were subsequently imaged on a sample scanning single molecule/nanoparticle detection confocal fluorescence microscope. Typical 10 μm fluorescence images of MEH-PPV nanoparticle samples are shown in Figure 3.5.

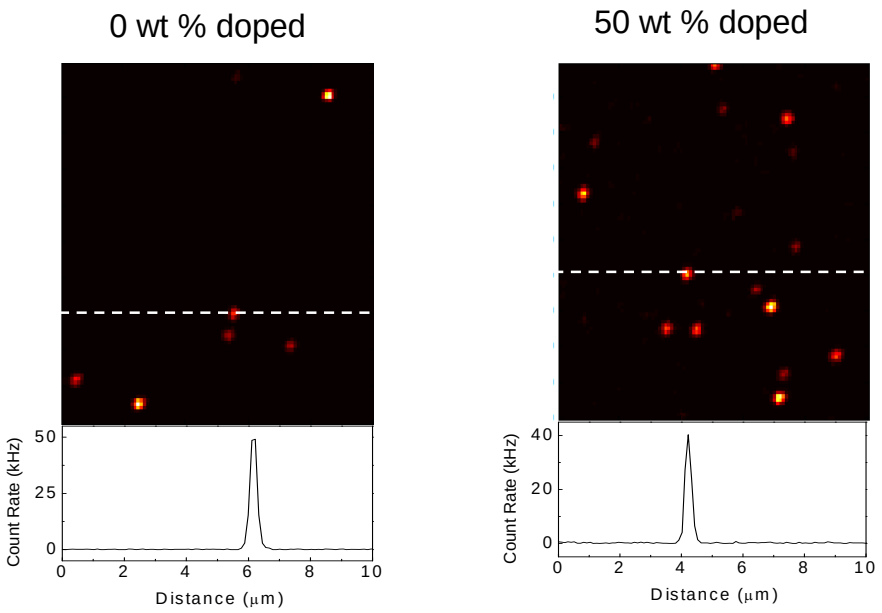

Figure 3.5 (Left) Fluorescence image of single undoped MEH-PPV nanoparticles. The image size is 10 x 10 μm^2. Only 0.72 W/cm^2 of the 488 nm line of an argon ion laser was needed to image the sample because of the large number of chromophores per nanoparticle. (Right) Fluorescence image of a sample consisting of composite MEH-PPV nanoparticles doped with 50 wt % PCBM. The image size is 10 x 10 μm^2. The sample was imaged with 7.2 W/cm^2 of the 488 nm line of an argon ion laser as excitation light. The linescans show that the factor of 10 difference in laser excitation intensity results in similar detected photon count rates for the PCBM doped and undoped MEH-PPV nanoparticles, indicating effective quenching of the MEH-PPV fluorescence by the PCBM present in the doped nanoparticles.

The MEH-PPV nanoparticles appear as bright diffraction limited spots in the images. Very low laser power was used due to the large number of emitters per nanoparticle. Due to quenching of the MEH-PPV emission by PCBM in the composite nanoparticles the detected fluorescence intensity of the doped nanoparticles is lower than that of the undoped polymer nanoparticles. PCBM doped MEH-PPV nanoparticle samples (represented by the 50 wt % PCBM doped nanoparticle samples in Figure 3.5) typically require a ten-fold increase in laser excitation intensity to achieve comparable emission

count rates as the undoped MEH-PPV nanoparticles. The laser power requirements do not scale with the PCBM doping levels, and indicate that even at lower doping levels (i.e. 5 wt %) quenching of the MEH-PPV fluorescence by PCBM is already an efficient process. The origin of this high efficiency not only lies in the facile charge transfer from conducting polymer to fullerene itself. It has been shown by single molecule spectroscopy experiments that radical cationic species on conjugated polymer backbones are very efficient quenchers via an energy transfer mechanism from the excited chromophore to the hole on the conducting polymer backbone. The hole has a quenching radius in excess of 10 nm, which is on the same length scale as the nanoparticle dimensions. Similar observations have also been made in bulk films and aggregates.[51,110]

The spectral properties of the composite MEH-PPV/PCBM nanoparticles and undoped MEH-PPV nanoparticles were investigated with single particle spectroscopy, the results of which are shown in Figure 3.6.

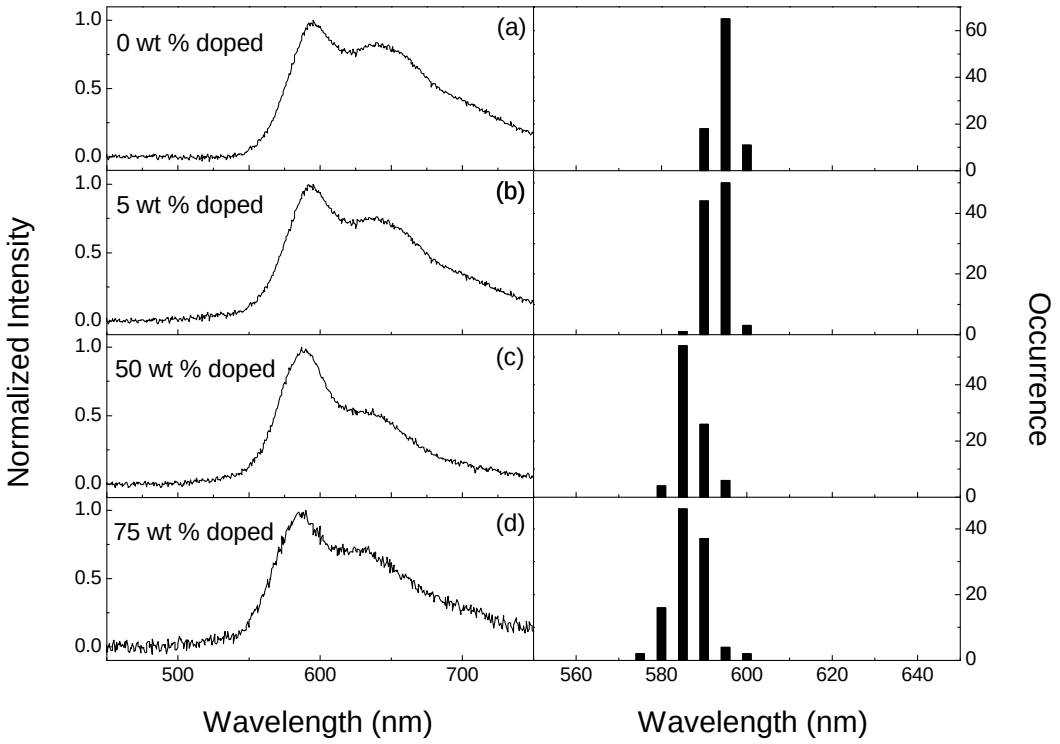

Figure 3.6 Representative ensemble spectra constructed from single nanoparticle spectra. Corresponding histograms for the emission maxima are shown in the right hand side panels. Emission maxima were determined by the best-fits of individual spectra to two or three Gaussians. (a) Single nanoparticle ensemble spectrum of undoped MEH-PPV nanoparticles. The emission maximum is located at 594 nm, in close agreement with bulk solution fluorescence spectroscopy. (b) Single nanoparticle ensemble spectrum of composite MEH-PPV nanoparticles doped with 5 wt % PCBM. The emission maximum is located at 593 nm, and as such not significantly shifted compared to the undoped nanoparticles. (c) Single nanoparticle ensemble spectrum of composite MEH-PPV nanoparticles doped with 50 wt % PCBM. The emission maximum is located at 588 nm, and is blue-shifted by 6 nm compared to the undoped nanoparticles. (d) Single nanoparticle ensemble spectrum of composite MEH-PPV nanoparticles doped with 75 wt % PCBM. The emission maximum is located at 587 nm, and is blue-shifted by 7 nm compared to the undoped nanoparticles. In addition, clear changes in vibronic structure are evident with varying PCBM doping levels. These observations indicate that at higher PCBM loading a reduced conjugation length exists due to steric effects caused by the presence of PCBM, and that PCBM reduces the intermolecular pi-stacking interactions. As a result, exciton transport may be limited due to compartmentalization of the polymer chain segments, basically preventing the exciton from reaching low energy sites.

Fluorescence spectra were collected for individual nanoparticles, and collected into an ensemble. Emission maxima of the individual particle spectra were determined by fitting the spectra with two or three Gaussians. The resulting data were used to construct histograms of single particle emission peak wavelengths for each of the four nanoparticle types. Two key observations can be made from these data: (i) the single particle ensemble spectra shift with respect to each other depending on PCBM doping level and (ii) the vibronic structure of the spectra changes with PCBM doping level. These observations are discussed hereafter. The spectra of the undoped nanoparticles (Figure 3.6 a) are red-shifted to 594 nm compared to the molecular solution in THF and this emission maximum corresponds well with the fluorescence spectra of undoped nanoparticles acquired in bulk measurements. Interestingly, the spectra of doped nanoparticles (especially 50 and 75 wt % PCBM doping) show a broader distribution of maximum wavelengths ranging from ~580 nm to ~590 nm, which was not observed in bulk measurements. In addition, the single particle ensemble spectra for the 5 wt % PCBM doped nanoparticles are blue-shifted by only 1 nm compared to the undoped nanoparticles, while those of the 50 and 75 wt % PCBM doped nanoparticles are blue-shifted by 6 nm and 7 nm compared to the undoped nanoparticles, respectively.[103] This observation indicates that at higher PCBM loading a reduced conjugation length exists due to steric effects caused by the presence of PCBM that result in polymer chain conformations with increased kinking and bending of the backbone. In addition, the presence of PCBM will reduce intermolecular pi-stacking interactions. As a result, the exciton transport may be limited due to compartmentalization of the polymer chain segments, basically preventing the exciton from reaching low energy sites. The changes

in vibronic structure detected in the single particle ensembles further corroborate the changing aggregation state of the conducting polymer chains. In particular, interchain interactions diminish with increasing doping levels which leads to a decreasing intensity of the 0-1 vibronic peak relative to the 0-0 transition. Once doping levels reach 75 wt % however, the single particle ensemble spectra strongly resemble those of the 5 wt % PCBM doped MEH-PPV nanoparticles, which is attributed to phase separation of MEH-PPV and PCBM in the composite nanoparticles.[41]

These SPS data provide a molecular scale insight into the evolution of conducting polymer morphologies in blended materials with varying degrees of PCBM doping by using nanoparticles as model systems that are situated in between single molecules and bulk material. While spectral differences between the composite and undoped nanoparticles remained undetected in the ensemble solution measurements they were revealed by SPS. This observation demonstrates that we can avoid the enormously broad distribution of material morphologies and tremendous heterogeneity present in the bulk by investigating simplified systems that are representative of the bulk material.

3.3 Conclusion

In this chapter the preparation and characterization of composite MEH-PPV/PCBM nanoparticles with doping levels of up to 75 wt % PCBM was reported. These novel nanoparticles represent structures in between single molecules and bulk that allow for a detailed investigation of the role of nanostructure on the properties of bulk materials. The composite nanoparticles were characterized for size, morphology and bulk as well as single nanoparticle photophysical properties. With SPS we were able to gain a molecular scale understanding of changes in MEH-PPV conformation upon addition of the fullerene

PCBM that is not accessible through bulk measurements. Such findings may be useful for further development of efficient conducting polymer/fullerene bulk heterojunction organic photovoltaic devices.

CHAPTER 4. EFFECT OF PCBM CONCENTRATION ON PHOTOLUMINESCENCE PROPERTIES OF COMPOSITE MEH-PPV/PCBM NANOPARTICLES INVESTIGATED BY A FRANCK-CONDON ANALYSIS OF SINGLE PARTICLE EMISSION SPECTRA*

4.1 Introduction

Conjugated polymers have been of great interest due to their potential for application in optoelectronic devices such as Organic Photovoltaic cells (OPVs), Polymer Light-Emitting Diodes (PLEDs) and Organic Field-Effect Transistors (OFETs).[1,78,111-114] However, the photophysical and optoelectronic properties of conjugated polymer materials have been found to be very complex due to the formation of interchain excitations and exciton migration processes. Exciton migration has lead to unexpected observations for conjugated polymer materials such as changes in spectral properties during the lifetime of the excited state due to hopping of the exciton over a distribution of sites with increasing conjugation length.[115] Aggregation of conjugated polymer chains also leads to short range order, which induces the formation of shared excitations between polymer chains that have a low quantum yield. These sites act as an energy sink and work as a trap for surrounding highly emissive molecular (excitonic) excitations,[105] effectively reducing the luminescence of the solid state material.[116-118] Aggregation can also influence the shape of the emission spectrum by altering the peak intensities of vibronic replicas.[115,119,120] These material properties have been found to vary between different sample preparations adding further complexity to achieving a complete understanding of these materials, and have been related to the enormous conformational

*This chapter has been accepted for publication in Tenery, D.; Gesquiere, A. J. *ChemPhysChem* **2009**

disorder that exists for conjugated polymers.[121-123] This issue has been highlighted by recent work in the organic electronics field, where it was found that the overall function and properties of conjugated polymer devices are highly dependent on the processing of the conjugated polymer material due to the sensitivity of the morphology of conjugated polymer materials to processing parameters such as choice of solvent, polymer concentration, spin coating speed, and solvent- or thermal annealing of the film.[37,46,124-130] Consequently, a lot of attention has been devoted to the investigation of the photophysical and optoelectronic properties of conjugated polymer materials with respect to bulk material morphology.[37,131-139] In recent years, it has been shown with Single Molecule Spectroscopy (SMS) that even single conjugated polymer chains present a rich photophysical picture reminiscent of the bulk material, although simplified, that is related to different morphologies that can be adopted by single polymer chains in the solid state with correlated spectroscopic properties.[50,86,88,92,106,140] These studies have produced exceptional data that has lead to a better understanding of the relationship between single conjugated polymer chain conformation and photophysical and optoelectronic properties of the chain. Single step photobleaching, fluorescence blinking (fluorescence intermittency), and variations in fluorescence spectral properties with preparation conditions were discovered. These observations were found to be related to a fast intramolecular energy transfer processes from higher energy chromophores in extended chain segments to low energy chromophores that are formed by intrachain pi-stacking, i.e. energy funneling.[52,94,141]

More recently, conjugated polymer nanoparticles have been fabricated and studied for their spectroscopic properties.[48,49,74,110,142-144] These studies are motivated by the fact that

single molecules do not necessarily represent the properties and function of the bulk material, specifically when considering interchain interactions. While due to the aforementioned conformational disorder that exists for conjugated polymers the bulk material is exceedingly complex to study in terms of molecular scale interactions and properties, these nanoparticles allow researchers to study interchain conjugated polymer interactions at the molecular level on a length scale in between single molecules and bulk since only a limited number of polymer molecules are present in the nanoparticles (Figure 4.1).

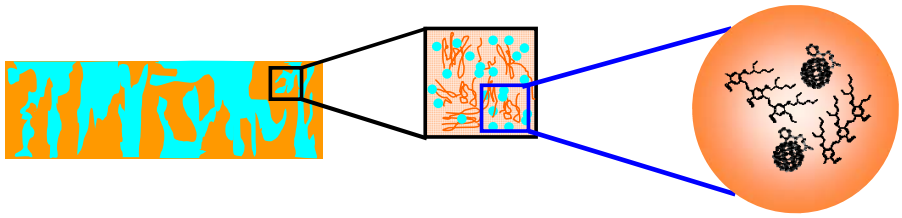

Figure 4.1 Sketch illustrating the use of composite nanoparticles in reducing the complexity of studying composite materials in bulk films by reducing the number of molecules, interfaces and domains that is being considered. Blue color represent PCBM, orange color represents MEH-PPV.

We recently reported the fabrication of composite nanoparticles of the conjugated polymer poly[2-methoxy-5-(2-ethylhexyl-oxy)-p-phenylenevinylene] (MEH-PPV) and the fullerene 1-(3-Methoxycarbonylpropyl)-1-phenyl-[6.6]C_{61} (PCBM),[75] a material system that is commonly used as an active layer in Bulk Heterojunction Organic Photovoltaic Devices (BH-OPV).[14,81,145-149] Molecular structures and resulting nanoparticle suspensions are shown in Figure 4.2.

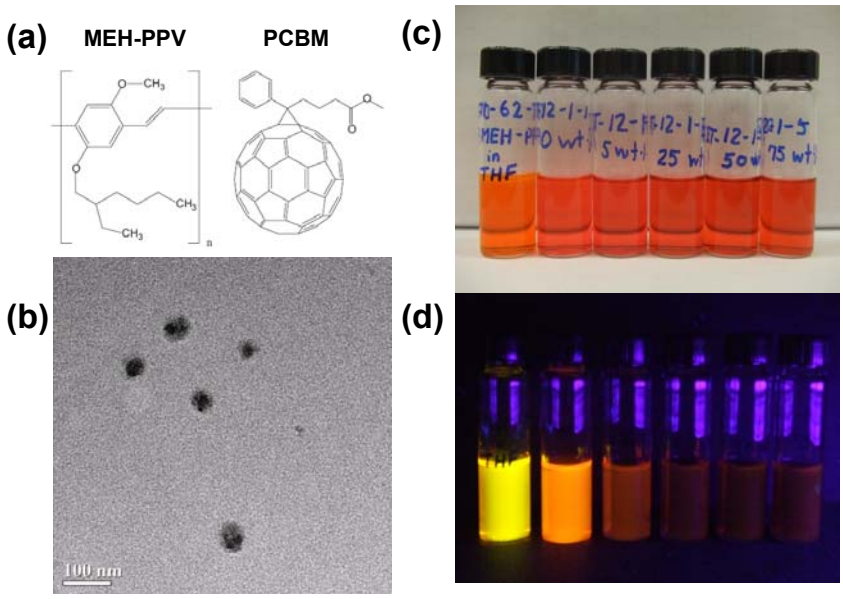

Figure 4.2 (a) Molecular structures of poly[2-methoxy-5-(2-ethylhexyl-oxy)-p-phenylenevinylene] (MEH-PPV) and the fullerene 1-(3-Methoxycarbonylpropyl)-1-phenyl-[6.6]C_{61} (PCBM). (b) TEM images of 75 wt % PCBM doped MEH-PPV/PCBM nanoparticles. (c) From left to right: Molecular solution of MEH-PPV in THF, and composite MEH-PPV/PCBM nanoparticle suspensions (0, 5, 25, 50, 75 wt % PCBM, respectively) in water. (d) Samples as described in (c) under UV illumination. Aggregation quenching is evident when comparing the molecular solution of MEH-PPV in THF with the undoped (0 wt %) MEH-PPV nanoparticles. In addition, fluorescence quenching due to charge transfer from MEH-PPV to PCBM is clearly observed.

Using Single Particle Spectroscopy (SPS), where the optical properties of individual nanoparticles are studied, we were able to show how variations in polymer chain folding and interactions between polymer chains and fullerenes affect material morphology and photophysical properties at the molecular scale in nanostructured bulk materials. In particular, the vibronic structure of the single particle ensemble spectra (constructed by averaging the emission spectra of a large number of individual nanoparticle spectra) was found to change with PCBM doping level, indicative of changes in conducting polymer conjugation length, interchain interactions, and the extent of exciton transport.

In this paper, we extend our study of this composite nanoparticle system to further investigate the spectral properties as a function of PCBM doping level by means of a detailed Franck-Condon analysis. Different research groups have reported on the study of the vibronic structure of fluorescence spectra of bulk conjugated polymer films.[47,115,119,120,150-152] Two emitter Franck-Condon models, where the emission spectrum is modeled as the superposition of two Franck-Condon vibronic progressions, have been found to be suitable for interpretation of the vibronic progression of fluorescence spectra of pure (undoped) MEH-PPV films. In this case one emitter has aggregate (intermolecular) properties and the other emitter has isolated molecule (intramolecular) properties.[47,150,152] However, this issue was investigated only on a few occasions for conjugated polymer blended materials. Xu et al. showed that the relative intensity of 0-1 vibronic peak compared to the 0-0 vibronic peak is suppressed in MEH-PPV films upon addition of PBD at low temperature.[153] These observations were attributed to changes in exciton migration with film composition. Marletta et al. studied blended films of MEH-PPV in polystyrene (PS) at low temperature.[154] The investigators were able to assign aggregate states and intrachain transitions in the emission spectra of MEH-PPV/PS blends. A similar observation was made by Bjorklund et al. for poly(p-phenylenevinylene) (PPV) blended into polyvinyl alcohol (PVA).[155] Ho et al. performed steady state photoluminescence spectroscopy on blended PPV-silica particle films and observed a clear effect of doping on the vibronic structure of the PPV emission spectra, for which an apparent increase in the intensity of the 0-0 transition was found with increasing silica doping levels, which could again be explained by the two emitter Franck-Condon model.[156]

These bulk studies do not reveal information on the distribution of properties of the excitonic (molecular) and aggregate sites in the materials, however. In this paper, we report a Franck-Condon analysis on emission spectra of single composite MEH-PPV/PCBM nanoparticles with various PCBM doping levels. Consistent with bulk spectroscopy on blended conjugated polymer/dopant films, we find that single particle emission spectra are in fact the result of the superposition of emission spectra of two emitters in the conjugated polymer particles. A distinct distribution of properties in samples of a given composition as well as between samples of different composition is observed in terms of Huang-Rhys factors and aggregation behavior. In addition, a unique observation is that the aggregate emitters show large Huang-Rhys factors for which the average has a broad distribution of values, indicative of a heterogeneous distribution of aggregate morphologies in blended conducting polymer materials The latter observation is in contrast to previously reported bulk studies from which it was assumed that inhomogeneities in material properties are overwhelmed by the uniformity of the properties of the aggregate sites.[150]

4.2 Results

4.2.1 Franck-Condon analysis of single particle spectra

The optical properties of composite MEH-PPV/PCBM nanoparticles with 0, 5, 25, 50, and 75 wt % of PCBM were studied by Single Particle Spectroscopy. Fluorescence spectra were collected for over 300 nanoparticles for each nanoparticle composition. For each dataset the single particle spectra were averaged into a single particle ensemble spectrum i.e. fluorescence spectra were taken for individual nanoparticles and averaged for over 300 of these individual nanoparticles for a given composition. These single

particle ensemble spectra are shown in Figure 4.3, where the normalized spectra are overlaid on each other.

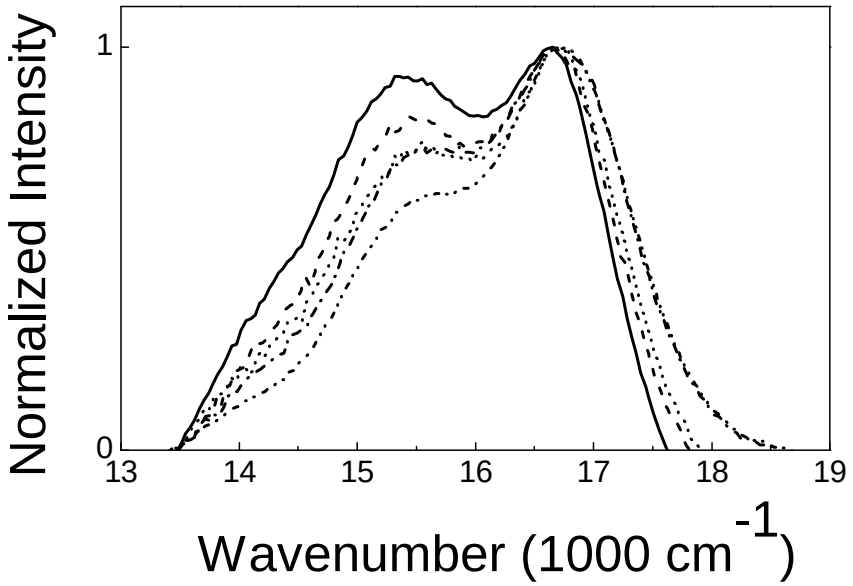

Figure 4.3 Overlaid normalized single particle ensemble spectra of 0 wt % (solid line), 5 wt % (dashed line), 25 wt % (dash dotted line), 50 wt % (dash dot dotted line), and 75 wt % (dotted line) PCBM doped composite nanoparticles reveal distinct changes in vibronic structure of the photoluminescence spectra as a function of nanoparticle composition.

Upon addition of PCBM the single particle ensemble spectra blue-shift due to interruption of intermolecular interactions of the MEH-PPV chains by PCBM. The peak emission histograms shown in Figure 4.4 show a shift in the distribution to higher wavenumber with PCBM doping levels up to 50 wt % and thus confirm this trend.

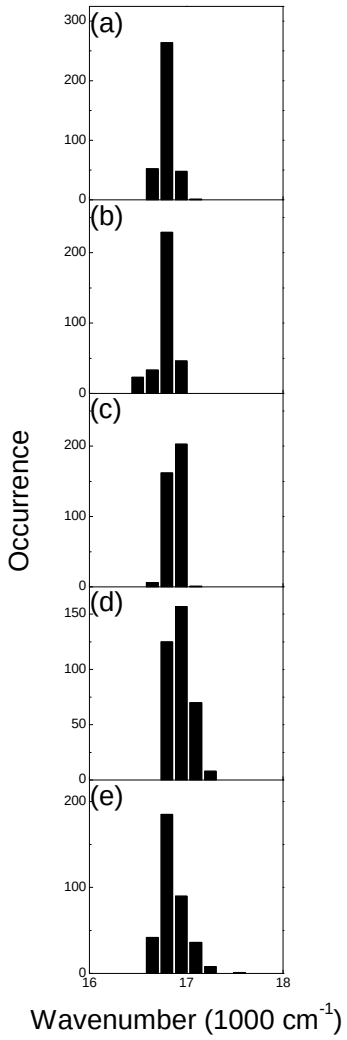

Figure 4.4 (a-e) Histograms depicting the distribution of peak emission maxima in the ensembles of single particle spectra collected for the composite 0, 5, 25, 50, 75 wt % PCBM doped MEH-PPV nanoparticle samples, respectively.

At 75 wt % the distribution shifts back to lower energy however. In addition, the data in Figure 4.3 clearly show a distinct change in spectral shape with changing PCBM doping levels. The single particle ensemble spectra show a change in relative intensities of the higher and lower energy emission peaks (approximately 16,750 and 15,500 cm^{-1}, respectively) with increasing doping level of PCBM. A key observation is that the lower

energy peak appears to be suppressed with increasing PCBM doping levels up to 50 wt % PCBM and then increases at 75 wt %.

In order to investigate these observations in detail the emission spectra of individual nanoparticles were fitted to a Frank Condon model one-at-a-time. Figure 4.5 shows representative single particle spectra of MEH-PPV nanoparticles with different doping levels of PCBM.

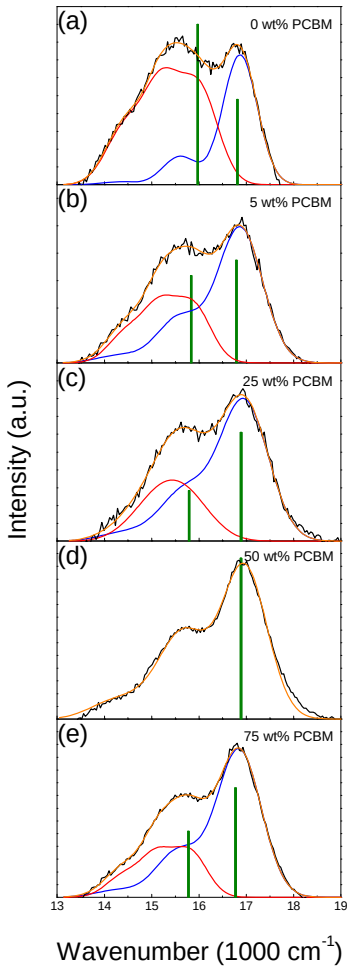

Figure 4.5 (a-e) Photoluminescence spectra (black line) and fitted data obtained through Franck-Condon analysis, including fitted emission spectrum (orange), molecular emitter spectrum (blue), aggregate emitter spectrum (red), and stick spectra (green) shown for a single nanoparticle of each of the compositions that were investigated as indicated on each panel.

The black solid line and the orange solid line correspond to the experimental and the calculated single particle spectra using a Franck Condon analysis, respectively. In the Franck Condon model the intensity of vibronic peaks is described by the Franck-Condon factor, in which the Franck-Condon factor for a given vibronic transition can be expressed by:

$$I_{0-n} = \frac{e^{-S} S^{n}}{n!} \tag{4.1}$$

where $I_{0\text{-}n}$ is the intensity of the vibronic peak for emission from the 0 vibronic level in the excited state to the n^{th} vibronic level in the ground state (vibronic mode 0-n), n is the number of the ground state vibronic level and *S* is the Huang-Rhys factor.[157] The Huang-Rhys factor *S* is a dimensionless quantity that describes the electron-phonon coupling between the ground state and excited state and is given by:

$$S = \frac{M\omega}{2\hbar}(\Delta Q)^{2} \tag{4.2}$$

where M is reduced mass and ω is the angular frequency of the harmonic oscillator that is the transition couples with, and ΔQ is the displacement of the minima of the potential energy surfaces in the electronic ground and excited states along the nuclear coordinate.[158] As it can be seen in Equation 4.2, *S* depends largely on the square of the displacement of the minima of the potential energy surface of the ground and excited states (ΔQ). In the case that there is no displacement between the potential energy surface of the ground state and excited state, ΔQ is equal to zero and therefore *S* is also equal to zero, resulting in a spectrum where all the intensity is located in the 0-0 transition. In many cases, *S* can be empirically determined from the ratio of intensity of 0-1 transition relative to 0-0 transition intensity[159]:

$$S = \frac{I_{0-1}}{I_{0-0}} \qquad 4.3$$

Using Equation 4.3, *S* for emission spectra of individual MEH-PPV nanoparticles doped with 0, 5, 25, 50, and 75 wt % PCBM (Figure 4.5) can be approximated as 0.8, 0.8, 0.7, 0.5 and 0.7, respectively, which will be referred to as $S_{apparent}$ from now on.

In previous studies, *S* has been correlated with the conformational disorder of polymer chains and exciton migration in bulk materials, where smaller *S* indicates longer conjugation length for the conducting polymers and larger extent of exciton migration.[52,115,153,159,160] In our data $S_{apparent}$ decreases upon increasing the doping level of PCBM up to 50 wt %, which suggests that the effective conjugation length and exciton migration in the PCBM doped MEH-PPV nanoparticles are enhanced. This interpretation contradicts the observed blue shifts of the emission maxima with increasing PCBM doping levels. Literature reports support the notion that a blue shift of emission spectra is expected for MEH-PPV blends and a reduction in exciton migration was observed with increasing amounts of dopants.[115,153,155,156] This conclusion is further corroborated by fitting the Franck-Condon model to the emission spectra of single composite nanoparticles, using the following equation in a nonlinear least squares fitting procedure:

$$I_{em} = \mathrm{A}\omega^3 \sum_{n_i=0} \left(\prod_i \frac{e^{-S_i} S_i^{n_i}}{n_i!} \right) e^{-\left(\frac{\omega - E_0 + n_i \hbar\omega_i}{\sigma}\right)^2} \qquad 4.4$$

where ω is the frequency of the emitted light, A is the amplitude of the 0-0 transition, and S_i, n_i, and $\hbar\omega_i$ are the Huang-Rhys factor, vibrational quanta, and vibrational frequency for *i*th mode, respectively.[161] The first part of Equation 4.4 gives the amplitude and Franck Condon factors of the vibronic mode under consideration, and results in a line spectrum given the Poisson distribution that is used to describe the system. These lines

are then broadened using a Gaussian function with width σ for each vibronic mode. The resulting fits (not shown) do not correspond well with the data, as is evident even by simple visual inspection. A similar discovery was made for emission spectra taken for composite PPV films doped with silica particles, where the data did not fit the Franck Condon model as well, a finding that was attributed to the presence of two emitters in PPV films for which the relative contribution of the lower energy emitter increased with decreasing silica volume fraction.[156] Given these data the single particle spectra of MEH-PPV nanoparticles doped with 0, 5, 25, 75 wt % PCBM were fitted with a two-emitter model (Equation 4.5), and as a result good fits to the data are obtained (Figure 4.5 a, b, c, and e).

$$I_{total} = I_{(red\ type)} + I_{(blue\ type)} \qquad 4.5$$

In Equation 4.5 we classify the higher energy emitters as "blue" type (molecular) and the lower energy emitters as "red" type (aggregate) emitters, and $I_{(red\ type)}$ and $I_{(blue\ type)}$ are each described by Equation 4.4. Therefore, for each single particle spectrum fitted with the model shown in Equation 4.5 we obtain the red type and blue type emitter fits. The sum of red type and blue type emitters makes up the calculated single particle spectrum.

Interestingly, for the single particle spectra of MEH-PPV nanoparticles doped with 50 wt % the one emitter model (Equation 4.4) produces an excellent fit that corresponds to a spectrum to which only the blue type i.e. molecular emitter contributes (Figure 4.5 b), indicating that the emission spectrum only consists of the excitonic (molecular) emitter. At this doping level the presence of PCBM has effectively led to the suppression of aggregation interactions between the polymer chains, making the spectrum appear as a dilute molecular solution, albeit red shifted with respect to the molecular solution.

4.2.2 Single particle ensembles

Figure 4.6 a-e shows the experimental and fitted single particle ensemble spectra (overall fit to experimental data, and calculated blue and red emitter spectra) of MEH-PPV nanoparticles doped with 0, 5, 25, 50 and 75 wt % PCBM.

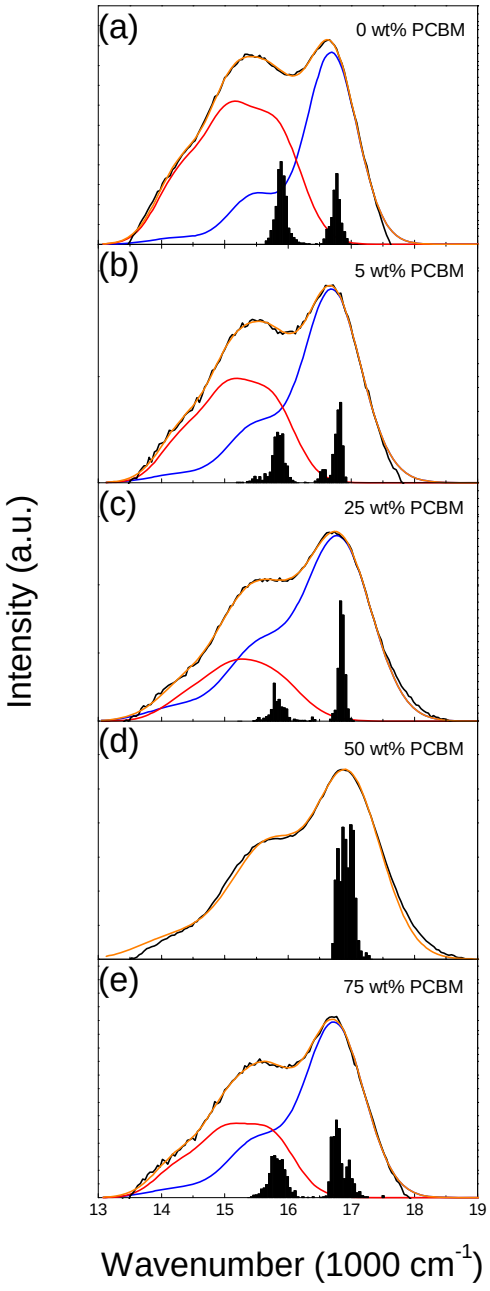

Figure 4.6 Single particle ensemble spectra (black lines) and corresponding fitted ensembles (fitted emission spectrum (orange), molecular emitter spectrum (blue), aggregate emitter spectrum (red), and stick spectra (green)) obtained through Franck-Condon analysis constructed by averaging the data collected and fitted for over 300 nanoparticles for each of the compositions indicated in panels (a-e).

Each type of single particle ensemble spectra (experimental or fitted) in this figure is constructed by averaging at least 300 individual single particle spectra. The black solid lines represent the single particle ensemble spectra constructed from experimentally determined emission spectra of individual MEH-PPV nanoparticles. The orange solid line represent the fitted single particle ensemble spectra (i.e. fit over 300 individual nanoparticle spectra and average) determined using the two-emitter Frank-Condon model (Equation 4.5), except for 50 wt % PCBM doped MEH-PPV nanoparticles for which Equation 4.4 (single emitter model) was fitted to the data. The single particle ensemble spectra of red and blue type emitters are shown as red and blue lines, the sum of which results in the overall fit to the data (orange line). The green bars (stick spectra, i.e. before Gaussian broadening) depict the distribution of 0-0 vibronic origins for individual blue and red emitters with corresponding averaged intensities for the ensemble of emitters. Since we fitted an ensemble of individual nanoparticles one-at-a-time we also obtain the distribution of the Huang-Rhys factors for the blue and red type emitters (S_{blue} and S_{red}, respectively), shown in Figure 4.7.

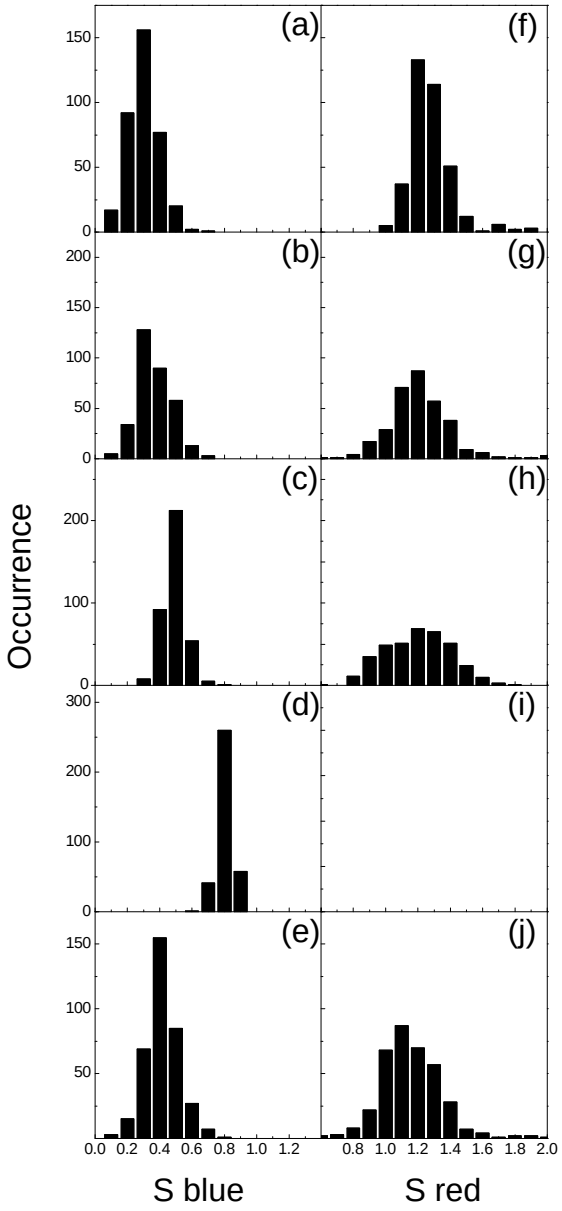

Figure 4.7 (a-e) Distribution of Huang-Rhys factors obtained for the molecular type emitter present in composite 0, 5, 25, 50, 75 wt % PCBM doped MEH-PPV nanoparticles, respectively. (f-j) Distribution of Huang-Rhys factors obtained for the aggregate type emitter present in composite 0, 5, 25, 50, 75 wt % PCBM doped MEH-PPV nanoparticles, respectively. Since the aggregate emitter is not detected for 50 wt % PCBM doped MEH-PPV nanoparticles no data is reported in panel (i).

Note that in the case of 50 wt % PCBM doped MEH-PPV nanoparticles (Figure 4.7 d, i), only S_{blue} is determined since it is fitted with only blue emitters. The data shown in Figure 4.6 present a number of key observations: (i) the intensity of red emitters relative to blue emitters in the fitted spectra (and stick spectra) decreases with increasing PCBM doping levels (also see Figure 4.5), until (ii) the red emitters vanish at 50 wt % PCBM doping and spectra can be fitted with a single emitter, however, (iii) at 75 wt % PCBM doping the red emitter re-appears, and the spectra appear similar to the 25 wt % PCBM case. In addition, (iv) S_{blue} increases with increasing PCBM doping levels up to 50 wt % PCBM doping, followed by a decrease at 75 wt % PCBM doping levels, while (v) S_{red} is large for all particle compositions and shows a minor change in the average value with particle composition towards lower values, however, S_{red} shows a much broader distribution than S_{blue}. These findings are discussed hereafter.

4.3 Discussion

The morphology of MEH-PPV nanoparticles obviously strongly depends on PCBM doping levels given that intra- and interchain interactions of the polymer chains will be distorted by the presence of PCBM. The critical aspect of investigating this issue through a composite nanoparticle system is that a distribution of morphological properties can be detected, which is difficult to achieve in bulk films due to ensemble averaging of properties. The addition of PCBM leads to what has been previously described as a dilution effect, where dopants interrupt intermolecular stacking and aggregation of conjugated polymer chains.[162] This observation can be clearly made for the data reported here (summarized in Table 4.1). The data reported earlier will be discussed in more detail hereafter.

4.3.1 Single Particle Spectra

In Figure 4.5 a,b,c,e the MEH-PPV nanoparticles are fitted with two emitters (red and blue), each providing their unique spectra. It can be seen that the calculated single particle spectrum using two types of emitters fits well with the experimental single particle spectrum of MEH-PPV nanoparticles. The ratio of the amplitude (stick spectra) from red emitter to blue emitter is substantially larger than 1 for 0 wt % PCBM nanoparticles which signifies that the emission is mainly coming from the red type emitters, but there is a significant fraction of blue type emitters that can be detected as well. Here it is important to realize that a majority of emission from red type emitters in the spectra does not necessarily signify that there is a majority of these low energy emitters. The low energy emitters can be populated by energy transfer from the high to low energy emitters, i.e. exciton migration.[163-168] The fact that we can detect a significant number of blue emitters most likely indicates that a fraction of the blue emitters did not energy transfer to lower energy aggregate sites, meaning that a red aggregate site was not found during the exciton migration process. When MEH-PPV nanoparticles are doped with 5 wt % PCBM (Figure 4.5 b), the nanoparticle luminescence is strongly quenched and a distinct decrease in the ratio of the amplitude between the red and the blue types of emitters is observed. When MEH-PPV nanoparticles are doped with 25 wt % PCBM, a noticeable change in the ratio of the amplitude between the red and the blue types of emitters is again observed. The ratio of the amplitude from red to blue types of emitters is now significantly less than 1. These data shows that the presence of 25 wt % PCBM in the MEH-PPV nanoparticles has a considerable effect on the morphology of the polymer chains, and interferes with interchain interaction in the MEH-PPV nanoparticles to a

higher degree compared to MEH-PPV nanoparticles doped with 5 wt % PCBM. The majority of the emission spectrum can now be attributed to blue type emitters, indicating reduced aggregation and thus less lower energy sites are available to participate in energy transfer events from blue sites to red sites. In addition, with increasing disorder exciton migration will be reduced which may also contribute to red sites being less likely to be found during exciton migration.

When MEH-PPV nanoparticles are doped 50 wt % PCBM, the experimental single particle spectrum can be fitted with only blue type emitters (Figure 4.5 d). In the presence of 50 wt % PCBM, interchain interactions are severely interrupted, and the emission spectrum consists solely of molecular (excitonic) emission. This indicates that energy transfer from blue type emitters to the red type emitters is strongly hindered due to either the complete absence of intermolecular aggregate sites, or these sites occur too rarely to be found during exciton migration. In addition, even though PCBM interrupts intermolecular aggregation and the single particle spectra are blue shifted with respect to 0 wt % PCBM nanoparticles the peak emission is still strongly red shifted compared to solution (~560 nm). This indicates that even isolated conjugated polymer chains are in a collapsed conformation and basically self-aggregate when poorly solvated, an observation that was reported recently in single molecule experiments and solution spectroscopy when adding bad solvent.[40,45,48,169] For such cases it is well known that there is an efficient energy transfer from blue sites (unstacked) to a limited number of red sites (backbone stacked) in collapsed MEH-PPV.[37,94]

Upon doping MEH-PPV nanoparticles with 75 wt % PCBM, an interesting observation is made. One might expect the data for 75 wt % PCBM doped MEH-PPV nanoparticles to

be comparable with 50 wt % PCBM doped MEH-PPV nanoparticles. However, the single particle spectra of 75 wt % PCBM doped MEH-PPV nanoparticles are in fact in between those of single particle spectra of 5 wt % and 25 wt % PCBM doped MEH-PPV nanoparticles, albeit more similar to the 25 wt % case. These data show that most of the detected emission is contributed by blue type emitters, but in addition emission from the red type emitters does exist in this case. We assign this observation to phase separation, which has been reported to occur at high doping level of either C_{60} or PCBM in conjugated polymers bulk thin films.[41,170,171] The TEM image in Figure 4.2 b shows contrast (dark areas consistent with electron rich PCBM domains) within the nanoparticles that suggests that phase separation may be taking place, although the image does not provide unambiguous evidence. Furthermore, our single particle investigation clearly illustrates that in the case of phase separation PCBM rich areas are formed with only a few MEH-PPV molecules, while the MEH-PPV rich areas still contain a considerable fraction of PCBM. This is evident from the fact that the measured single particle spectra are comparable to the single particle spectra of 25 wt % PCBM doped MEH-PPV nanoparticles.

4.3.2 Single Particle Ensembles

By considering a large number of single particle spectra for each nanoparticle composition a distribution of properties can be obtained from the experimental and fitted data by compiling the data obtained for individual nanoparticles into single particle ensembles, see Figure 4.6. The data in Figure 4.6 a-e further illustrate the discussion presented above in terms of occurrence and relative intensity of blue and red type emitters in the emission spectra for the single particle ensembles, and also show the

distribution of energies of the 0-0 vibronic origins of the blue type and red type emitters for the different particle compositions. A slight blue shift of the vibronic origin is observed for doping levels up to 50 wt % PCBM for the blue emitters, supporting the idea that the morphology of the MEH-PPV nanoparticles becomes more disordered due to interruption of interactions between polymer chains with increasing doping levels of PCBM (up to 50 wt %). This corresponds well the observations made for the peak emission histograms shown in Figure 4.4. However, a slight red shift of the average vibronic origin is observed for the red type emitters with increasing PCBM doping levels. This may be due to the fact that PCBM is a poor solvent for MEH-PPV, which could result in stronger collapse of molecules i.e. into a globule with stronger aggregation interactions at red sites. Finally, the MEH-PPV nanoparticles doped with 75 wt % PCBM appear as they are doped somewhere in between 5 and 25 wt% PCBM due to the presence of both MEH-PPV/PCBM blended regions and phase segregated PCBM rich areas in these nanoparticles.

In addition, the histograms in Figure 4.7 a-e and Figure 4.7 f-j show the distribution of the Huang-Rhys factors for the blue and red type emitters, respectively. These histograms were constructed from the values of S_{blue} and S_{red} that were determined from fitting the individual single particle emission spectra to the Franck-Condon models described above, the averages of which are summarized in Table 4.1.

Table 4.1 Summary of parameters obtained from fitting single particle spectra to the Franck-Condon model reported in equation 4.5. S blue and S red represent the Huang-Rhys factors for the molecular and aggregate type emitters, while Wavenumber blue, Wavenumber red, and Amp blue and Amp red are the (0-0) origins of the molecular and aggregate type emitters with their corresponding amplitudes, respectively. The data in this Table represent the average of over 300 nanoparticles for each composition (expressed by wt % PCBM doping levels).

Doping	S blue	S red	Amp blue	Amp red	Wavenumber blue	Wavenumber red
0 wt %	0.30 ± 0.10	1.27 ± 0.14	1.72 ± 1.44	2.52 ± 2.07	16.80 ± 0.07	15.95 ± 0.11
5 wt %	0.36 ± 0.11	1.22 ± 0.21	1.34 ± 1.00	1.30 ± 1.01	16.79 ± 0.10	15.82 ± 0.16
25 wt %	0.49 ± 0.07	1.21 ± 0.21	2.31 ± 1.73	1.06 ± 1.08	16.87 ± 0.05	15.85 ± 0.13
50 wt %	0.81 ± 0.05	-	6.35 ± 5.39	-	16.93 ± 0.11	-
75 wt %	0.41 ± 0.10	1.16 ± 0.19	0.98 ± 0.66	0.72 ± 0.49	16.87 ± 0.13	15.86 ± 0.13

These data show a clear trend where the average S_{blue} increases as the doping level of PCBM increases up to 50 wt %, and then decreases for 75 wt %. The Huang-Rhys factor has been shown to represent the extent of conjugation and exciton migration in conjugated polymers. [52,115,153,159,160] It can therefore be concluded that increasing trend of S_{blue} with increasing PCBM doping level indicates reduced exciton migration and increased self trapping of excitons, which corroborates that interchain aggregation is being hindered by the presence of PCBM. In addition, the subsequent decrease of S_{blue} at 75 wt % PCBM doping further supports the notion that phase separation occurs at these high doping levels, leading to conjugated polymer regions in the nanoparticle that are apparently less heavily doped and thus have a larger occurrence of aggregation interactions between polymer chains and consequently enhanced exciton migration properties. Interestingly, the distribution of S_{blue} at 50 wt % PCBM doping appears narrower than for the other nanoparticle compositions, suggesting that the nanoparticles

consist of isolated collapsed molecules with very similar exciton migration properties, consistent with fast intramolecular exciton migration to low energy sites in the collapsed globule. The average value of $S_{blue} = 0.81 \pm 0.05$ is very consistent with this interpretation and the presence of excitonic emitters only.[115,162,172]

The average S_{red} values obtained for the red type emitters present in the composite MEH-PPV nanoparticles doped with 0, 5, 25 and 75 wt % PCBM are also summarized in Table 4.1. We do not report an average S_{red} value or related distribution for the MEH-PPV nanoparticles doped with 50 wt % PCBM since the red emitters are absent in this case. There are three main observations to be considered comparing the S_{blue} values with the S_{red} values. First, the S_{red} values are much higher than the S_{blue} values, and S_{red} is typically larger than 1.[115] The high values of S_{red} indicate severe self trapping of excitons, resulting in very little exciton migration. This observation suggests that the red type emitters are aggregate sites that are localized, with exciton migration limited to delocalization at the red site. These findings correspond well with the picture of aggregate sites acting as energy sinks in conjugated polymer materials.[37] Second, the average of S_{red} decreases slightly upon addition of PCBM, consistent with the red shift of the 0-0 vibronic origin of red type emitters, which as discussed above could be due to PCBM acting as a poor solvent for MEH-PPV resulting in stronger intra- and intermolecular aggregation interactions. However, compared to molecular type emitters the aggregate sites show only small changes in of S_{red}. Considering the distinct changes in the relative intensities of the stick spectra it appears that aggregate sits are either present (and populated by energy transfer/exciton migration) or not present (or not populated by energy transfer/exciton migration) in a to a certain extent on-off fashion as opposed to a gradual

change of aggregation interactions as observed for molecular (blue) sites. Third, a broad distribution of S_{red} is observed for the various nanoparticle compositions that were studied. This is a key observation in that it indicates nanoscale structural variations in the morphologies of the aggregate sites in the polymer material, presumably due to variations in polymer chain folding and stacking at the aggregate sites, while until now these were assumed to be rather uniform in their morphologies.[150]

4.4 Conclusion

The photophysical and optoelectronic properties of conjugated polymer materials have been found to be very complex due to the formation of interchain excitations and exciton migration processes. These issues are very complex and difficult to address for bulk materials due to the large conformational disorder that exists for conjugated polymers and masking of observations at the molecular level by the bulk. By means of a recently developed composite nanoparticle system in combination with Single Particle Spectroscopy we were able to obtain molecular scale information pertinent to advancing the understanding of the structure-property relationships of bulk conjugated polymer/fullerene blended materials. Effects of dopant concentration on exciton migration, aggregation and phase separation with respect to material morphology have been elucidated in detail. In addition, a broad heterogeneous distribution of aggregate morphologies in blended conducting polymer materials, which can be attributed to variations in polymer chain folding and stacking at the aggregate sites were found. This observation illustrates the importance of considering the role of aggregate sites in conjugated polymer material function and properties. Furthermore, the reported results obtained by the SPS approach show how blending conjugated polymers with fullerenes at

various doping levels induces changes in interchain interactions and aggregate site density even at length scales below a few tens of nanometers.

CHAPTER 5. STUDY OF SINGLE PARTICLE FLUORESCENCE PROPERTIES OF MEH-PPV/PCBM NANOPARTICLES IN A DEVICE ENVIRONMENT: EFFECT OF ELECTRICAL FIELDS

5.1 Introduction

The leading organic photovoltaic cells reported so far use blended materials of conjugated polymers with electron accepting molecules such as C_{60}-fullerene derivatives as the active layer. For example, the organic photovoltaic cells prepared using active layers as poly[2-methyoxy-5-(3,7-dimethyloxtyloxy)-1,4-phenylene vinylene] (MDMO-PPV) or regioregular poly[3-hexylthiophene] (P3HT) with PCBM provide power conversion efficiencies (η) of approximately 3 % and 5 % respectively.[12,173,174],[16,175-178] In these blended materials, photoexcitation is followed by ultrafast (femtosecond time scale) photoinduced charge transfer from the conjugated polymers to the PCBM at their interfaces resulting in the formation of radical cations and anions.[179] In these devices, the charge transfer process is highly efficient in which the internal quantum efficiency reaches close to unity. Despite the high quantum efficiency, the charge separation process at the interface and its dependence on the composition is not fully understood. In this chapter, the fabrication of a field-only device is discussed, and the investigation of the fluorescence properties of composite MEH-PPV/PCBM nanoparticles in these devices is reported. The goal is to elucidate the effect of applied electrical fields on the interfacial charge transfer processes occurring in composite MEH-PPV/PCBM nanoparticles. One of the questions we want to address is: would the charge transfer process be enhanced, reduced or remain unchanged with applied electrical field? For example, if the fluorescence intensity of the composite MEH-PPV/PCBM increases with the applied electrical field, this indicates the interfacial charge transfer rate is reduced in the presence

of applied electrical field and vice versa. In the field-only device, there is no current but an electric field is present. This is achieved by fabricating the device that consists of a thick insulting layer of SiO_2 on top of ITO glass substrate followed by spin-coating of composite MEH-PPV/PCBM nanoparticles and followed by deposition of a metal such as gold in which the ITO and gold act as the electrodes. The information gained from the experiment may provide us with a better understanding of the electronic structure of the materials.

5.2 Results and discussion

The fluorescence confocal image and the spectra of different MEH-PPV nanoparticles in a device sample are shown in Figure 5.1.

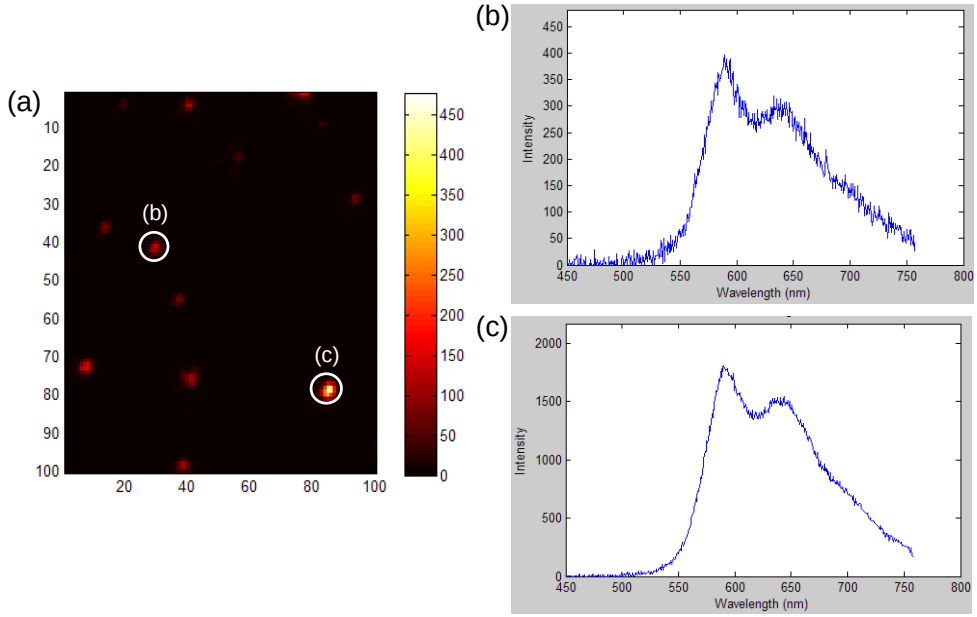

Figure 5.1 (a) Fluorescence confocal image of the MEH-PPV nanoparticles in the device. The scan range is 10 µm by 10 µm. The excitation wavelength is 488 nm and the laser power of 1.0 nW is used. (b) Single particle spectrum of the MEH-PPV nanoparticle labeled as (b) in the fluorescence confocal image in (a). (c) Single particle spectrum of the MEH-PPV nanoparticle labeled as (c) in the fluorescence confocal image in (a).

As it can be seen in the single particle spectra (Figure 5.1 b and c) obtained from the fluorescent spots found in the device samples correspond well with the MEH-PPV nanoparticles, showing that the device fabrication procedures do not significantly alter the nanoparticle properties. The fluorescence confocal image (Figure 5.2 a) and transients (Figure 5.2 b-f) of undoped MEH-PPV nanoparticles are collected at different voltages, see Figure 5.2. The transients of the MEH-PPV nanoparticles are collected without applying voltage followed by applying voltages of 1 V, 5 V, and 10 V in a sequential manner. The time period for collecting each transient is 30 seconds. As it can be seen, the transients collected from the MEH-PPV nanoparticles do not show any change as function of applied voltage. In other words, the fluorescence intensity of the single MEH-PPV nanoparticles remains constant while applying various voltages onto the device.

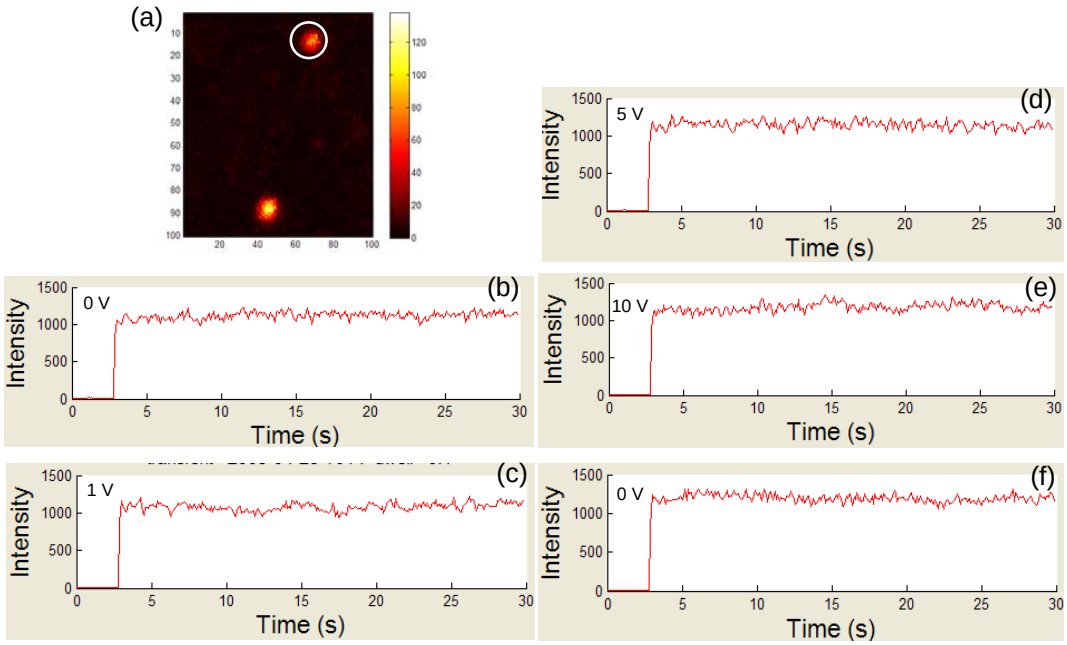

Figure 5.2 (a) Fluorescence confocal image of the MEH-PPV nanoparticles in the device. The order of the layers in the device is as followed: ITO glass substrate, SiO_2, PMMA, MEH-PPV nanoparticles in PVA, PMMA, and Al. The scan range is 6 µm by 6 µm. (b) Transients of the MEH-PPV nanoparticle that is circled in white. Transients are collected every 30 seconds in the following order of voltage applied: 0 V, 1 V, 5 V, 10 V and 0 V.

A fluorescence confocal image and spectra of different 50 wt % PCBM doped MEH-PPV nanoparticles embedded in a device are shown in Figure 5.3.

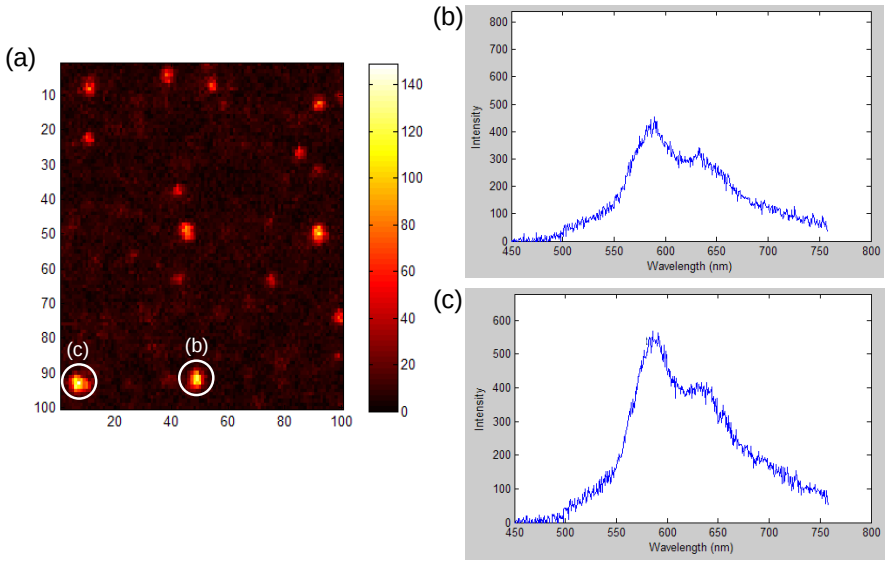

Figure 5.3 (a) Fluorescence confocal image of the MEH-PPV nanoparticles doped with 50 wt % PCBM in the device. The scan range is 9 µm by 9 µm. The excitation wavelength is 488 nm and the laser power of 10 nW is used. (b) Single particle spectrum of the 50 wt % PCBM doped MEH-PPV nanoparticle labeled as (b) in the fluorescence confocal image in (a). (c) Single particle spectrum of the 50 wt % PCBM doped MEH-PPV nanoparticle labeled as (c) in the fluorescence confocal image in (a).

Again the emission spectra appear as expected, showing that the device fabrication procedures do not significantly alter the nanoparticle properties. A confocal fluorescence image (Figure 5.4 a) and transients (Figure 5.4 b-f) of the MEH-PPV nanoparticles doped with 50 wt % PCBM collected at different voltages is shown in Figure 5.4. The transients of the MEH-PPV nanoparticles doped with 50 wt % PCBM are collected without applying voltage followed by applying voltages of 1 V, 5 V, and 10 V in a sequential manner. The time period for collecting each transient is 30 seconds. As it can be seen, the fluorescence intensity decreases each time collecting transients. This is due to sample drift and not due to applying voltage.

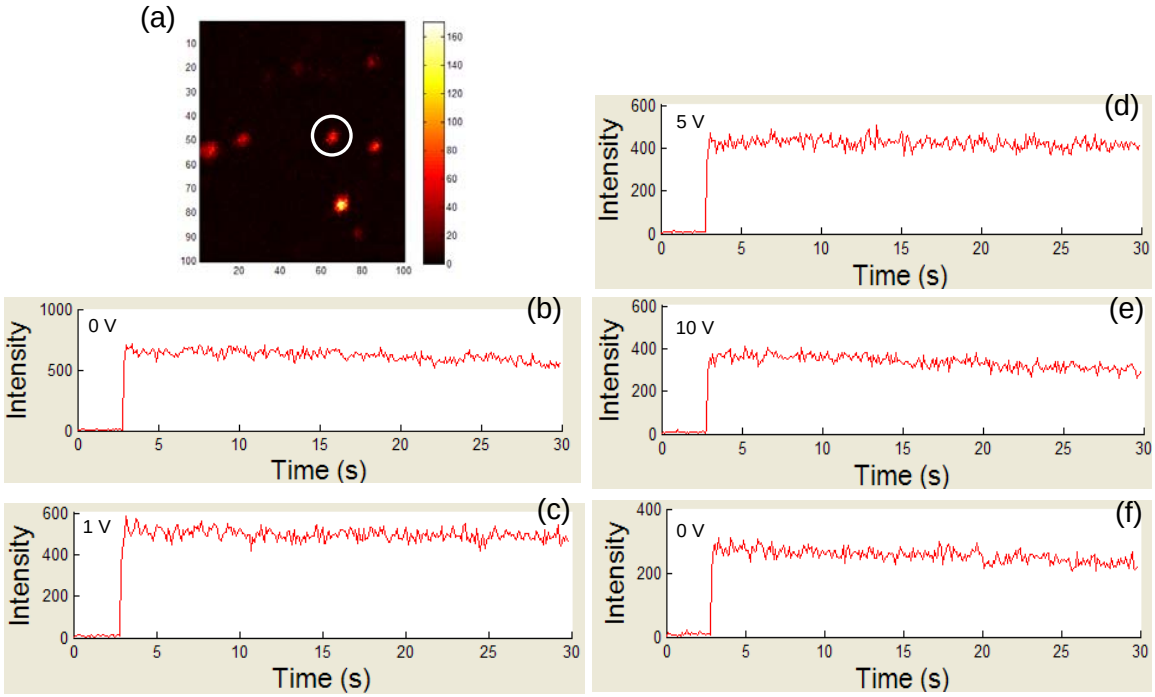

Figure 5.4 (a) Fluorescence confocal image of the MEH-PPV nanoparticles doped with 50 wt % PCBM in the device. The order of the layers in the device is as followed: ITO glass substrate, SiO_2, PMMA, MEH-PPV nanoparticles doped with 50 wt % PCBM in PVA, PMMA, and Al. The scan range is 7 µm by 7 µm. (b) Transients of the MEH-PPV nanoparticle doped with 50 wt % PCBM that is circled in white. Transients are collected every 30 seconds in the following order of voltage applied: 0 V, 1 V, 5 V, 10 V and 0 V.

5.3 Conclusion

In this chapter, field-only devices were fabricated to investigate the effect of applied electrical fields on the interfacial charge transfer processes in composite MEH-PPV/PCBM nanoparticles. The transients of the individual composite MEH-PPV/PCBM nanoparticles were collected as function of applied electrical fields. Our data show that there is no observable effect on the fluorescence intensity of the individual composite MEH-PPV/PCBM nanoparticles. This indicates that the interfacial electron charge transfer rates do not change upon applied electrical fields similar to those found in fully functional devices.

CHAPTER 6. DIFFUSION OF MEH-PPV NANOPARTICLES INSIDE HOLLOW LIPID NANOTUBES

6.1 Introduction

Diffusion in confined geometries is a fundamental problem that is at the forefront of physical chemistry due to the current trend towards nanotechnology and nanodevices.[180,181] The development in this field has opened up the potential for significant technological advances in catalysis, trapping of contaminants, chromatographic analysis, molecular sieving, and nanofluidic devices. In addition, with the advent of nanobiotechnology and nanomedicine, a fundamental understanding of how physical processes and biochemical reactions proceed in nanoscale environments is needed.[182]

In fact, there are numerous biologically relevant processes such as diffusion through cell membranes, cell-to-cell communication, single cell addressing and manipulation by micro- or nanoinjection involve uptake, transport and/or delivery of molecules in confined geometries imposed by lipid membranes. Lipid tubules have been shown to be an excellent candidate to study as it can mimic the confined geometry in the biological systems. They are synthesized through modification of head groups or alkyl chains lipids in which form open-ended tubular structures in solutions by chiral molecular self-assembly and packing directed self-assembly.[183-209] The diameters of self-assembled lipid tubules span the range between 10 nm to 2.0 μm, depending on the nature of lipid molecules and the condition under which self-assembly occurs.

There have been many reports on the self-assembled lipid tubules which are utilized as a controlled release system for drugs and genes.[27-30,34,210-215] Some of the advantages of lipid tubule-based delivery systems are; they are biocompatible, injectable (can be

localized to specific site) and do not involve residual organic solvents (no need to mix immiscible phases).[27,210] However, the mechanism of slow and sustained release of bioactive agents from lipid tubules is not fully understood. It has been suggested that the release rate of bioactive agents is associated with their diffusivity in lipid tubules, but very little is know on their diffusion behavior inside lipid tubules. The detailed understanding of how the sizes, phases and surface properties of lipid tubules affect the release rate of bioactive agents will provide the possibility of designing lipid tubules for achieving their sustained release over a targeted period of time.

The diffusion of molecules confined in mesoporous materials[216-218], gels[219], vesicles [220,221], and silica nanotubes [53,222], has been studied with neutron scattering, NMP, and optical methods. In the case of optical tracking of fluorescent molecules, fluorescence correlation spectroscopy (FCS) or fluorescence recovery after photobleaching (FRAP) are the most prevalent approaches. However, these methods do not provide the detailed molecular level mechanistic and kinetic information on the motion of the confined molecules. Optical single molecule detection has been shown to be an excellent approach for the study of single molecule diffusion through single particle tracking (SPT) [223] and has been applied in the study of single molecular diffusion in mesoporous silica.[217,224-228]

In this chapter, samples of $DC_{8,9}PC$ lipid nanotubes [55] with a diameter of approximately 0.5 μm and a length ranging from 5 to 100 μm, provided by Dr. Jiyu Fang from the Advanced Materials Processing and Analysis Center (AMPAC), were studied. We introduced the MEH-PPV nanoparticles with a size of approximately 30 nm to the $DC_{8,9}PC$ lipid nanotubes, to investigate the diffusion process in the interior of $DC_{8,9}PC$ lipid nanotubes. The molecular diffusion study of MEH-PPV nanoparticles in the

$DC_{8,9}PC$ lipid nanotubes was achieved by single particle imaging in wide-field configuration, also often referred to as Single Particle Tracking.

6.2 Results and discussion

Bright field and fluorescence confocal (referred to as APD image) images of the dehydrated $DC_{8,9}PC$ lipid nanotubes sample 1 are shown in Figure 6.1. As it can be seen the size of the $DC_{8,9}PC$ lipid nanotubes varies greatly in their diameter and length. In addition, many of the $DC_{8,9}PC$ lipid nanotubes are very close of each other and overlay on top of each other. However, there are some isolated single $DC_{8,9}PC$ lipid nanotubes that can be observed. The $DC_{8,9}PC$ lipid nanotubes are slightly fluorescent which can be seen in the APD image in Figure 6.1.

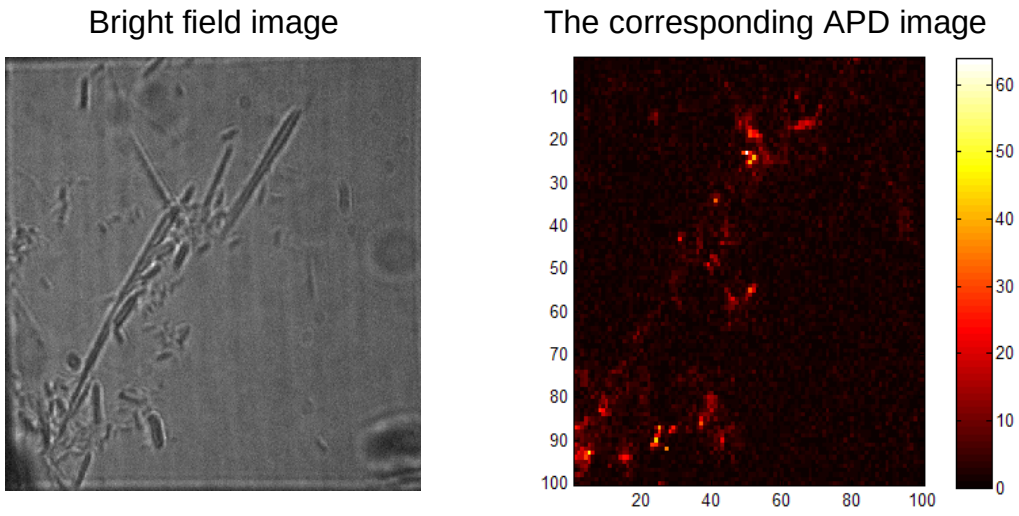

Figure 6.1 The bright field and the corresponding APD images of the dehydrated $DC_{8,9}PC$ lipid nanotubes. The excitation wavelength is 488 nm and the laser power of 1.0 nW is used.

To investigate the single particle diffusion inside of the $DC_{8,9}PC$ lipid nanotubes, the MEH-PPV nanoparticles which were previously prepared (see chapter 3) were introduced into the nanotubes. The bright field and APD images of the dehydrated $DC_{8,9}PC$ lipid nanotubes with MEH-PPV nanoparticles sample 2 are shown Figure 6.2.

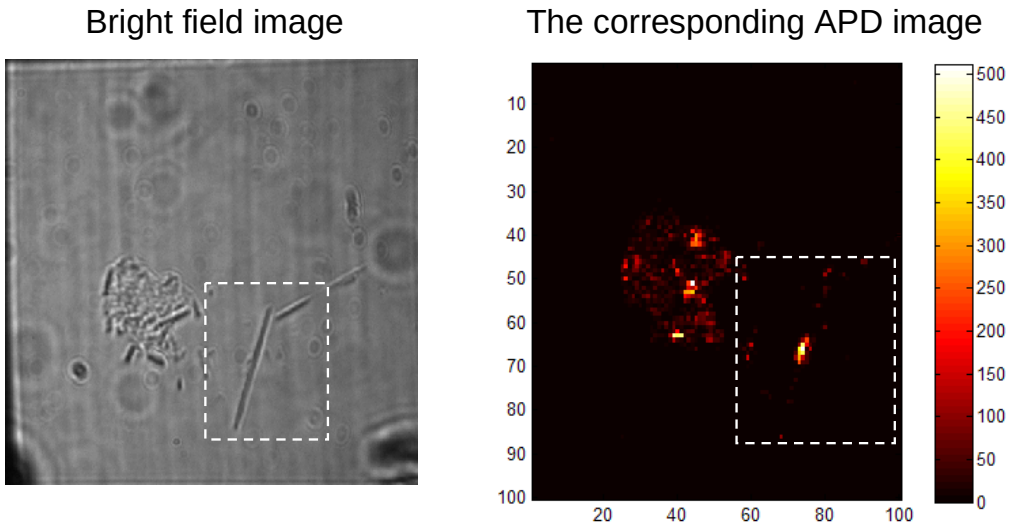

Figure 6.2 The bright field and the corresponding APD images of the dehydrated $DC_{8,9}PC$ lipid nanotubes with MEH-PPV nanoparticles. The scan range is 50 μm by 50 μm. The excitation wavelength is 488 nm and the laser power of 1.0 nW is used.

As it can be seen, there are both isolated and cluster areas of $DC_{8,9}PC$ lipid nanotubes present in the bright field image. Since we are interested in studying the diffusion of single MEH-PPV nanoparticle inside a nanotube, we considered the isolated $DC_{8,9}PC$ lipid nanotube area which is shown in a dotted box in Figure 6.2.The zoomed in ADP image of the dotted box is shown in Figure 6.3 a. Subsequently, the APD image is zoomed in onto the dotted box area indicated in Figure 6.3 a and the APD image of the zoomed in area is shown in Figure 6.3 b. The APD image displays the individual nanoparticles which outlines the shape of $DC_{8,9}PC$ lipid nanotube however, it can not be

conclusive about whether the MEH-PPV nanoparticles are inside of the $DC_{8,9}PC$ lipid nanotube from this data. It is most likely that the MEH-PPV nanoparticles are adsorbed onto the exterior of the $DC_{8,9}PC$ lipid nanotubes. The spectra of the MEH-PPV nanoparticles were collected (i.e. circled Figure 6.3 b) and one is shown in Figure 6.3 c. The spectrum collected confirms that it is the MEH-PPV nanoparticle.

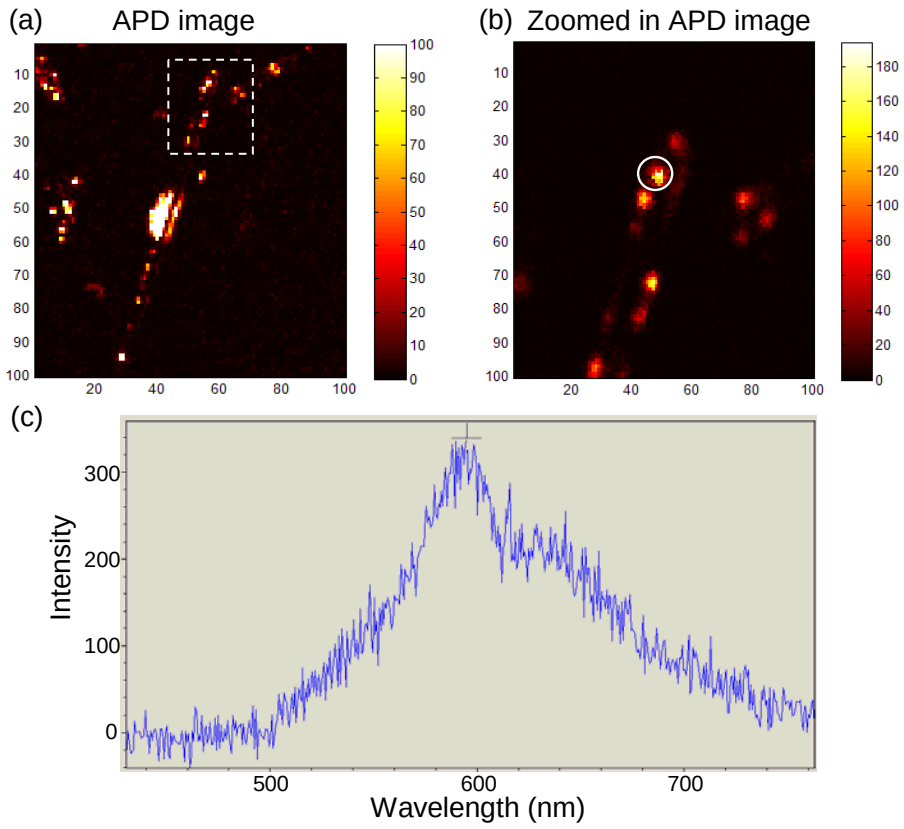

Figure 6.3 (a) The zoomed in APD image of Figure 6.2. The scan range is 23 μm by 23 μm (b) The zoomed in APD image of Figure 6.3 a. The scan range is 7 μm by 7 μm. (c) The single particle spectrum of the MEH-PPV nanoparticle which is indicated with a white circle in Figure 6.3 b. The excitation wavelength is 488 nm and the laser power of 1.0 nW is used.

To investigate diffusion of single MEH-PPV nanoparticles in the nanotubes, the bright field images and the corresponding wide field images of sample 2 are collected. In addition, the movie of the sample is obtained as to observe the diffusion of the single

nanoparticle inside the $DC_{8,9}PC$ lipid nanotube. In Figure 6.4, the bright field and the corresponding wide field images of sample 2 is shown.

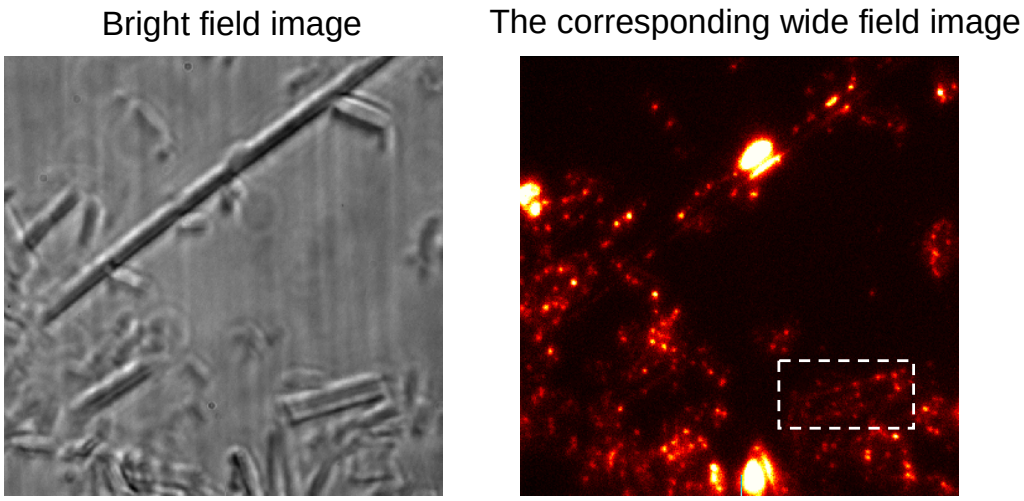

Figure 6.4 The bright field and the corresponding wide field images of the dehydrated $DC_{8,9}PC$ lipid nanotubes with MEH-PPV nanoparticles. The dotted box in the wide field image shows two individual MEH-PPV nanoparticles inside the nanotube. The excitation wavelength is 488 nm and the laser power of 64 μW is used.

From this experiment, it can be observed that the most of the MEH-PPV nanoparticles are adsorbed onto the exterior of $DC_{8,9}PC$ lipid nanotubes. Individual MEH-PPV nanoparticles are rarely found inside the nanotube. When the nanotubes are dehydrated, the hollow cylindrical shape of the nanotubes collapses and changes to a flattened shape. Thus, it is difficult for the MEH-PPV nanoparticles to enter the inside of nanotube even though the diameter of the nanotube is much larger than the size of MEH-PPV nanoparticles. Our next experiment therefore involved the re-hydration of the nanotubes in order avoid the flattening of the $DC_{8,9}PC$ lipid nanotubes. By re-hydrating the nanotubes, the nanotubes gain back their cylindrical shape in which the hollow center of the nanotube is filled with water. Thus, this may allow the MEH-PPV nanoparticles to

enter the inside of the nanotubes. In Figure 6.5, the bright field and wide field images of nanotubes with MEH-PPV nanoparticles sample 3 is shown.

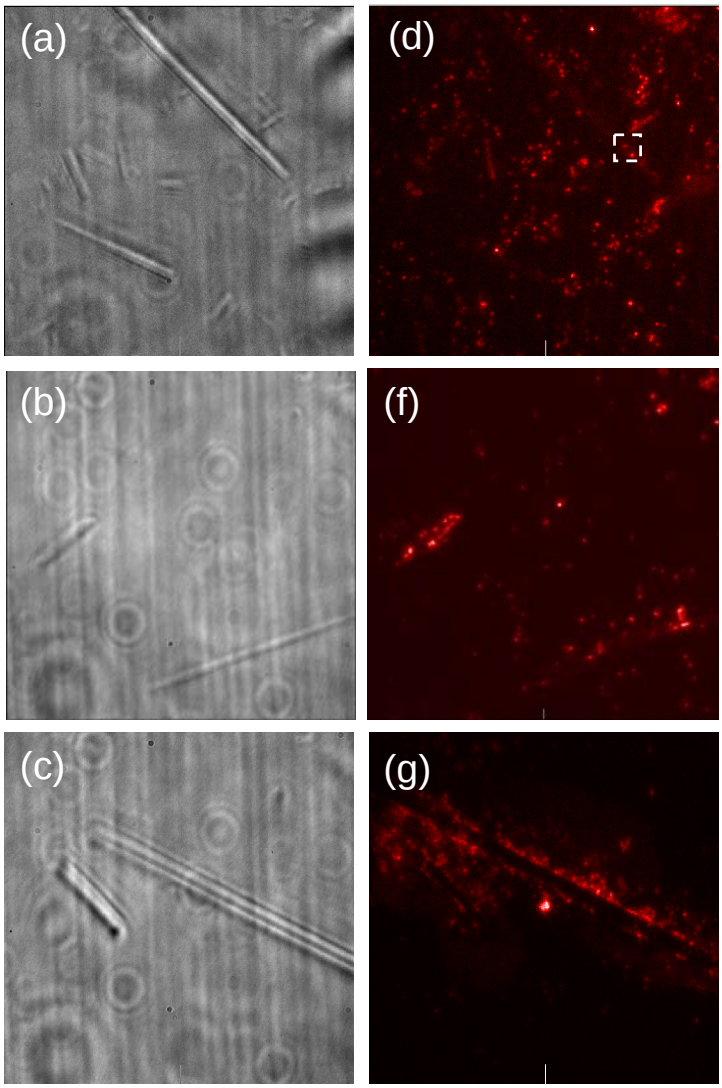

Figure 6.5 (a-c) Bright field images of re-hydrated $DC_{8,9}PC$ lipid nanotubes with MEH-PPV nanoparticles. (d-f) The corresponding wide images of the bright field images that are shown in (a), (b), and (c) respectively. The dotted box shows the individual nanoparticles that are inside of the $DC_{8,9}PC$ lipid nanotube.

As it can be seen the most of the MEH-PPV nanoparticles are adsorbed on the edges of the nanotubes even in the re-hydrated nanotube conditions. Individual MEH-PPV

nanoparticles inside of the nanotubes are rarely observed. In addition, some moving nanotubes are observed when a movie is taken due to the fact the sample is under water. When the single MEH-PPV nanoparticles are observed inside of the $DC_{8,9}PC$ lipid nanotubes, diffusion of the single MEH-PPV nanoparticle is observed. The diffusion was captured through a video clip by collecting 150 frames for 60 seconds in wide field mode. In Figure 6.6, two individual MEH-PPV nanoparticles are inside of the $DC_{8,9}PC$ lipid nanotube and the diffusion of the MEH-PPV nanoparticle can be observed.

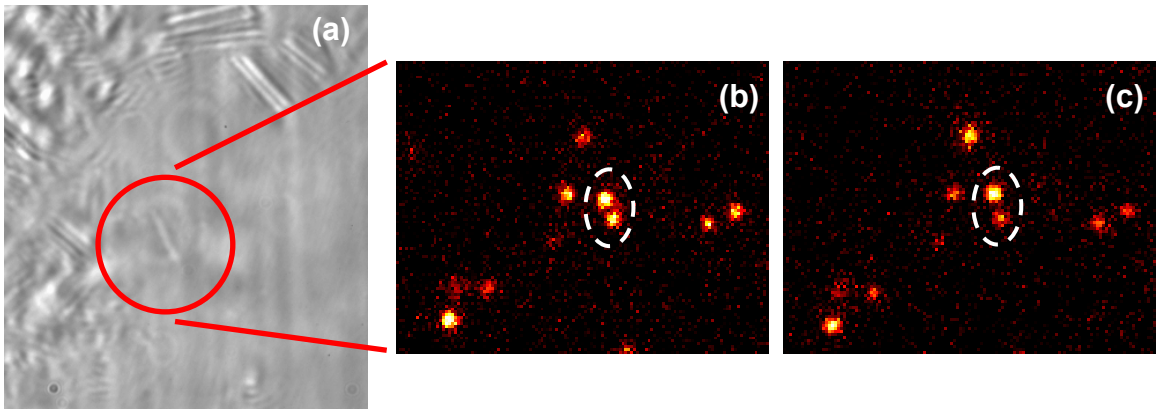

Figure 6.6 (a) Bright field image of re-hydrated $DC_{8,9}PC$ lipid nanotubes with MEH-PPV nanoparticles. (b)The corresponding wide image of the bright field image that are shown in (a). The dotted circle shows the individual nanoparticles that are inside of the $DC_{8,9}PC$ lipid nanotube before diffusion. (c) The corresponding wide image of the bright field image that are shown in (a). The dotted circle shows the individual nanoparticles that are inside of the $DC_{8,9}PC$ lipid nanotube after diffusion.

As it can be in Figure 6.6, diffusion of single MEH-PPV nanoparticles inside the hollow $DC_{8,9}PC$ lipid nanotubes can be studied via SPS. This method demonstrates the capability of investigating single compacted DNA diffusion in self-assembled lipid tubes which will lead to a better understanding of DNA diffusion in biomimetic confined geometries. This can contribute to improved or new design rules and principles for potential applications of tubule-based gene delivery systems.

6.3 Conclusion

In this chapter, we investigated the study of single particle diffusion kinetics of the MEH-PPV nanoparticles inside of $DC_{8,9}PC$ lipid nanotubes through single molecule/particle spectroscopy. Our results show that the cylindrical shape of the $DC_{8,9}PC$ lipid nanotubes collapses into a flatten shape upon dehydration of the sample. Thus, most of the MEH-PPV nanoparticles adsorbed on the exterior of the $DC_{8,9}PC$ lipid nanotubes. In fact, both samples types that we studied (dehydrated and rehydrated) show that the most MEH-PPV nanoparticles adsorb on the exterior of the $DC_{8,9}PC$ lipid nanotubes. Only a few times were the MEH-PPV nanoparticles inside of the $DC_{8,9}PC$ lipid nanotubes. We attribute this observation to hydrophobic interactions between the MEH-PPV nanoparticles and the exterior wall of the lipid nanotubes. However, we observed single MEH-PPV nanoparticles inside of $DC_{8,9}PC$ lipid nanotubes in a few occasions. For these cases, we were able to capture the diffusion of the single MEH-PPV nanoparticles inside of the $DC_{8,9}PC$ lipid nanotubes. These data give a clear proof of concept that diffusion of nanoparticles inside the hollow lipid nanotubes can be studied on a single particle basis, which will allow us to study diffusion processes quantitatively and mechanistically within the framework of developing a biocompatible drug and gene delivery platform.

APPENDIX: LIST OF PUBLICATIONS

Gesquiere, A. J.; Tenery, D.; Hu, Z. J. *Spectroscopy* **2008**, *23*, 32-44.

Tenery, D.; Worden, J. G.; Hu, Z. J.; Gesquiere, A. J. *Journal of Luminescence* **2009**, *129*, 423-429.

Hu, Z. J.; Tenery, D.; Bonner, M. S.; Gesquiere, A. J. *Journal of Luminescence* **2009,** submitted.

Tenery, D.; Gesquiere, A. J. *ChemPhysChem* **2009,** accepted.

Tenery, D.; Gesquiere, A. J. *Chemical Physics* **2009,** submitted.

REFERENCES

(1) Gunes, S.; Neugebauer, H.; Sariciftci, N. S. *Chemical Reviews* **2007**, *107*, 1324-1338.
(2) Winder, C.; Sariciftci, N. S. *Journal of Materials Chemistry* **2004**, *14*, 1077-1086.
(3) Dittmer, J. J.; Marseglia, E. A.; Friend, R. H. *Advanced Materials* **2000**, *12*, 1270-+.
(4) Greenham, N. C.; Peng, X. G.; Alivisatos, A. P. *Physical Review B* **1996**, *54*, 17628-17637.
(5) Halls, J. J. M.; Walsh, C. A.; Greenham, N. C.; Marseglia, E. A.; Friend, R. H.; Moratti, S. C.; Holmes, A. B. *Nature* **1995**, *376*, 498-500.
(6) Hasobe, T.; Imahori, H.; Kamat, P. V.; Ahn, T. K.; Kim, S. K.; Kim, D.; Fujimoto, A.; Hirakawa, T.; Fukuzumi, S. *Journal of the American Chemical Society* **2005**, *127*, 1216-1228.
(7) Hoppe, H.; Glatzel, T.; Niggemann, M.; Schwinger, W.; Schaeffler, F.; Hinsch, A.; Lux-Steiner, M. C.; Sariciftci, N. S. *Thin Solid Films* **2006**, *511*, 587-592.
(8) Huynh, W. U.; Dittmer, J. J.; Alivisatos, A. P. *Science* **2002**, *295*, 2425-2427.
(9) Kamat, P. V. *Journal of Physical Chemistry B* **2002**, *106*, 7729-7744.
(10) Nasr, C.; Hotchandani, S.; Kim, W. Y.; Schmehl, R. H.; Kamat, P. V. *Journal of Physical Chemistry B* **1997**, *101*, 7480-7487.
(11) Ramakrishna, G.; Jose, D. A.; Kumar, D. K.; Das, A.; Palit, D. K.; Ghosh, H. N. *Journal of Physical Chemistry B* **2005**, *109*, 15445-15453.
(12) Shaheen, S. E.; Brabec, C. J.; Sariciftci, N. S.; Padinger, F.; Fromherz, T.; Hummelen, J. C. *Applied Physics Letters* **2001**, *78*, 841-843.
(13) Tachibana, Y.; Moser, J. E.; Gratzel, M.; Klug, D. R.; Durrant, J. R. *Journal of Physical Chemistry* **1996**, *100*, 20056-20062.
(14) Yu, G.; Gao, J.; Hummelen, J. C.; Wudl, F.; Heeger, A. J. *Science* **1995**, *270*, 1789-1791.
(15) Hoppe, H.; Sariciftci, N. S. *Journal of Materials Research* **2004**, *19*, 1924-1945.
(16) Li, G.; Shrotriya, V.; Huang, J. S.; Yao, Y.; Moriarty, T.; Emery, K.; Yang, Y. *Nature Materials* **2005**, *4*, 864-868.
(17) van Duren, J. K. J.; Yang, X. N.; Loos, J.; Bulle-Lieuwma, C. W. T.; Sieval, A. B.; Hummelen, J. C.; Janssen, R. A. J. *Advanced Functional Materials* **2004**, *14*, 425-434.
(18) Berleb, S.; Brutting, W.; Paasch, G. *Organic Electronics* **2000**, *1*, 41-47.
(19) Berleb, S.; Brutting, W.; Paasch, G. *Synthetic Metals* **2001**, *122*, 37-39.
(20) Nesterov, A.; Paasch, G.; Scheinert, S.; Lindner, T. *Synthetic Metals* **2002**, *130*, 165-175.
(21) Nguyen, P. H.; Scheinert, S.; Berleb, S.; Brutting, W.; Paasch, G. *Organic Electronics* **2001**, *2*, 105-120.
(22) Paasch, G.; Nesterov, A.; Scheinert, S. *Synthetic Metals* **2003**, *139*, 425-432.
(23) Paasch, G.; Peisert, H.; Knupfer, M.; Fink, J.; Scheinert, S. *Journal of Applied Physics* **2003**, *93*, 6084-6089.
(24) Paasch, G.; Scheinert, S. *Synthetic Metals* **2001**, *122*, 145-147.
(25) Paasch, G.; Scheinert, S. *Synthetic Metals* **2003**, *135*, 407-408.

(26) Scheinert, S.; Paasch, G.; Schrodner, M.; Roth, H. K.; Sensfuss, S.; Doll, T. *Journal of Applied Physics* **2002**, *92*, 330-337.
(27) Rudolph, A. S.; Stilwell, G.; Cliff, R. O.; Kahn, B.; Spargo, B. J.; Rollwagen, F.; Monroy, R. L. *Biomaterials* **1992**, *13*, 1085-1092.
(28) Schnur, J. M.; Price, R.; Rudolph, A. S. *Journal of Controlled Release* **1994**, *28*, 3-13.
(29) Price, R. R.; Schnur, J. M. *Journal of Coatings Technology* **2003**, *75*, 53-+.
(30) Meilander, N. J.; Pasumarthy, M. K.; Kowalczyk, T. H.; Cooper, M. J.; Bellamkonda, R. V. *Journal of Controlled Release* **2003**, *88*, 321-331.
(31) Fang, J. M.; Zhu, Y. Y.; Smiley, E.; Bonadio, J.; Rouleau, J. P.; Goldstein, S. A.; McCauley, L. K.; Davidson, B. L.; Roessler, B. J. *Proceedings of the National Academy of Sciences of the United States of America* **1996**, *93*, 5753-5758.
(32) Shea, L. D.; Smiley, E.; Bonadio, J.; Mooney, D. J. *Nature Biotechnology* **1999**, *17*, 551-554.
(33) Wang, D. Q.; Robinson, D. R.; Kwon, G. S.; Samuel, J. *Journal of Controlled Release* **1999**, *57*, 9-18.
(34) Goldstein, A. S.; Gelb, M. H.; Yager, P. *Journal of Controlled Release* **2001**, *70*, 125-138.
(35) Tokarz, M.; Akerman, B.; Olofsson, J.; Joanny, J. F.; Dommersnes, P.; Orwar, O. *Proceedings of the National Academy of Sciences of the United States of America* **2005**, *102*, 9127-9132.
(36) Hurtig, J.; Gustafsson, B.; Tokarz, M.; Orwar, O. *Analytical Chemistry* **2006**, *78*, 5281-5288.
(37) Schwartz, B. J. *Annual Review of Physical Chemistry* **2003**, *54*, 141-172.
(38) Barbara, P. F. *Accounts Of Chemical Research* **2005**, *38*, 503-503.
(39) Nguyen, T. Q.; Schwartz, B. J.; Schaller, R. D.; Johnson, J. C.; Lee, L. F.; Haber, L. H.; Saykally, R. J. *Journal of Physical Chemistry B* **2001**, *105*, 5153-5160.
(40) Padmanaban, G.; Ramakrishnan, S. *Journal Of Physical Chemistry B* **2004**, *108*, 14933-14941.
(41) Hoppe, H.; Niggemann, M.; Winder, C.; Kraut, J.; Hiesgen, R.; Hinsch, A.; Meissner, D.; Sariciftci, N. S. *Advanced Functional Materials* **2004**, *14*, 1005-1011.
(42) Dante, M.; Garcia, A.; Nguyen, T.-Q. *Journal of Physical Chemistry C* **2009**, *113*, 1596-1600.
(43) Nguyen, T. Q.; Doan, V.; Schwartz, B. J. *Journal Of Chemical Physics* **1999**, *110*, 4068-4078.
(44) Zhang, H. R.; Lu, X. F.; Li, Y.; Ai, X. C.; Zhang, X. K.; Yang, G. Q. *Journal of Photochemistry and Photobiology a-Chemistry* **2002**, *147*, 15-23.
(45) Traiphol, R.; Sanguansat, P.; Srikhirin, T.; Kerdcharoen, T.; Osotchan, T. *Macromolecules* **2006**, *39*, 1165-1172.
(46) Shi, Y.; Liu, J.; Yang, Y. *Journal of Applied Physics* **2000**, *87*, 4254-4263.
(47) Wang, P.; Cuppoletti, C. M.; Rothberg, L. J. *Synthetic Metals* **2003**, *137*, 1461-1463.
(48) Grey, J. K.; Kim, D. Y.; Norris, B. C.; Miller, W. L.; Barbara, P. F. *Journal of Physical Chemistry B* **2006**, *110*, 25568-25572.
(49) Szymanski, C.; Wu, C. F.; Hooper, J.; Salazar, M. A.; Perdomo, A.; Dukes, A.; McNeill, J. *Journal of Physical Chemistry B* **2005**, *109*, 8543-8546.

(50) VandenBout, D. A.; Yip, W. T.; Hu, D. H.; Fu, D. K.; Swager, T. M.; Barbara, P. F. *Science* **1997**, *277*, 1074-1077.
(51) Gesquiere, A. J.; Park, S. J.; Barbara, P. F. *Journal of Physical Chemistry B* **2004**, *108*, 10301-10308.
(52) Yu, Z. H.; Barbara, P. F. *Journal of Physical Chemistry B* **2004**, *108*, 11321-11326.
(53) Jayaraman, K.; Okamoto, K.; Son, S. J.; Luckett, C.; Gopalani, A. H.; Lee, S. B.; English, D. S. *Journal of the American Chemical Society* **2005**, *127*, 17385-17392.
(54) Wirth, M. J.; Swinton, D. J. *Analytical Chemistry* **1998**, *70*, 5264-5271.
(55) Guo, L.; Chowdhury, P.; Fang, J. Y.; Gai, F. *Journal of Physical Chemistry B* **2007**, *111*, 14244-14249.
(56) Kulzer, F.; Orrit, M. *Annual Review of Physical Chemistry* **2004**, *55*, 585-611.
(57) Moerner, W. E.; Fromm, D. P. *Review of Scientific Instruments* **2003**, *74*, 3597-3619.
(58) Nie, S.; Zare, R. *Annu. Rev. Biophys. Biomol. Struct.* **1997**, *26*, 567-596.
(59) Yip, W. T.; Hu, D. H.; Yu, J.; Vanden Bout, D. A.; Barbara, P. F. *Journal of Physical Chemistry A* **1998**, *102*, 7564-7575.
(60) English, D. S.; Furube, A.; Barbara, P. F. *Chemical Physics Letters* **2000**, *324*, 15-19.
(61) Ha, T.; Enderle, T.; Chemla, D. S.; Selvin, P. R.; Weiss, S. *Physical Review Letters* **1996**, *77*, 3979-3982.
(62) Ha, T.; Enderle, T.; Chemla, D. S.; Selvin, P. R.; Weiss, S. *Chemical Physics Letters* **1997**, *271*, 1-5.
(63) Kohn, F.; Hofkens, J.; Gronheid, R.; Van der Auweraer, M.; De Schryver, F. C. *Journal of Physical Chemistry A* **2002**, *106*, 4808-4814.
(64) Veerman, J. A.; Garcia-Parajo, M. F.; Kuipers, L.; van Hulst, N. F. *Physical Review Letters* **1999**, *83*, 2155-2158.
(65) Weston, K. D.; Carson, P. J.; DeAro, J. A.; Buratto, S. K. *Chemical Physics Letters* **1999**, *308*, 58-64.
(66) Basche, T.; Kummer, S.; Brauchle, C. *Nature* **1995**, *373*, 132-134.
(67) Basche, T.; Moerner, W. E.; Orrit, M.; Talon, H. *Physical Review Letters* **1992**, *69*, 1516-1519.
(68) Orrit, M.; Bernard, J. *Physical Review Letters* **1990**, *65*, 2716-2719.
(69) Ying, L. M.; Xie, X. S. *Journal of Physical Chemistry B* **1998**, *102*, 10399-10409.
(70) Hofkens, J.; Maus, M.; Gensch, T.; Vosch, T.; Cotlet, M.; Kohn, F.; Herrmann, A.; Mullen, K.; De Schryver, F. *Journal of the American Chemical Society* **2000**, *122*, 9278-9288.
(71) White, J. D.; Hsu, J. H.; Fann, W. S.; Yang, S. C.; Pern, G. Y.; Chen, S. A. *Chemical Physics Letters* **2001**, *338*, 263-268.
(72) Kasai, H.; Nalwa, H. S.; Oikawa, H.; Okada, S.; Matsuda, H.; Minami, N.; Kakuta, A.; Ono, K.; Mukoh, A.; Nakanishi, H. *Japanese Journal of Applied Physics Part 2-Letters* **1992**, *31*, L1132-L1134.
(73) Gesquiere, A. J.; Uwada, T.; Asahi, T.; Masuhara, H.; Barbara, P. F. *Nano Letters* **2005**, *5*, 1321-1325.
(74) Wang, F.; Han, M. Y.; Mya, K. Y.; Wang, Y. B.; Lai, Y. H. *Journal of the American Chemical Society* **2005**, *127*, 10350-10355.

(75) Tenery, D.; Worden, J. G.; Hu, Z. J.; Gesquiere, A. J. *Journal of Luminescence* **2009**, *129*, 423-429.
(76) Gross, M.; Muller, D. C.; Nothofer, H. G.; Scherf, U.; Neher, D.; Brauchle, C.; Meerholz, K. *Nature* **2000**, *405*, 661-665.
(77) Gustafsson, G.; Cao, Y.; Treacy, G. M.; Klavetter, F.; Colaneri, N.; Heeger, A. J. *Nature* **1992**, *357*, 477-479.
(78) Dimitrakopoulos, C. D.; Malenfant, P. R. L. *Advanced Materials* **2002**, *14*, 99-+.
(79) Horowitz, G. *Advanced Materials* **1998**, *10*, 365-377.
(80) Sirringhaus, H.; Tessler, N.; Friend, R. H. *Science* **1998**, *280*, 1741-1744.
(81) Kim, J. Y.; Lee, K.; Coates, N. E.; Moses, D.; Nguyen, T. Q.; Dante, M.; Heeger, A. J. *Science* **2007**, *317*, 222-225.
(82) Gupta, D.; Kabra, D.; Kolishetti, N.; Ramakrishnan, S.; Narayan, K. S. *Advanced Functional Materials* **2007**, *17*, 226-232.
(83) Xue, J. G.; Rand, B. P.; Uchida, S.; Forrest, S. R. *Journal of Applied Physics* **2005**, *98*.
(84) Davenas, J.; Alcouffe, P.; Ltaief, A.; Bouazizi, A. *Macromolecular Symposia* **2006**, *233*, 203-209.
(85) Moerner, W. E.; Orrit, M. *Science* **1999**, *283*, 1670-1676.
(86) Barbara, P. F.; Gesquiere, A. J.; Park, S. J.; Lee, Y. J. *Accounts of Chemical Research* **2005**, *38*, 602-610.
(87) Becker, K.; Lupton, J. M.; Feldmann, J.; Nehls, B. S.; Galbrecht, F.; Gao, D. Q.; Scherf, U. *Advanced Functional Materials* **2006**, *16*, 364-370.
(88) Huser, T.; Yan, M.; Rothberg, L. J. *Proceedings of the National Academy of Sciences of the United States of America* **2000**, *97*, 11187-11191.
(89) Pullerits, T.; Mirzov, O.; Scheblykin, I. G. *Journal of Physical Chemistry B* **2005**, *109*, 19099-19107.
(90) Sartori, S. S.; De Feyter, S.; Hofkens, J.; Van der Auweraer, M.; De Schryver, F.; Brunner, K.; Hofstraat, J. W. *Macromolecules* **2003**, *36*, 500-507.
(91) Scheblykin, I. G.; Yartsev, A.; Pullerits, T.; Gulbinas, V.; Sundstrom, V. *Journal of Physical Chemistry B* **2007**, *111*, 6303-6321.
(92) Schindler, F.; Lupton, J. M.; Feldmann, J.; Scherf, U. *Proceedings of the National Academy of Sciences of the United States of America* **2004**, *101*, 14695-14700.
(93) Uji-i, H.; Melnikov, S. M.; Deres, A.; Bergamini, G.; De Schryver, F.; Herrmann, A.; Mullen, K.; Enderlein, J.; Hofkens, J. *Polymer* **2006**, *47*, 2511-2518.
(94) Yu, J.; Hu, D. H.; Barbara, P. F. *Science* **2000**, *289*, 1327-1330.
(95) Lin, H. Z.; Tabaei, S. R.; Thomsson, D.; Mirzov, O.; Larsson, P. O.; Scheblykin, I. G. *Journal of the American Chemical Society* **2008**, *130*, 7042-7051.
(96) Schindler, F.; Lupton, J. M.; Muller, J.; Feldmann, J.; Scherf, U. *Nature Materials* **2006**, *5*, 141-146.
(97) Palacios, R. E.; Fan, F. R. F.; Grey, J. K.; Suk, J.; Bard, A. J.; Barbara, P. F. *Nature Materials* **2007**, *6*, 680-685.
(98) Huser, T.; Yan, M.; Rothberg, L. J. *P. Natl. Acad. Sci. USA* **2000**, *97*, 11187-11191.
(99) Smith, T. M.; Kim, J.; Peteanu, L. A.; Wildeman, J. *Journal of Physical Chemistry C* **2007**, *111*, 10119-10129.

(100) An, B. K.; Kwon, S. K.; Jung, S. D.; Park, S. Y. *Journal of the American Chemical Society* **2002**, *124*, 14410-14415.
(101) Wu, C. F.; Szymanski, C.; McNeill, J. *Langmuir* **2006**, *22*, 2956-2960.
(102) Gesquiere, A. J.; Tenery, D.; Hu, Z. J. *Spectroscopy* **2008**, *23*, 32-44.
(103) Sariciftci, N. S.; Smilowitz, L.; Heeger, A. J.; Wudl, F. *Science* **1992**, *258*, 1474-1476.
(104) Kim, H.; Lee, K.; Park, Y. G.; Suh, H. *Journal of the Korean Physical Society* **2003**, *42*, 183-186.
(105) Nguyen, T. Q.; Martini, I. B.; Liu, J.; Schwartz, B. J. *Journal of Physical Chemistry B* **2000**, *104*, 237-255.
(106) Hu, D. H.; Yu, J.; Wong, K.; Bagchi, B.; Rossky, P. J.; Barbara, P. F. *Nature* **2000**, *405*, 1030-1033.
(107) Wang, J.; Wang, D. L.; Moses, D.; Heeger, A. J. *Journal of Applied Polymer Science* **2001**, *82*, 2553-2557.
(108) Lin, H. Z.; Weng, Y. F.; Huang, H. M.; He, Q. G.; Zheng, M.; Bai, F. L. *Applied Physics Letters* **2004**, *84*, 2980-2982.
(109) Dyakonov, V.; Zoriniants, G.; Scharber, M.; Brabec, C. J.; Janssen, R. A. J.; Hummelen, J. C.; Sariciftci, N. S. *Physical Review B* **1999**, *59*, 8019-8025.
(110) Scheblykin, I.; Zoriniants, G.; Hofkens, J.; De Feyter, S.; Van der Auweraer, M.; De Schryver, F. C. *Chemphyschem* **2003**, *4*, 260-267.
(111) Hoven, C. V.; Garcia, A.; Bazan, G. C.; Nguyen, T. Q. *Advanced Materials* **2008**, *20*, 3793-3810.
(112) Kroon, R.; Lenes, M.; Hummelen, J. C.; Blom, P. W. M.; De Boer, B. *Polymer Reviews* **2008**, *48*, 531-582.
(113) Zaumseil, J.; Sirringhaus, H. *Chemical Reviews* **2007**, *107*, 1296-1323.
(114) Friend, R. H.; Gymer, R. W.; Holmes, A. B.; Burroughes, J. H.; Marks, R. N.; Taliani, C.; Bradley, D. D. C.; Dos Santos, D. A.; Bredas, J. L.; Logdlund, M.; Salaneck, W. R. *Nature* **1999**, *397*, 121-128.
(115) Ruseckas, A.; Namdas, E. B.; Ganguly, T.; Theander, M.; Svensson, M.; Andersson, M. R.; Inganas, O.; Sundstrom, V. *Journal of Physical Chemistry B* **2001**, *105*, 7624-7631.
(116) Rumbles, G.; Samuel, I. D. W.; Collison, C. J.; Miller, P. F.; Moratti, S. C.; Holmes, A. B. *Synthetic Metals* **1999**, *101*, 158-161.
(117) Rothberg, L. J.; Yan, M.; Papadimitrakopoulos, F.; Galvin, M. E.; Kwock, E. W.; Miller, T. M. *Synthetic Metals* **1996**, *80*, 41-58.
(118) Jakubiak, R.; Collison, C. J.; Wan, W. C.; Rothberg, L. J.; Hsieh, B. R. *J. Phys. Chem. A* **1999**, *103*, 2394-2398.
(119) Brown, P. J.; Thomas, D. S.; Kohler, A.; Wilson, J. S.; Kim, J. S.; Ramsdale, C. M.; Sirringhaus, H.; Friend, R. H. *Physical Review B* **2003**, *67*.
(120) Meskers, S. C. J.; Janssen, R. A. J.; Haverkort, J. E. M.; Wolter, J. H. *Chemical Physics* **2000**, *260*, 415-439.
(121) Van Averbeke, B.; Beljonne, D. *Journal of Physical Chemistry A* **2009**, *113*, 2677-2682.
(122) Grage, M. M. L.; Pullerits, T.; Ruseckas, A.; Theander, M.; Inganas, O.; Sundstrom, V. *Chemical Physics Letters* **2001**, *339*, 96-102.

(123) Wood, P.; Samuel, I. D. W.; Schrock, R.; Christensen, R. L. *Journal of Chemical Physics* **2001**, *115*, 10955-10963.
(124) Kline, R. J.; McGehee, M. D.; Kadnikova, E. N.; Liu, J. S.; Frechet, J. M. J.; Toney, M. F. *Macromolecules* **2005**, *38*, 3312-3319.
(125) Yang, X.; Loos, J. *Macromolecules* **2007**, *40*, 1353-1362.
(126) Reyes-Reyes, M.; Kim, K.; Carroll, D. L. *Applied Physics Letters* **2005**, *87*.
(127) Liu, J.; Shi, Y. J.; Yang, Y. *Advanced Functional Materials* **2001**, *11*, 420-424.
(128) Arias, A. C.; MacKenzie, J. D.; Stevenson, R.; Halls, J. J. M.; Inbasekaran, M.; Woo, E. P.; Richards, D.; Friend, R. H. *Macromolecules* **2001**, *34*, 6005-6013.
(129) Hoppe, H.; Sariciftci, N. S. *Journal of Materials Chemistry* **2006**, *16*, 45-61.
(130) Li, G.; Yao, Y.; Yang, H.; Shrotriya, V.; Yang, G.; Yang, Y. *Advanced Functional Materials* **2007**, *17*, 1636-1644.
(131) Surin, M.; Hennebicq, E.; Ego, C.; Marsitzky, D.; Grimsdale, A. C.; Mullen, K.; Bredas, J. L.; Lazzaroni, R.; Leclere, P. *Chemistry of Materials* **2004**, *16*, 994-1001.
(132) Khan, A. L. T.; Sreearunothai, P.; Herz, L. M.; Banach, M. J.; Kohler, A. *Physical Review B* **2004**, *69*.
(133) Moons, E. *Journal of Physics-Condensed Matter* **2002**, *14*, 12235-12260.
(134) Ariu, M.; Lidzey, D. G.; Sims, M.; Cadby, A. J.; Lane, P. A.; Bradley, D. D. C. *Journal of Physics-Condensed Matter* **2002**, *14*, 9975-9986.
(135) Cadby, A. J.; Lane, P. A.; Mellor, H.; Martin, S. J.; Grell, M.; Giebeler, C.; Bradley, D. D. C.; Wohlgenannt, M.; An, C.; Vardeny, Z. V. *Physical Review B* **2000**, *62*, 15604-15609.
(136) Teetsov, J.; Vanden Bout, D. A. *Journal of Physical Chemistry B* **2000**, *104*, 9378-9387.
(137) Bradley, D. D. C.; Grell, M.; Grice, A.; Tajbakhsh, A. R.; O'Brien, D. F.; Bleyer, A. *Optical Materials* **1998**, *9*, 1-11.
(138) Chappell, J.; Lidzey, D. G.; Jukes, P. C.; Higgins, A. M.; Thompson, R. L.; O'Connor, S.; Grizzi, I.; Fletcher, R.; O'Brien, J.; Geoghegan, M.; Jones, R. A. L. *Nature Materials* **2003**, *2*, 616-621.
(139) Donley, C. L.; Zaumseil, J.; Andreasen, J. W.; Nielsen, M. M.; Sirringhaus, H.; Friend, R. H.; Kim, J. S. *Journal of the American Chemical Society* **2005**, *127*, 12890-12899.
(140) Palacios, R. E.; Barbara, P. F. *Journal Of Fluorescence* **2007**, *17*, 749-757.
(141) Kim, D. Y.; Grey, J. K.; Barbara, P. F. *Synthetic Metals* **2006**, *156*, 336-345.
(142) Stejskal, J. *Journal of Polymer Materials* **2001**, *18*, 225-258.
(143) Kurokawa, N.; Yoshikawa, H.; Hirota, N.; Hyodo, K.; Masuhara, H. *Chemphyschem* **2004**, *5*, 1609-1615.
(144) Smith, T. M.; Hazelton, N.; Peteanu, L. A.; Wildeman, J. *Journal of Physical Chemistry B* **2006**, *110*, 7732-7742.
(145) Xue, L. L.; Liu, L. J.; Gao, Q.; Wen, S. P.; He, J. T.; Tian, W. J. *Solar Energy Materials and Solar Cells* **2009**, *93*, 501-507.
(146) Alam, M. M.; Jenekhe, S. A. *Chemistry of Materials* **2004**, *16*, 4647-4656.
(147) Kumar, S.; Nann, T. *Journal of Materials Research* **2004**, *19*, 1990-1994.
(148) Greenham, N. C.; Peng, X. G.; Alivisatos, A. P. *Synthetic Metals* **1997**, *84*, 545-546.

(149) Petrella, A.; Tamborra, M.; Curri, M. L.; Cosma, P.; Striccoli, M.; Cozzoli, P. D.; Agostiano, A. *Journal of Physical Chemistry B* **2005**, *109*, 1554-1562.
(150) Collison, C. J.; Rothberg, L. J.; Treemaneekarn, V.; Li, Y. *Macromolecules* **2001**, *34*, 2346-2352.
(151) Clark, J.; Silva, C.; Friend, R. H.; Spano, F. C. *Phys Rev Lett* **2007**, *98*, 206406.
(152) Spano, F. C. *Journal of Chemical Physics* **2005**, *122*.
(153) Quan, S. Y.; Teng, F.; Xu, Z.; Quan, L.; Zhang, T.; Liu, D.; Hou, Y. B.; Wang, Y. S.; Xu, X. R. *Journal of Luminescence* **2007**, *124*, 81-84.
(154) Marletta, A.; Goncalves, V. C.; Balogh, D. T. *Journal of Luminescence* **2006**, *116*, 87-93.
(155) Bjorklund, T. G.; Lim, S. H.; Bardeen, C. J. *Synthetic Metals* **2004**, *142*, 195-200.
(156) Ho, P. K. H.; Kim, J. S.; Tessler, N.; Friend, R. H. *Journal of Chemical Physics* **2001**, *115*, 2709-2720.
(157) Huang, K.; Rhys, A. *Proceeding of the Royal Society of London* **1950**, *A204*, 406-423.
(158) Bassler, H.; Schweitzer, B. *Accounts of Chemical Research* **1999**, *32*, 173-182.
(159) Kennedy, S. P.; Garro, N.; Phillips, R. T. *Physical Review B* **2001**, *64*.
(160) Borges, C. A. M.; Marletta, A.; Faria, R. M.; Guimaraes, F. E. G. *Brazilian Journal of Physics* **2004**, *34*, 590-592.
(161) Hagler, T. W.; Pakbaz, K.; Voss, K. F.; Heeger, A. J. *Physical Review B* **1991**, *44*, 8652-8666.
(162) He, G. F.; Li, Y. F.; Liu, J.; Yang, Y. *Applied Physics Letters* **2002**, *80*, 4247-4249.
(163) Lammi, R. K.; Barbara, P. F. *Photochemical & Photobiological Sciences* **2005**, *4*, 95-99.
(164) Ariu, M.; Sims, M.; Rahn, M. D.; Hill, J.; Fox, A. M.; Lidzey, D. G.; Oda, M.; Cabanillas-Gonzalez, J.; Bradley, D. D. C. *Physical Review B* **2003**, *67*.
(165) Wang, C. F.; White, J. D.; Lim, T. L.; Hsu, J. H.; Yang, S. C.; Fann, W. S.; Peng, K. Y.; Chen, S. A. *Physical Review B* **2003**, *67*.
(166) Collini, E.; Scholes, G. D. *Science* **2009**, *323*, 369-373.
(167) Hennebicq, E.; Pourtois, G.; Scholes, G. D.; Herz, L. M.; Russell, D. M.; Silva, C.; Setayesh, S.; Grimsdale, A. C.; Mullen, K.; Bredas, J. L.; Beljonne, D. *Journal of the American Chemical Society* **2005**, *127*, 4744-4762.
(168) Schwartz, B. J.; Nguyen, T. Q.; Wu, J. J.; Tolbert, S. H. *Synthetic Metals* **2001**, *116*, 35-40.
(169) Cossiello, R. F.; Akcelrud, L.; Atvars, D. Z. *Journal of the Brazilian Chemical Society* **2005**, *16*, 74-86.
(170) Joël Davenas, P. A. A. L. A. B. *Macromolecular Symposia* **2006**, *233*, 203-209.
(171) Bjorstrom, C. M.; Magnusson, K. O.; Moons, E. *Synthetic Metals* **2005**, *152*, 109-112.
(172) Chang, R.; Hsu, J. H.; Fann, W. S.; Liang, K. K.; Chiang, C. H.; Hayashi, M.; Yu, J.; Lin, S. H.; Chang, E. C.; Chuang, K. R.; Chen, S. A. *Chemical Physics Letters* **2000**, *317*, 142-152.
(173) Mozer, A. J.; Denk, P.; Scharber, M. C.; Neugebauer, H.; Sariciftci, N. S. *Journal of Physical Chemistry B* **2004**, *108*, 5235-5242.

(174) Wienk, M. M.; Kroon, J. M.; Verhees, W. J. H.; Knol, J.; Hummelen, J. C.; van Hal, P. A.; Janssen, R. A. J. *Angewandte Chemie-International Edition* **2003**, *42*, 3371-3375.
(175) Kim, Y.; Cook, S.; Tuladhar, S. M.; Choulis, S. A.; Nelson, J.; Durrant, J. R.; Bradley, D. D. C.; Giles, M.; McCulloch, I.; Ha, C. S.; Ree, M. *Nature Materials* **2006**, *5*, 197-203.
(176) Ma, W. L.; Yang, C. Y.; Gong, X.; Lee, K.; Heeger, A. J. *Advanced Functional Materials* **2005**, *15*, 1617-1622.
(177) Padinger, F.; Rittberger, R. S.; Sariciftci, N. S. *Advanced Functional Materials* **2003**, *13*, 85-88.
(178) Schilinsky, P.; Waldauf, C.; Brabec, C. J. *Applied Physics Letters* **2002**, *81*, 3885-3887.
(179) Veldman, D.; Ipek, O.; Meskers, S. C. J.; Sweelssen, J.; Koetse, M. M.; Veenstra, S. C.; Kroon, J. M.; van Bavel, S. S.; Loos, J.; Janssen, R. A. J. *Journal of the American Chemical Society* **2008**, *130*, 7721-7735.
(180) Han, J.; Craighead, H. G. *Science* **2000**, *288*, 1026-1029.
(181) Karlsson, M.; Davidson, M.; Karlsson, R.; Karlsson, A.; Bergenholtz, J.; Konkoli, Z.; Jesorka, A.; Lobovkina, T.; Hurtig, J.; Voinova, M.; Orwar, O. *Annual Review of Physical Chemistry* **2004**, *55*, 613-649.
(182) Martin, C. R.; Kohli, P. *Nature Reviews Drug Discovery* **2003**, *2*, 29-37.
(183) Ambrosi, M.; Fratini, E.; Alfredsson, V.; Ninham, B. W.; Giorgi, R.; Lo Nostro, P.; Baglioni, P. *Journal of the American Chemical Society* **2006**, *128*, 7209-7214.
(184) Brazhnik, K. P.; Vreeland, W. N.; Hutchison, J. B.; Kishore, R.; Wells, J.; Helmerson, K.; Locascio, L. E. *Langmuir* **2005**, *21*, 10814-10817.
(185) Brizard, A.; Aime, C.; Labrot, T.; Huc, I.; Berthier, D.; Artzner, F.; Desbat, B.; Oda, R. *Journal of the American Chemical Society* **2007**, *129*, 3754-3762.
(186) Brizard, A.; Oda, R.; Huc, I. In *Low Molecular Mass Gelators: Design, Self-Assembly, Function*; Springer-Verlag Berlin: Berlin, 2005; Vol. 256, p 167-218.
(187) Cheng, Q.; Yamamoto, M.; Stevens, R. C. *Langmuir* **2000**, *16*, 5333-5342.
(188) Douliez, J. P. *Journal of the American Chemical Society* **2005**, *127*, 15694-15695.
(189) Douliez, J. P.; Gaillard, C.; Navailles, L.; Nallet, F. *Langmuir* **2006**, *22*, 2942-2945.
(190) Fuhrhop, J. H.; Schnieder, P.; Boekema, E.; Helfrich, W. *Journal of the American Chemical Society* **1988**, *110*, 2861-2867.
(191) Goldstein, A. S.; Lukyanov, A. N.; Carlson, P. A.; Yager, P.; Gelb, M. H. *Chemistry and Physics of Lipids* **1997**, *88*, 21-36.
(192) Guo, Y. L.; Yui, H.; Minamikawa, H.; Yang, B.; Masuda, M.; Ito, K.; Shimizu, T. *Chemistry of Materials* **2006**, *18*, 1577-1580.
(193) Imae, T.; Takahashi, Y.; Muramatsu, H. *Journal of the American Chemical Society* **1992**, *114*, 3414-3419.
(194) John, G.; Masuda, M.; Okada, Y.; Yase, K.; Shimizu, T. *Advanced Materials* **2001**, *13*, 715-718.
(195) Lauf, U.; Fahr, A.; Westesen, K.; Ulrich, A. S. *Chemphyschem* **2004**, *5*, 1246-1249.
(196) Lee, K. C.; Lukyanov, A. N.; Gelb, M. H.; Yager, P. *Biochimica Et Biophysica Acta-Biomembranes* **1998**, *1371*, 168-184.

(197) Matsui, H.; Gologan, B. *Journal of Physical Chemistry B* **2000**, *104*, 3383-3386.
(198) Mishra, B. K.; Garrett, C. C.; Thomas, B. N. *Journal of the American Chemical Society* **2005**, *127*, 4254-4259.
(199) Mishra, B. K.; Thomas, B. N. *Journal of the American Chemical Society* **2002**, *124*, 6866-6871.
(200) Shimizu, T.; Masuda, M. *Journal of the American Chemical Society* **1997**, *119*, 2812-2818.
(201) Song, J.; Cheng, Q.; Kopta, S.; Stevens, R. C. *Journal of the American Chemical Society* **2001**, *123*, 3205-3213.
(202) Spector, M. S.; Singh, A.; Messersmith, P. B.; Schnur, J. M. *Nano Letters* **2001**, *1*, 375-378.
(203) Terech, P.; de Geyer, A.; Struth, B.; Talmon, Y. *Advanced Materials* **2002**, *14*, 495-+.
(204) Thomas, B. N.; Corcoran, R. C.; Cotant, C. L.; Lindemann, C. M.; Kirsch, J. E.; Persichini, P. J. *Journal of the American Chemical Society* **1998**, *120*, 12178-12186.
(205) Thomas, B. N.; Lindemann, C. M.; Corcoran, R. C.; Cotant, C. L.; Kirsch, J. E.; Persichini, P. J. *Journal of the American Chemical Society* **2002**, *124*, 1227-1233.
(206) Wang, G. J.; Hollingsworth, R. I. *Advanced Materials* **2000**, *12*, 871-874.
(207) Wong, G. C. L.; Tang, J. X.; Lin, A.; Li, Y. L.; Janmey, P. A.; Safinya, C. R. *Science* **2000**, *288*, 2035-+.
(208) Yager, P.; Schoen, P. E. *Molecular Crystals and Liquid Crystals* **1984**, *106*, 371-381.
(209) Zastavker, Y. V.; Asherie, N.; Lomakin, A.; Pande, J.; Donovan, J. M.; Schnur, J. M.; Benedek, G. B. *Proceedings of the National Academy of Sciences of the United States of America* **1999**, *96*, 7883-7887.
(210) Goldstein, A. S.; Amory, J. K.; Martin, S. M.; Vernon, C.; Matsumoto, A.; Yager, P. *Bioorganic & Medicinal Chemistry* **2001**, *9*, 2819-2825.
(211) Johnson, D. L.; Polikandritou-Lambros, M.; Martonen, T. B. *Drug Delivery* **1996**, *3*, 9.
(212) Lee, K. C.; Carlson, P. A.; Goldstein, A. S.; Yager, P.; Gelb, M. H. *Langmuir* **1999**, *15*, 5500-5508.
(213) Meilander, N. J.; Yu, X. J.; Ziats, N. P.; Bellamkonda, R. V. *Journal of Controlled Release* **2001**, *71*, 141-152.
(214) Price, R.; Patchan, M. *Journal of Microencapsulation* **1991**, *8*, 301-306.
(215) Spargo, B. J.; Cliff, R. O.; Rollwagen, F. M.; Rudolph, A. S. *Journal of Microencapsulation* **1995**, *12*, 247-254.
(216) Jung, C.; Hellriegel, C.; Platschek, B.; Wohrle, D.; Bein, T.; Michaelis, J.; Brauchle, C. *Journal of the American Chemical Society* **2007**, *129*, 5570-5579.
(217) Kirstein, J.; Platschek, B.; Jung, C.; Brown, R.; Bein, T.; Brauchle, C. *Nature Materials* **2007**, *6*, 303-310.
(218) Saltzman, W. M.; Langer, R. *Biophysical Journal* **1989**, *55*, 163-171.
(219) Fatin-Rouge, N.; Starchev, K.; Buffle, J. *Biophysical Journal* **2004**, *86*, 2710-2719.
(220) Dalla Serra, M.; Fagiuoli, G.; Nordera, P.; Bernhart, I.; Della Volpe, C.; Di Giorgio, D.; Ballio, A.; Menestrina, G. *Molecular Plant-Microbe Interactions* **1999**, *12*, 391-400.

(221) Gao, F.; Mei, E. W.; Lim, M.; Hochstrasser, R. M. *Journal of the American Chemical Society* **2006**, *128*, 4814-4822.
(222) Okamoto, K.; Shook, C. J.; Bivona, L.; Lee, S. B.; English, D. S. *Nano Letters* **2004**, *4*, 233-239.
(223) Saxton, M. J.; Jacobson, K. *Annual Review of Biophysics and Biomolecular Structure* **1997**, *26*, 373-399.
(224) Fu, Y.; Ye, F. M.; Sanders, W. G.; Collinson, M. M.; Higgins, D. A. *Journal of Physical Chemistry B* **2006**, *110*, 9164-9170.
(225) Higgins, D. A.; Collinson, M. M. *Langmuir* **2005**, *21*, 9023-9031.
(226) Jung, C.; Hellriegel, C.; Michaelis, J.; Brauchle, C. *Advanced Materials* **2007**, *19*, 956-+.
(227) Jung, C.; Hellriegel, C.; Platschek, B.; Wohrle, D.; Bein, T.; Michaelis, J.; Brauchle, C. *Journal of the American Chemical Society* **2007**, *129*, 5570-5579.
(228) Seebacher, C.; Hellriegel, C.; Deeg, F. W.; Brauchle, C.; Altmaier, S.; Behrens, P.; Mullen, K. *Journal of Physical Chemistry B* **2002**, *106*, 5591-5595.